

2012-05-01

Observational and Numerical Studies of the Boundary Layer, Cloud, and Aerosol Variability in the Southeast Pacific Coastal Marine Stratocumulus

Xue Zheng

University of Miami, x.zheng09@gmail.com

Recommended Citation

Zheng, Xue, "Observational and Numerical Studies of the Boundary Layer, Cloud, and Aerosol Variability in the Southeast Pacific Coastal Marine Stratocumulus" (2012). *Open Access Dissertations*. Paper 789.
http://scholarlyrepository.miami.edu/oa_dissertations/789

This Open access is brought to you for free and open access by the Electronic Theses and Dissertations at Scholarly Repository. It has been accepted for inclusion in Open Access Dissertations by an authorized administrator of Scholarly Repository. For more information, please contact jrenaud@miami.edu.

Report Documentation Page		Form Approved OMB No. 0704-0188
Public reporting burden for the collection of information is estimated to average 1 hour per response, including the time for reviewing instructions, searching existing data sources, gathering and maintaining the data needed, and completing and reviewing the collection of information. Send comments regarding this burden estimate or any other aspect of this collection of information, including suggestions for reducing this burden, to Washington Headquarters Services, Directorate for Information Operations and Reports, 1215 Jefferson Davis Highway, Suite 1204, Arlington VA 22202-4302. Respondents should be aware that notwithstanding any other provision of law, no person shall be subject to a penalty for failing to comply with a collection of information if it does not display a currently valid OMB control number.		
1. REPORT DATE 01 MAY 2012	2. REPORT TYPE	3. DATES COVERED 00-00-2012 to 00-00-2012
4. TITLE AND SUBTITLE Observational and Numerical Studies of the Boundary Layer, Cloud, and Aerosol Variability in the Southeast Pacific Coastal Marine Stratocumulus		5a. CONTRACT NUMBER
		5b. GRANT NUMBER
		5c. PROGRAM ELEMENT NUMBER
6. AUTHOR(S)		5d. PROJECT NUMBER
		5e. TASK NUMBER
		5f. WORK UNIT NUMBER
7. PERFORMING ORGANIZATION NAME(S) AND ADDRESS(ES) University of Miami,Coral Gables,FL,33124		8. PERFORMING ORGANIZATION REPORT NUMBER
9. SPONSORING/MONITORING AGENCY NAME(S) AND ADDRESS(ES)		10. SPONSOR/MONITOR'S ACRONYM(S)
		11. SPONSOR/MONITOR'S REPORT NUMBER(S)
12. DISTRIBUTION/AVAILABILITY STATEMENT Approved for public release; distribution unlimited		
13. SUPPLEMENTARY NOTES		
14. ABSTRACT <p>This dissertation investigates the impacts of meteorological factors and aerosol indirect effects on the costal marine stratocumulus (Sc) variations in the southeast Pacific, a region that has been largely unexplored and is a major challenge of the modeling community, through both observational and numerical studies. This study provides a unique dataset for documenting the characteristics of the marine Sc-topped BL off the coast of Northern Chile. The observational study shows that the boundary layer (BL) over this region was well mixed and topped by a thin and non-drizzling Sc layer on days synoptically-quiet with little variability between this region and the coast. The surface wind, the surface fluxes and the BL turbulence appeared to be weaker than those over other ocean regions where stratocumulus clouds exist. The weaker turbulence in the BL may contribute to a relatively low entrainment rate calculated from the near cloud top fluxes. This in-situ data set can help us better understand cloud processes within this coastal regime, and also be valuable for the calibration of the satellite retrievals and the evaluation of numerical models operating at a variety of scales. A strong positive correlation between the liquid water path (LWP) and the cloud condensation nuclei (CCN) was observed under similar boundary layer conditions. This correlation cannot be explained by some of the hypotheses based on previous modeling studies. The satellite retrievals obtained upstream one day prior to the flight observations reveal some sign that the clouds under the high CCN concentrations have minimal LWP loss due to precipitation suppression effects. The results from large eddy simulations with a two-momentum bulk microphysics scheme under different idealized environment scenarios based on aircraft observations indicate that 1) the simulated Sc responds more quickly to changes in large-scale subsidence than to those changes in surface fluxes, free tropospheric humidity, and the BL-top stability; 2) large-scale vertical wind shear clearly induces cloud-top mixing and enhances entrainment rate; 3) the solar radiation could weaken the BL turbulence, reduce the entrainment rate and decouple the BL; and 4) the impact of the reduced cloud sedimentation due to increasing aerosol on the cloud is small.</p>		

15. SUBJECT TERMS					
16. SECURITY CLASSIFICATION OF:			17. LIMITATION OF ABSTRACT Same as Report (SAR)	18. NUMBER OF PAGES 138	19a. NAME OF RESPONSIBLE PERSON
a. REPORT unclassified	b. ABSTRACT unclassified	c. THIS PAGE unclassified			

UNIVERSITY OF MIAMI

OBSERVATIONAL AND NUMERICAL STUDIES OF THE BOUNDARY LAYER,
CLOUD, AND AEROSOL VARIABILITY IN THE SOUTHEAST PACIFIC
COASTAL MARINE STRATOCUMULUS

By

Xue Zheng

A DISSERTATION

Submitted to the Faculty
of the University of Miami
in partial fulfillment of the requirements for
the degree of Doctor of Philosophy

Coral Gables, Florida

May 2012

UNIVERSITY OF MIAMI

A dissertation submitted in partial fulfillment of
the requirements for the degree of
Doctor of Philosophy

OBSERVATIONAL AND NUMERICAL STUDIES OF THE BOUNDARY LAYER,
CLOUD, AND AEROSOL VARIABILITY IN THE SOUTHEAST PACIFIC
COASTAL MARINE STRATOCUMULUS

Xue Zheng

Approved:

Bruce Albrecht, Ph.D.
Professor of Meteorology and
Physical Oceanography

Terri A. Scandura, Ph.D.
Dean of the Graduate School

Amy Clement, Ph.D.
Professor of Meteorology and
Physical Oceanography

Paquita Zuidema, Ph.D.
Associate Professor of
Meteorology and Physical
Oceanography

Shouping Wang, Ph.D.
Scientist, Marine Meteorology Division
Naval Research Laboratory
Monterey, California

Ping Zhu, Ph.D.
Assistant Professor of Earth
and Environment
Florida International University

ZHENG, XUE (Ph.D., Meteorology and Physical Oceanography)
Observational and Numerical Studies of the (May 2012)
Boundary Layer, Cloud, and Aerosol Variability
in the Southeast Pacific Coastal
Marine Stratocumulus

Abstract of a dissertation at the University of Miami.

Dissertation supervised by Professor Bruce Albrecht.
No. of pages in text. (124)

This dissertation investigates the impacts of meteorological factors and aerosol indirect effects on the coastal marine stratocumulus (Sc) variations in the southeast Pacific, a region that has been largely unexplored and is a major challenge of the modeling community, through both observational and numerical studies.

This study provides a unique dataset for documenting the characteristics of the marine Sc-topped BL off the coast of Northern Chile. The observational study shows that the boundary layer (BL) over this region was well mixed and topped by a thin and non-drizzling Sc layer on days synoptically-quiet with little variability between this region and the coast. The surface wind, the surface fluxes and the BL turbulence appeared to be weaker than those over other ocean regions where stratocumulus clouds exist. The weaker turbulence in the BL may contribute to a relatively low entrainment rate calculated from the near cloud top fluxes. This *in-situ* data set can help us better understand cloud processes within this coastal regime, and also be valuable for the calibration of the satellite

retrievals and the evaluation of numerical models operating at a variety of scales.

A strong positive correlation between the liquid water path (LWP) and the cloud condensation nuclei (CCN) was observed under similar boundary layer conditions. This correlation cannot be explained by some of the hypotheses based on previous modeling studies. The satellite retrievals obtained upstream one day prior to the flight observations reveal some sign that the clouds under the high CCN concentrations have minimal LWP loss due to precipitation suppression effects.

The results from large eddy simulations with a two-momentum bulk microphysics scheme under different idealized environment scenarios based on aircraft observations indicate that 1) the simulated Sc responds more quickly to changes in large-scale subsidence than to those changes in surface fluxes, free-tropospheric humidity, and the BL-top stability; 2) large-scale vertical wind shear clearly induces cloud-top mixing and enhances entrainment rate; 3) the solar radiation could weaken the BL turbulence, reduce the entrainment rate and decouple the BL; and 4) the impact of the reduced cloud sedimentation due to increasing aerosol on the cloud is small.

Acknowledgements

This dissertation benefited greatly from the dedicated effort of many people. First of all, I am grateful to my advisor, Dr. Bruce A. Albrecht, for introducing me to the research area of boundary layer clouds. I was fortunate to have a lot of opportunities to participate in many observational projects and also collaborate with the modeling community. The research experience, the intellectual skills, the support and encouragement I gained from him will benefit me forever.

I appreciate all the support from my committee members. In particular, Dr. Shouping Wang taught me a lot about LES simulations during our collaboration. Dr. Ping Zhu kindly provided computational resources for the numerical simulations in this study. Dr. Paquita Zuidema offered me several valuable ideas on the cloud-aerosol interactions, and the comments from Dr. Amy Clement inspired me to think in a broader research area.

This dissertation would not have been possible without the CIRPAS Twin Otter team during VAMOS-REx. Drs. Hafliði H. Jonsson and Djamal Khelif kindly provided the quality-controlled aircraft observations. Dr. Patrick Minnis and Kirk Ayers provided the satellite retrievals during the flight observations. Drs. Graham Feingold and Patrick Chuang provided key scientific input on the observing strategies employed and interpretation of the initial results. I also appreciate their critical comments and input in Chapter 2 and Chapter 3 of this dissertation.

I would like to thank current and past group mates: Shaunna, Virendra,

Eunsil, Tom, and Ming. I learned more from them than they could imagine about aircraft and radar observations, scientific communication skills, and everyday life experiences. I have also been fortunate to be a member of the RSMAS community. I thank all the RSMAS faculty, staff, and colleagues who helped me in my research. I really enjoyed working with them for the past several years.

Finally, I sincerely thank my family and friends for always being supportive in every aspect of my Ph.D. study life. Without them, my life in Miami would not have been so nice and fun.

This work was supported by ONR grant N000140810465, NOAA grant NA17RJ1226, and the NOAA/CPPA Program under grant NAO8OAR4320889.

TABLE OF CONTENTS

List of Figures	vii
List of Tables	x
Chapter 1: Introduction	1
1.1 Motivation	1
1.2 Cloud-controlling Factors	2
1.3 VOCALS-REx	8
1.4 Scientific Objectives	10
Chapter 2: Cloud and Aerosol Variability in the Southeast Pacific Coastal Marine Stratocumulus	12
2.1 Motivation and Background	12
2.2 Data and Methodology	15
2.3 General Synoptic Conditions and Variations	20
2.4 Boundary Layer Vertical Structure	28
2.5 Temporal Variation of BL Structure	36
2.6 Aerosol and Cloud Properties	45
2.7 Summary	52
Chapter 3: Liquid Water Path and Cloud Condensation Nuclei Relationships in Marine Stratocumulus	56
3.1 Motivation and Objectives	56
3.2 Data and Methods	57
3.3 Results	61

3.4 Conclusion and Discussion	72
Chapter 4: The Impact of Large-Scale Forcing and Aerosol Variation on Simulated Stratocumulus Clouds	76
4.1 Motivation and Background	76
4.2 Model Description	78
4.3 The Impact of Large-Scale Forcing	83
4.4 The Impact of CCN Number Concentrations	98
4.5 Summary and Discussion	105
Chapter 5: Summary, conclusions and future work	108
5.1 Summary and conclusions	108
5.2 Future work	111
References	113

LIST OF FIGURES

Figure 2.1: Time series of aircraft altitude for Flight RF04 in Table 2.2 (Oct. 21 2008).	15
Figure 2.2: a) Composite Sea Level Pressure (Oct.16– Nov.13 2008), b) Composite 700-hPa geopotential height, c) 700-hPa geopotential height at 12:00UTC Nov. 1, 2008.	21
Figure 2.3: The average fields of a) Low cloud amount, b) LWP, c) R_e (micron) derived from GOES-10 data during the flight time.	23
Figure 2.4: The average surface wind (vectors) and divergence (color shading) from QuikSCAT (Oct.16– Nov.13 2008).	25
Figure 2.5: a) Two-dimensional isobaric back trajectories starting at 500 m from Point Alpha (Plus sign) for the 18 cases (color bar) with the 24-hour point (Blue Circle), and the 48-hour point (Square), b) Three-dimensional back trajectories starting at 2000 m from Point Alpha.	26
Figure 2.6: Synthesis of sea level pressure and 700hPa geopotential height a) at Point Alpha from NCEP reanalysis (12:00 UTC, open symbols) and aircraft observations (~12:00 UTC, solid symbols), b) at Iquique from NCEP reanalysis (12:00 UTC, open symbols) and radiosonde data (~12:00 UTC, solid symbols).	28
Figure 2.7: Profiles scaled by the PBL heights: a) total-water mixing ratio; b) liquid water potential temperature, c) LWC, d) wind speed, e) wind direction, and f) N_a from PCASP for all 18 flights.	30
Figure 2.8: Time–height section of (top) mixing ratio, (bottom) potential temperature from the soundings launched at Iquique during VOCALS-REx.	31
Figure 2.9: The soundings of a) wind speed, b) wind direction, c) potential temperature, and d) mixing ratio on Oct. 24. The average values from the horizontal legs are denoted as red squares.	33
Figure 2.10: a) Vertical velocity variance, b) Total water flux, and c) Liquid water potential temperature flux vs. normalized height calculated from all the flight legs for the 18 flights.	34
Figure 2.11: Synthesis of the inversion level at Point Alpha from flight data, and at Iquique from radiosonde data.	37

Figure 2.12: LWP integrated from aircraft soundings on all flight days.	38
Figure 2.13: a) $\Delta\theta$, b) Δq_t . The solid squares represent the values at Point Alpha measured by the aircraft, and the open circles donate the values at Iquique measured by the radiosonde system.	41
Figure 2.14: a) SST and BL-averaged θ_i , b) 30-m wind speed, c) 30-m wind direction, and d) surface wind vectors from flight data.	41
Figure 2.15: 3-day mean TRMM TMI SST map ending on a) Oct. 16, 2008; b) Nov. 13, 2008.	42
Figure 2.16: Average sub-cloud aerosol (red solid square), above-cloud aerosol (red cross), sub-cloud 0.2% CCN (open red square), above-cloud 0.2 % CCN (black triangle), and cloud droplet (black dot) number concentrations on all flight days.	47
Figure 2.17: R_e from the near-cloud-top legs on all flight days. Red symbols are GOES retrievals averaged over an area within a radius of 20 km of aircraft observations. Blue symbols are average Terra MODIS retrievals for a 0.5° region centered on Point Alpha taken at between 14:20 and 15:50 UTC.	49
Figure 2.18: LWP as a function of sub-cloud CCN concentrations for all flight days.	52
Figure 3.1: Vertical profiles of total water mixing ratio, liquid water potential temperature, and liquid water content for the 10 cases in the study.	59
Figure 3.2: LWP as a function of sub-cloud CCN concentrations for selected 10 flights. Open blue squares are GOES retrievals averaged for each entire flight mission over an area within a radius of 20 km of Point Alpha.	62
Figure 3.3: Sub-cloud layer CCN, PCASP and N_d for 10 cases sorted by increasing CCN from flight 1 to 10.	63
Figure 3.4: The six-hour average fields of LWP prior to the flight observation on a) 18 October (HC), c) 19 October (HC), e) 22 October (LC), g) 27 October (LC), i) 09 November (LC), and the six-hour average fields of R_e prior to the flight observation on b) 18 October (HC), d) 19 October (HC), f) 22 October (LC), h) 27 October (LC), j) 09 November derived from GOES-10 data.	69
Figure 3.5: Time evolution of GOES-derived LWP and R_e for the two highest (black cross symbols) and the three lowest (blue open symbols) CCN concentrations from 12 hours prior to the flight (marked as $t=-12\text{hr}$) to 1 hour before flight time ($t=-1\text{hr}$).	70

Figure 3.6: 12-hour average LWP along the back trajectories prior to the flights on the HC days (left bar) and LC days (right bar) with the range of the equivalent LWP proportion (gray bar) due to one-hour drizzle reduction.	72
Figure 4.1: Initial soundings of a) potential temperature, b) total water mixing ratio, and c) south-north wind component.	85
Figure 4.2: Snapshots of the albedo estimated with cloud water and cloud droplet number concentration a) Case 1, t =15 hour, b) Case A0, t = 15 hour, c) Case A1, t = 15 hour.	87
Figure 4.3: a) Vertical velocity variance , b) total water flux , and c) buoyancy flux vs. normalized height calculated from all 11 cases, t=15 hour.	88
Figure 4.4: Time evolutions of a) LWP, b) BL inversion height, for all 11 cases.	89
Figure 4.5: Initial soundings of a) potential temperature, b) total water mixing ratio, in group A, B, C.	99
Figure 4.6: Domain-averaged profiles of a) cloud droplet number concentrations, b) cloud water tendencies due to sedimentation in group A, B, C at t = 6 hour.	100
Figure 4.7: The 4-9 hour mean profiles of a) vertical velocity variance, b) longwave radiative heating, in group A, B, C.	101
Figure 4.8: Time evolutions of the simulated LWP.	102
Figure 4.9: The 4-9 hour mean profiles of a) updraft fraction in the cloudy area, b) Buoyancy flux in group A, B, C.	103
Figure 4.10: Horizontal distribution of cloud-top height in group A, B, C at t = 15 hour.	104

LIST OF TABLES

Table 2.1:	Flight List.....	16
Table 2.2:	Instrumentation on Twin Otter during VOCALS-REx.	17
Table 2.3:	Mean values of boundary layer at Point Alpha during VOCALS-REx.	32
Table 3.1:	Summary of drizzle rate as the functions of LWP/cloud depth and cloud droplet concentration observations.	61
Table 3.2:	Cloud, aerosol, and BL characteristics averaged for the two cases with the highest CCN, the three cases with the lowest CCN, the five highest CCN cases, and the five lowest CCN cases.	65
Table 3.3:	Large-scale advection estimation for the two cases with the highest CCN and the three cases with the lowest CCN.	67
Table 4.1:	Summary of the simulations.	83
Table 4.2:	Summary of the large-scale forcing in the simulations.	86
Table 4.3:	Results from the sensitivity to large-scale forcing.	92
Table 4.4:	Summary of the differences between the cases with large and small surface fluxes.	95
Table 4.5:	Sensitivity test for the aerosol number concentrations.	99
Table 4.6:	Results from the sensitivity to CCN number concentrations.	103

Chapter 1: Introduction

1.1 Motivation

Stratocumulus (Sc), along with cumulus, and stratus, is a genus of low clouds occurring within the planetary boundary layer (BL), where turbulent mixing plays a key role. Distinct from the other two low cloud types, Sc is a horizontally homogenized (unlike cumulus) convective cloud system embedded with individual convective overturning circulations (unlike stratus) (Lilly 1968; Bretherton and Wyant 1997). The Sc-topped BL is typically capped by a sharp temperature and moisture inversion. Seen from the satellite visible images, Sc extends over horizontal ranges from ~ 10 to ~ 1000 km with a depth of hundreds of meters. Generally speaking, Sc forms: 1) over the subtropical oceans in the downward branches of the Hadley circulations; 2) over the subsiding region of mid-latitude frontal systems; 3) over the oceans during cold-air outbreaks; and 4) over the polar regions (Wood 2012). In this study, we mainly focus on the marine Sc clouds located at the eastern edges of subtropical highs.

Sc covers more than 20% of the Earth's surface and about 1/3 of the Earth's oceans (Hahn and Warren 2007; Ackerman et al. 1993; Warren et al. 1988). The annual mean stratus cloud amount over the world reveals several Sc regions, such as the mid-latitudes and the eastern ocean basins, all of which are also areas with strong negative cloud radiative forcing (Hartmann et al. 1992). Therefore, Sc and stratus are found to be the most radiatively important cloud type for the current climate. Modeling studies indicate that the radiative impact

resulting from changes in the Sc global coverage and albedo can be comparable to that from the greenhouse effect (Slingo 1990). However, the Sc and cumulus feedbacks have been found to have the largest uncertainty in tropical cloud feedbacks simulated by general circulation models (Bony and Dufresne 2005; Soden and Vecchi 2011). The significant climatological importance of marine Sc and its large feedback uncertainty in the future climate motivated a number of researchers, including me, to study and better understand marine Sc, particularly their evolution under different environmental and anthropogenic forcing.

In section 1.2, we briefly summarize the current knowledge and the remaining challenges of the external and internal factors controlling marine Sc amount and radiative properties. Section 1.3 introduces a field experiment which took place in the southeast (SE) Pacific in 2008, the Variability of the American Monsoons Ocean-Cloud-Atmosphere-Land Study-Regional Experiment (VOCALS-REx). Most of the observational data used in this study are acquired during this field experiment. The introduction ends with the scientific objectives (section 1.4) that this dissertation attempts to address in the following chapters.

1.2 Cloud-controlling factors

Based on a number of field experiments, theoretical and numerical studies in the past decades, we have established a qualitative understanding on the primary meteorological and microphysical factors controlling the variability in Sc from annual to diurnal time scales (e.g., Albrecht et al. 1995a; Klein and Hartmann 1993; Xu et al. 2005; Klein 1997; Wood et al. 2011; etc.). The remainder of this section will briefly summarize the current knowledge on

meteorological factors and aerosol indirect effects that largely impact on the Sc-topped BL.

1.2.1 Meteorological factors

Previous studies established that large scale subsidence rate, lower tropospheric stability (LTS), sea surface temperature (SST), SST gradient, surface wind, free tropospheric temperature and humidity, etc. are the main meteorological factors (Norris 1998; Klein and Hartmann 1993; Stevens and Brenguier 2008; Klein 1997) that can control cloud-top height and cloud thickness. Because these factors are usually involved with each other through large scale atmospheric circulations, it is almost impossible to isolate any one effect from the others in the real world. Previous observational and modeling studies, however, suggest that the variations of Sc cover on different temporal and spatial scales are strongly correlated with certain controlling factors (Xu et al. 2005; Norris and Klein 2000; Klein 1997).

a) Large scale subsidence rate

As one of the top factors, subsidence rate works with many other factors to control the evolution of Sc-topped BL and Sc amount (Xu et al. 2005; Norris and Klein 2000). Subsidence is mainly determined by large-scale surface wind divergence according to mass continuity. Over the oceans, large-scale divergence $D(z)$ is usually approximated to be constant through the whole lower troposphere ($D(z) = \bar{D}$). The subsidence $w_{ls}(z_i)$ near the top of Sc-topped BL, therefore, is determined by the surface divergence and the inversion height:

$$w_{ls}(z_i) = -\bar{D} \times z_i$$

Moderate large-scale subsidence is an essential condition for the formation and maintenance of marine Sc. Subsiding warm and dry air from free troposphere encounters the cool moist air from ocean surface, thus a strong temperature and moisture inversion forms at the top of the Sc-topped BL. This strong inversion limits the deepening of the Sc-topped BL and decoupling. On the other hand, both too high and too low subsidence could result in the dissipation of marine Sc. If the inversion height is suppressed by a strong subsidence to near the lifting condensation level (LCL) where usually is the cloud base, the Sc cloud layer becomes thinner and even broken or dissipated (Weaver and Pearson, 1990). In Sc-topped BLs, through strong vertical mixing the turbulent eddies from the surface can reach the cloud top and mix with the turbulence generated by the cloud-top longwave radiative cooling. If the subsidence is too weak, the BL keeps deepening and the turbulent mixing near the cloud top will be unable to couple with the surface turbulent mixing process and the BL is no longer well-mixed. In the decoupled BL, cumulus clouds tend to form under the Sc layer maintained by the surface fluxes and can further cause the Sc breakup. As a result, the Sc cloud layer becomes no more horizontally homogenized and transits to cumulus cloud types (Albrecht et al. 1995 a, b). The transition of homogenous Sc layer to broken cumulus can significantly alter the cloud amount over the Sc regimes.

b) Lower tropospheric stability (LTS)

LTS can be defined as the potential temperature difference between 700 hPa and 1000 hPa (or surface) (Klein and Hartmann 1993; Norris 1998; etc.).

Therefore, the variability of LTS is controlled by SST and free tropospheric conditions. The relationship between the seasonal variations in LTS and the Sc variability is the most compelling relationship between low cloud amount and meteorological conditions (Klein and Hartmann 1993; Wood and Bretherton 2006; Sevents et al. 2007). The reason is that strong LTS and moderate large scale subsidence help the BL keep a strong inversion that reduces entrainment and maintains the Sc layer without decoupling (Wood and Bretherton 2004).

We could introduce the difference between potential temperature/ dry-static energy just above cloud top and at the surface, denoted as Δs , to indicate the stability near the top of BL. Δs also represents the estimated inversion strength of the Sc-topped BL (Wood and Bretherton 2006). Previous studies found that a properly constructed Δs can explain over 80% of interseasonal variance in low-cloud amount (Wood and Bretherton 2006).

c) SST, SST gradient and surface wind

Cool SST and surface wind impact on the surface fluxes which supply moisture and heat into the BL and modulate the turbulent mixing processes within the BL. On large scales such as interannual and seasonal variations of low-cloud amount are found to be negatively correlated with SST variation because SST largely controls the variation of LTS as the previous section noted (Klein et al. 1995; Xu et al. 2005).

Increasing SST and reducing surface divergence can enhance the transition from shallow to deep MBL over the subtropical oceans because increased surface fluxes and reduced large scale subsidence can cause the BL

deepening, and then decoupling with cumulus clouds developing below the Sc layer (Bretherton and Wyant 1997; Xiao et al. 2010). As the cumulus cloud layer builds up and the BL remains decoupled, the Sc layer can dissipate and the Sc-topped BL transitions into trade-wind cumulus topped BL (Albrecht et al 1995b).

On scales smaller than synoptic scale, the variation of low cloud cover may be positively correlated with SST variation due to increased surface moisture supply (Xie, 2004). Statistical studies (e.g., Xu et al., 2005; Mauger and Norris, 2010) indicated that surface wind speed and SST gradient also have strong impact on the low cloud cover variations on the synoptic time scale.

d) Free tropospheric humidity

A number of field experiments have shown that the enhancement of free tropospheric humidity under the influence of weather systems is common over the marine Sc regimes (e.g., Serpetzoglou et al. 2008; Bretherton et al. 2010; Stevens et al. 2003). Free tropospheric humidity is likely to play a critical role on the variability of Sc amount through modulation of the cloud-top longwave cooling processes and cloud-top entrainment processes (Turton and Nicholls 1987; Nieuwstadt and Businger 1984; Randall 1980). Observations (Bretherton et al. 2010) along 20°S between the coast of Northern Chile and a buoy 1500 km offshore indicated that the cloud-top longwave cooling over the coastal region with higher free tropospheric humidity was lower than that over the remoter ocean area. Although the equilibrium cloud depth in a well-mixed BL is suggested to decrease with increasing free tropospheric humidity (Betts and Ridgway 1989) due to the reduced cloud-top radiative cooling, Sc clouds with

higher cloud fractions are found to be associated with higher free tropospheric humidity as shown in a composite analysis by Mauger and Norris (2010). Therefore, there is a lack of definitive conclusions on the role of free tropospheric humidity on the Sc amount (see a discussion in Wood, 2012).

1.2.2 Aerosol indirect effects

In addition to the meteorological factors, aerosols can have a significant impact on the cloud albedo and cloud amount as well (Twomey 1977; Albrecht 1989; Lohmann and Feichter 2005; etc.). Acting as cloud condensation nuclei (CCN), aerosols can be activated to be cloud droplets when environmental super-saturation reaches certain level (Pruppacher and Klett 1997). Therefore, for a Sc layer with a fixed LWP, anthropogenic aerosol can increase cloud droplet number concentration, reduce the average size of cloud droplets, and modify the cloud droplet size distribution. As the cloud droplet size distribution changed, the cloud properties, in-cloud microphysical processes, and the cloud and BL dynamics are considered to respond through certain interactions. The first cloud response is that the cloud albedo will increase due to the reduced cloud droplet size (Twomey 1977), which is called the first aerosol indirect effect. This study will mainly focus on the cloud amount and life time response, also called the second aerosol indirect effect (Albrecht 1989).

In terms of in-cloud microphysical processes, the most straightforward and significant cloud response to aerosols is that in-cloud precipitation tends to be suppressed due to the reduced collision-coalescence (Albrecht 1989). A number of observations indicate that in warm clouds, cloud-base precipitation rate

decreases as cloud droplet number concentration increases (e.g., Pawlowska and Brenguier 2003; Wood 2005; Lu et al. 2007; etc.). Therefore, the cloud LWP is likely to increase and result in a larger cloud amount and longer cloud lifetime (Christensen and Stephens 2011; Lu and Seinfeld 2005). Impacts of precipitation-suppression on the cloud and BL turbulence structure, however, are less well understood and have controversial aspects (Wood 2007; Sandu et al. 2008; Ackerman et al. 2009).

For non-drizzling Sc, although the proposed mechanisms are different, current hypotheses based on large-eddy simulations (LES) (Ackerman et al. 2004; Bretherton et al., 2007; Wang et al. 2003) suggest that enhancing cloud-top entrainment rate resulted from the higher CCN concentration can decrease the cloud LWP. Ackerman et al. (2004) and Wood (2007) attributed the enhanced entrainment rate in the high-CCN cloud to increased boundary-layer turbulence, while Bretherton et al. (2007) suggested that increased cloud-top evaporation cooling in the high-CCN cloud induces buoyancy reversal and promotes entrainment processes. Observations showing increasing, decreasing, or constant LWP in polluted clouds make it even more difficult to address the second aerosol indirect effect on the non-drizzling Sc (e.g., Brioude et al. 2009; Lu et al. 2007; Coakley and Walsh 2002; Christensen and Stephens 2011; Christensen et al 2009; etc.).

1.3 VOCALS-REx

From October to November 2008, The VAMOS Ocean-Cloud-Atmosphere-Land Study-Regional Experiment (VOCALS-REx) took place over

the SE Pacific (69° - 86° W, 12° - 31° S), an area extending from the near-coastal region of northern Chile and southern Peru to the remote ocean, where one of the most extended and persistent subtropical Sc deck in the world is located (Klein and Hartmann 1993). Since the coupled ocean-atmosphere-land system in this region is found to be critical to global climate but still remaining a challenge for global and regional modeling community to successfully simulate, VOCALS-REx aimed at 1) further understanding aerosol-cloud-drizzle interactions in the BL; and 2) improving model simulations and predictions of the SE Pacific coupled ocean-atmosphere-land system on a variety of scales (Wood et al. 2011a). Over 150 scientists from 40 institutions in 8 countries were involved in VOCALS-REx, with observational platforms including five aircraft, two research vessels, and six surface sites. For the atmospheric observational component, VOCALS-REx gathered an intensive dataset to study the BL structure, lower free troposphere, aerosol and cloud properties, and precipitation. The multi-platform observations during VOCALS revealed that the Sc-topped BL depth deepens from ~ 1000 m near shore to ~ 1600 m at a distance of about 1500 km offshore along the 20° S section (Bretherton et al. 2010). Here we are not going to cover all details of this field experiment. Instead, we just focus on the atmosphere part and the particular aspects we will further analyze in the rest part of this dissertation.

As one observational platform of VOCALS-REx, the Center for Interdisciplinary Remotely-Piloted Aircraft Studies (CIRPAS) Twin Otter aircraft made observations off the coast of Northern Chile. Comprehensive *in-situ* observations of aerosol, turbulence, cloud properties, and drizzle variables in

coastal marine Sc were collected onboard. The observed BL in the coastal region is generally well-mixed and with little or no drizzle in a relative solid Sc layer. The Twin Otter project provides a unique opportunity to investigate the processes responsible for the aerosol and cloud properties variations over the coastal region, which were largely unexplored.

On the map of the 2000-2008 mean cloud droplet concentration over the SE Pacific (Fig.1, George and Wood 2010), the maximum cloud droplet concentration is located at the coastal region between 17° S and 30° S and the N_d decreases sharply west of the maximum. The cloud LWP pattern indicates that the cloud layer over the max cloud droplet concentration region is thin Sc cloud with little or no drizzle. The coastal region with large aerosol variations provides a unique area to study the aerosol indirect effects on the Sc layer.

1.4 Scientific objectives

As discussed above, there are still a set of unknown aspects about controlling factors on the subtropical marine Sc cloud variations, particularly in the SE Pacific coastal region. This study seeks to address two questions:

1) Is there any correlation between the Sc and aerosol variations near the coast of northern Chile?

2) What are the contributions of meteorological factors and aerosol indirect effects on the observed Sc variations?

To address the first question, we used observations during VOCALS-REx to document the Sc and aerosol variations near the coast of northern Chile, which is fully discussed in chapter 2. Chapter 3 looks into an observed positive

correlation between the cloud LWP and the BL CCN number concentration along with the cloud history prior to the flight observations from the satellite retrievals. In chapter 4, we try to explore the impact of large-scale forcing and aerosol variation on the simulated stratocumulus clouds by analyzing two sets of large eddy simulations based on the observed BL structure. Summary and conclusions are described in chapter 5.

Chapter 2: Cloud and aerosol variability in the Southeast Pacific coastal marine stratocumulus

2.1 Motivation and background

There have been few observational studies in the SE Pacific until the last decade or so, when several research cruises were conducted to study marine Sc and marine BL processes in the SE Pacific. The CIMAR-5 (Garreaud et al. 2001), East Pacific Investigation of Climate (EPIC) 2001 (Bretherton et al. 2004), Pan-American Climate Studies (PACS) Stratus 2003 (Kollias et al. 2004), and Stratus 2004 (Serpetzoglou et al. 2008) research cruises explored the BL over the subtropical SE Pacific more than 1000 km offshore. CIMAR-5 provided a transect of the SE Pacific boundary layer at 27° S between the Chilean coast (71° W) and Easter Island (110° W) during late October 1999. It revealed the east-west increase in the BL depth from less than 1000 m near the coast to over 2000 m at the far end of the transect. The other research cruises included 5-6 days of observations at the Stratus Ocean Reference Station (Stratus ORS, 20° S, 85° W) (Cronin et al. 2002; Bretherton et al. 2004; Ghate et al. 2009). The EPIC 2001 observations were made in October --- the month with the maximum climatological stratus cloud amount (Klein and Hartmann 1993; Ghate et al. 2009). During this cruise the BL at the Stratus ORS was usually well-mixed and covered by a solid Sc layer with a thickness of less than 500 m. The clouds were close to adiabatic (Bretherton et al. 2004). The most variable cloud conditions were observed in November during PACS Stratus 2003 (Kollias et al. 2004) when solid Sc, broken cloud, clear sky, and drizzle were observed. The BL depth was about 1200 m and the mean cloud base was around 1000 m. In December

during the PACS Stratus 2004 study, the BL depth reached about 1400 m and the decoupled BL structure dominated (Serpetzoglou et al. 2008). These observations revealed the complex structures and the variability in the BL and the cloud layers. Most of the previous field experiments in the SE Pacific focused on the open ocean area, but the near-coastal marine Sc in the SE Pacific has been largely unexplored.

Wood and Bretherton (2004) estimated BL depth, entrainment rate and decoupling over this region using NCEP reanalysis data and satellite observations. They found that the BL depths over this region are generally 100-200 m deeper than those off the coast of California, and the BLs tend to be less decoupled than those over the coastal regions of the Northeast (NE) Pacific. However, it is difficult to establish the generality of previous studies based on remote sensing observations and reanalysis products due to the absence of *in-situ* observations. Further, previous studies have shown that the coastal BL around 20° S has several features different from the coastal BL north or south of this region (Zuidema et al. 2009; Rahn and Garreaud 2010a). Satellite retrievals show that the monthly mean cloud-top height in the coastal region around 20° S could be about 300 m higher than the surrounding region (Zuidema et al. 2009). Simulation of the observed elevated inversion height in this coastal region is a major challenge for the regional atmospheric numerical modeling community (e.g., Rahn and Garreaud 2010a, b; Wyant et al. 2010; etc.). It has been speculated that since current models can not sufficiently represent the blocking effect of the steep Andes on the flows, simulations tend to produce unrealistically

large divergence in the coastal region, which suppresses the BL depth and thins the cloud layer (Rahn and Garreaud 2010a; Jiang et al. 2010; Wang et al. 2011). *In-situ* observations could help the modeling community improve simulations in the coastal region by offering a variety of measurements within and above the BL. As one component of the five aircraft and two research vessels in the VOCALS experiment (see Chapter 1 for details), the Center for Interdisciplinary Remotely-Piloted Aircraft Studies (CIRPAS) Twin Otter aircraft focused on making observations off the coast of Northern Chile. Comprehensive *in-situ* observations of aerosol, turbulence, cloud properties, and drizzle were also collected. These offered a unique opportunity to acquire first-hand evidence of cloud-aerosol-turbulence interactions in the near-coastal marine Sc over the SE Pacific ocean.

In this study, we combine the *in-situ* aircraft data collected by CIRPAS Twin Otter with meteorological reanalysis, satellite-derived cloud properties, and radiosonde data to explore the BL structure and physical properties of clouds and aerosol over the coastal region in the SE Pacific. The goal is to characterize variations of the near-coastal BL, clouds, and aerosols in the SE Pacific. Section 2.2 describes the aircraft data and the other data supplements. The general synoptic conditions during VOCALS-REx are reviewed in section 2.3. In section 2.4 we investigate the BL vertical structure. The temporal variation of BL structure is provided in section 2.5 followed by the variations of cloud and aerosol properties in section 2.6. Section 2.7 summarizes the general features of the BL, cloud, and aerosol over the near-coastal region in the SE Pacific.

2.2 Data and methodology

2.2.1 Aircraft data

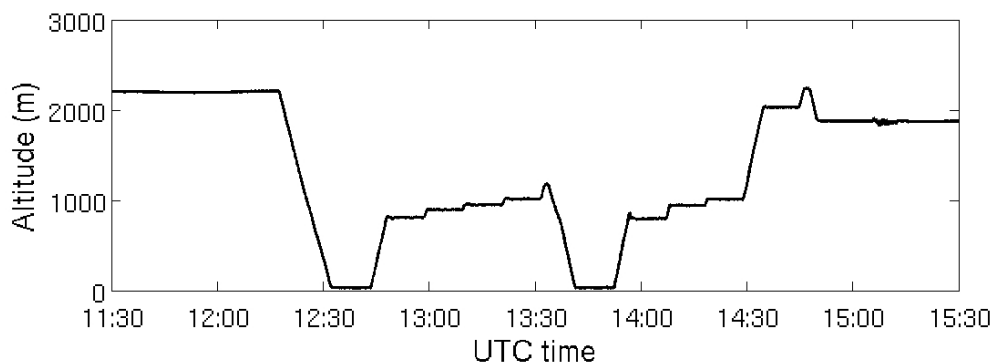


Figure 2.1 Time series of aircraft altitude for Flight RF04 in Table 2.2 (Oct. 21 2008).

The CIRPAS Twin Otter aircraft completed 19 flights in the vicinity of Point Alpha (20° S, 72° W) off the coast of Northern Chile from Oct. 16 to Nov. 13 2008 during VOCALS-REx. Because cloud and aerosol probe data failed on one of those flights (Nov. 5), we only include observations from the other 18 flights in this paper. Each flight had a duration of 4.5 to 5.5 hours and included at least two soundings and several 10-minute horizontal legs near the ocean surface, below the cloud, near the cloud base, within the cloud, near the cloud top, and above the inversion (Fig 2.1). Fifteen of the flights started around 11:00 UTC (07:00 Local Time, LT), with the first sounding made around 12:00 UTC (08:00 LT), while the other three flights took off about 3 hours later (see Table 2.1 for a list of the flights).

Table 2.1 Flight List.

Flight	RF01	RF02	RF03	RF04	RF05	RF06
Date	16-Oct	18-Oct	19-Oct	21-Oct	22-Oct	24-Oct
Time (UTC*)	14:10-18:40	11:10-15:40	10:50-15:40	11:00-15:30	11:00-15:40	11:00-15:50
Descriptor	Typical	Typical	Typical	Typical	Typical	Decoupled, wind shear in BL, cirrus
Flight	RF07	RF08	RF09	RF10	RF11	RF12
Date	26-Oct	27-Oct	29-Oct	30-Oct	1-Nov	2-Nov
Time (UTC*)	11:00-16:00	14:50-19:40	11:00-15:50	10:40-15:50	10:40-16:00	11:00-16:00
Descriptor	Typical	Typical	Decoupled	Wind shear in BL	Moisture above, drizzling	Moisture above, drizzling
Flight	RF13	RF14	RF15	RF16	RF17	RF18
Date	4-Nov	8-Nov	9-Nov	10-Nov	12-Nov	13-Nov
Time (UTC*)	11:00-15:40	11:00-16:00	11:00-15:40	13:20-19:00	11:00-16:00	11:00-15:50
Descriptor	Decoupled, wind shear in BL, cirrus	Double cloud layer, cirrus	Typical	Typical	Typical	Typical

* Local time: UTC -4

The data from the onboard instruments were processed and quality-controlled to provide standard meteorological turbulence, aerosol, cloud, and precipitation observations. This chapter will analyze the measured wind speed, wind direction, vertical velocity, air temperature, air density, pressure, mixing ratio, IR sea surface temperature (SST), and cloud liquid water content (LWC) from the PVM-100 probe (Gerber et al. 1994) at a frequency of 10 Hz. The cloud

Table 2.2 Instrumentation on Twin Otter during VOCALS-REx.

Instrument	Observations	Variables
Standard meteorological instruments	Winds, air temperature, dewpoint, cloud liquid water content, surface temperature	u, v, w, T, T_d , LWC, pressure, SST
Turbulence Probes	High speed wind, temperature, and moisture	u, v, w, T , pressure, q_v
Gerber Probe	Liquid water	LWC
Cloud Imaging Probe (CIP)	Drizzle droplet size range: 15.5-1500 μm	Drizzle water content
CPCs	Ultrafine aerosols	Ultrafine aerosol concentration
CCN Spectrometer	CCN at 0.2% super-saturation	CCN
Passive Cavity Aerosol Spectrometer Probe (PCASP)	Aerosol size range: 0.1-2 μm	Accumulation mode aerosol concentration
Cloud, Aerosol and Precipitation Spectrometer (CAPS)	Cloud droplet size range: 2.07-40.2 μm	Cloud droplet concentration

and aerosol data obtained at 1 Hz include accumulation mode aerosol (size range: 0.1- 2 μm) concentration (N_a) from the Passive Cavity Aerosol Spectrometer Probe (PCASP), N_d from the measurements by the Cloud, Aerosol and Precipitation probe (CAS), cloud condensation nuclei (CCN) from the CCN Spectrometer, effective radius of cloud droplets (R_e) from the PVM-100 probe, and drizzle water content from the Cloud Imaging Probe (CIP). Uncertainties for aerosols and cloud droplet concentrations measured by these probes are estimated to be within 15% in the sample flow. Table 2.2 describes the relevant instruments onboard. Two conserved variables during adiabatic processes will be

mainly used to estimate the BL structure in the next sections: the total water mixing ratio $q_t = q_v + \frac{LWC}{\rho_{air}}$, where q_v is the water vapor mixing ratio, and the liquid water potential temperature (Betts 1973) $\theta_l = \theta - \frac{\theta}{T} \frac{L}{c_p} q_l$, where θ is the potential temperature, T is the air temperature, $L = 2450 \text{ KJ kg}^{-1}$ is the latent heat of vaporation at 20°C , and $c_p = 1015 \text{ J kg}^{-1} \text{ K}^{-1}$ is the isobaric specific heat of moist air, q_l is the liquid water specific humidity.

2.2.2 Reanalysis data, satellite measurements, and radiosonde data

Previous studies suggest that large-scale dynamic forcing impacts the Sc properties on both the inter-seasonal and synoptic time-scales (Klein and Hartmann 1993; Rozendaal and Rossow 2003). The large-scale datasets, including meteorological reanalyses and satellite observations, along with soundings launched in the nearby region, provide a comprehensive data supply for exploring the large-scale background of the BL at Point Alpha.

We adopt the reanalysis of meteorological observations from the National Centers for Environmental Prediction (NCEP) /NCAR Reanalysis Project (NNRP, Kistler et al. 2001) to study the sea level pressure and the 700-hPa geopotential height over the large region (50° W - 95° W , 0° - 45° S). The resolution of the NCEP NNRP data is $2.5^\circ \times 2.5^\circ \times 17$ pressure levels and this data product is available at 6 hour intervals. The resolution of this product is suitable for evaluating the large-scale patterns of sea level pressure and 700-hPa geopotential height. The same analyses with the ECMWF Interim reanalysis indicate that the results are insensitive to the different reanalysis products.

Radiances from the Tenth Geostationary Operational Environmental

Satellite (GOES-10) were used to retrieve cloud properties at 4-km resolution with the methods of Minnis et al. (2011a) for the area (75.75° W- 70.75° W 23.75° S- 16.25° S) in the vicinity of Point Alpha during VOCALS-REx. Wood et al. (2011) provide further description and examples of the GOES VOCALS-Rex retrievals. Cloud properties were also retrieved from 1-km Terra MODerate-resolution Imaging Spectroradiometer (MODIS) data using the same algorithms applied to the GOES-10 data (Minnis et al. 2011b). In addition, the Quick Scatterometer (QuikSCAT) L3 data provides $0.25^{\circ} \times 0.25^{\circ}$ resolution surface wind twice per day. The QuikSCAT surface wind field is used to estimate the average surface divergence at Point Alpha.

During VOCALS-REx an NCAR/EOL GPS Advanced Upper-Air Sounding (GAUS) system located in Iquique, Chile (70.1° W, 20.3° S) launched Vaisala RS92 radiosondes 6 times per day. This radiosonde delivers high quality wind measurements, pressure, temperature, and humidity measurements. We adopt the radiosonde data as a supplement to describe the BL structure on the coast and compare it with that from the Point Alpha aircraft observations. Because of the diurnal cycle of continental BL and the direct influence of the Andes, the BL involves more complicated processes at this on-shore location, especially during the daytime. Although the radiosonde data have no liquid water information, the satellite retrievals indicate that the mean LWP over this near-coastal region is less than 30 g m^{-2} during the observations, as will be shown in section 3. We assume that ignoring the contribution of liquid water to total water mixing ratio will not change the mean BL thermodynamic structure. Therefore, the potential

temperature (θ) and water vapor mixing ratio (q_v) calculated from the radiosonde data represent the BL thermodynamic structure.

2.2.3 Back-trajectories

To help establish the history of the air masses sampled by the aircraft, we use the Hybrid Single Particle Lagrangian Integrated Trajectory Model (HYSPLIT, Draxler and Rolph 2011) to calculate back trajectories starting at Point Alpha. HYSPLIT can be set up to compute two-dimensional and three-dimensional parcel trajectories with a simple advection calculation. The input meteorological gridded data is the NCEP Global Data Assimilation System (GDAS) data with $1^\circ \times 1^\circ$ resolution. For each flight, two-dimensional parcel trajectories starting at the 500-m level (within the BL) and three-dimensional parcel trajectories starting at the 2000-m level (free atmosphere) are calculated for 48 hours prior to the flight time.

2.3. General synoptic conditions and variations

2.3.1 Synoptic patterns from NCEP reanalysis

A rough picture of the large-scale meteorological conditions over the study period is given by the composite fields of sea level pressure and 700-hPa geopotential height from NCEP reanalysis. The mean sea level pressure (Fig. 2.2a) from Oct. 16 to Nov. 13 2008 was controlled by the strength and location of the subtropical high and a low-level trough that extended from the equator along the coast to 25°S east of the northeast part of the subtropical high. The low-level trough, the subtropical high system, and the topography along the coast interact to produce conditions and processes unique to the near-coastal area (Garreaud

and Munoz 2004, 2005). The mean 700-hPa geopotential height (Fig. 2.2b) shows that a mid-latitude trough reached 20° S between the subtropical high and Point Alpha. This indicates that the study region was influenced by the subtropical high system, and the mid-latitude trough.

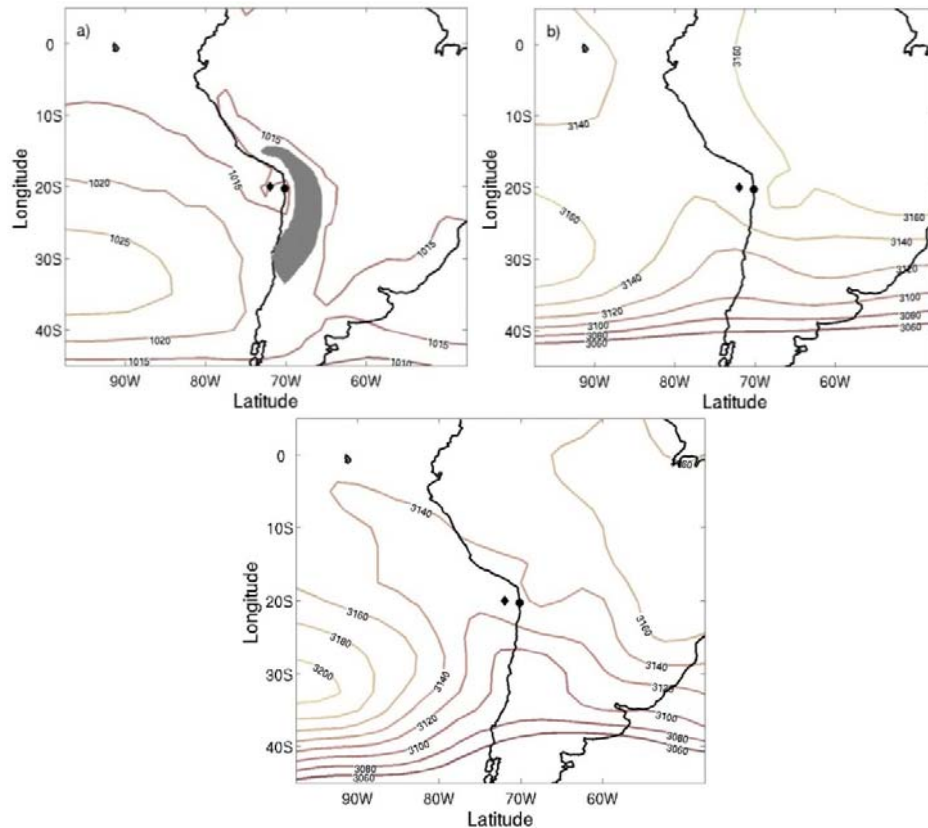


Figure 2.2 a) Composite Sea Level Pressure (Oct.16– Nov.13 2008). The contours are every 2 hPa. The Andes region is shaded to avoid the artificially high sea level pressure region due to the high altitude; b) Composite 700-hPa geopotential height; c) 700-hPa geopotential height at 12:00UTC Nov. 1, 2008. The contours are every 20 m. The black diamond marks Point Alpha, and the black dot indicates the location of Iquique. The coastal outline is shown as a black solid line.

Since this study occurred during the local austral spring season, the daily sea level pressure fields (not shown here) show that, the SE Pacific high system

was strongest during the first several days (Oct. 16 –Oct. 18), with the 1020-hPa isobar extending over the ocean area south of 20° S. As the study progressed, the SE Pacific high system weakened and varied due to the mid-latitude wave activity. At the end of the study period, the 1020-hPa isobar moved to the open ocean area south of 25° S and west of 80° W. The day-to-day 700-hPa geopotential height (not shown here) exhibited patterns with troughs developing from the mid-latitudes extending to north of 25° S (Oct. 29 - Nov. 2, Nov. 13). Meanwhile the subtropical high was strong and occupied the region west of 80° W. Therefore, the longitudinal component of the general flow over this region increased during these troughing periods.

2.3.2 Composite cloud properties from satellite observations

As noted in section 2.1, every flight mission time was about 4.5-5.5 hours (see Table 2.1). During the flight missions, the GOES-derived cloud properties were available every 30 minutes. To estimate the mean conditions of the large-scale cloud background, we averaged the GOES-derived low cloud amount (%), liquid water path (LWP; g m^{-2}), and R_e to a horizontal resolution of $0.5^\circ \times 0.5^\circ$ when the aircraft was flying.

During the flight observing times, the mean low cloud amount (Fig. 2.3a) around Point Alpha was around 70%, which was about 10% lower than that over the open ocean west of 73° W. The coastal region had less than 60% cloud amount except for a long narrow band extending from (17° S, 74° W) to (19° S, 71.5° W) with cloud amounts > 80%. A climatological study using 18 years of satellite measurements (O' Dell et al. 2008) shows that the cloud LWP over the

coastal region exhibits a doubly peaked diurnal cycle in October, with peaks at 11:00 and 23:00 UTC (07:00 and 19:00 LT) , the former of which is around the flight observing time. Therefore, the long narrow band with high cloud amounts and LWP mentioned above could be a part of the diurnal cycle and be linked to a wave of positive vertical velocity driven by the topography of the Andes moving from the coast of Peru in the late afternoon (Garreaud and Muñoz 2004).

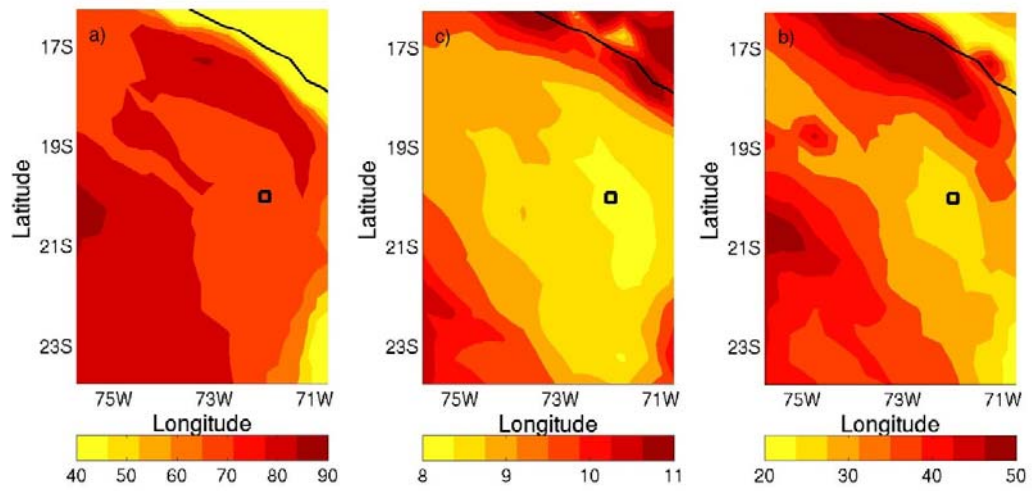


Figure 2.3 The average fields of a) Low cloud amount (%), b) LWP (g m^{-2}), c) R_e (micron) derived from GOES-10 data during the flight time (see Table 1). Point Alpha is marked as the blue square box.

The GOES-10 average cloud LWP over Point Alpha during the observing time periods was about 27 g m^{-2} , and it increased westward to the value of about 43 g m^{-2} around 75°W , 20°S (Fig. 2.3b). R_e over Point Alpha averaged less than $8.5 \text{ }\mu\text{m}$ (Fig. 2.3c), while R_e offshore was greater than $9.5 \text{ }\mu\text{m}$. The satellite retrievals during the observation time indicate that clouds over the study region were generally thin, bright and slightly broken compared with those in the adjoining areas possibly due to both meteorological and aerosol forcing.

Because QuikSCAT winds over this study area were available from two passes per day and the available time was random, it is impossible to estimate the surface divergence field during the aircraft mission time. Therefore, we averaged all 58 QuikSCAT surface wind passes over this study area from Oct. 16 to Nov. 13, 2008 to estimate the climatological features of the surface wind and divergence fields during VOCALS_REx. The average surface divergence (Oct. 16- Nov. 13) field from QuikSCAT winds (Fig. 2.4) reflects the complexity of this field in the near-coastal regions and the sensitivity of the divergence calculations to the retrieved wind field, which is smoothed by time averaging. The entire indicated area was mainly controlled by divergence related to large-scale subsidence above the inversion, except in the narrow convergence zone along the coast east of Point Alpha due to the topography of the steep Andes as mentioned in a previous study (Rahn and Garreaud 2010a). The average surface divergence at Point Alpha is about $3 \times 10^{-6} \text{ s}^{-1}$. However, its variability might be large since Point Alpha is located near the transition zone between the typical subtropical Sc deck with strong surface divergence and the coastal area impacted by mesoscale processes such as gravity waves moving from the coastline (Rahn and Garreaud 2010a). Further, since the QuikSCAT winds were available whenever the measurement swath of QuikSCAT covered this region, the composite surface wind and divergence fields include diurnal variations. The surface divergence from ECMWF Interim reanalysis with a horizontal resolution of $0.7^\circ \times 0.7^\circ$ is $-1 \times 10^{-6} \text{ s}^{-1}$.

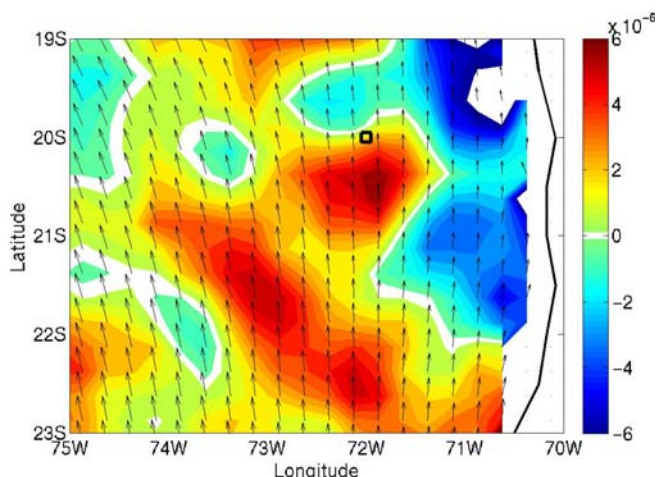


Figure 2.4 The average surface wind (vectors) and divergence (color shading, increment= $2 \times 10^{-6} \text{ s}^{-1}$) from QuikSCAT (Oct.16– Nov.13 2008). Point Alpha is marked as the blue square box.

2.3.3 Back trajectories

The back trajectories for the observed air masses at Point Alpha indicate that for the 18 flights the air masses within the BL (Fig. 2.5a) were mainly from the coastal regions south of Point Alpha, 48 hours prior to observation. The air masses traveled toward Point Alpha over the ocean. The trajectories also indicate that most of the observed air masses stayed over the ocean for more than 24 hours prior to the flights, and were advected by southerly to southwesterly flows. The air masses above the inversion (Fig. 2.5b) traveled longer distances and came from a wider variety of directions than those within the BL due to synoptic variability 48 hours prior to the observations. The trajectory histories of the above-inversion air masses are as follows: north of Point Alpha along the coast of Peru during 4 flights; in the vicinity of Point Alpha during 7 flights; over the continent during 1 flight; over the ocean west of 77° W

during 5 flights; and over the ocean and south of Point Alpha during only 1 flight. The flight observations (as shown in the next section) and the numerical simulations (Garreaud and Muñoz 2005; Wang et al. 2011) indicate that the horizontal winds switch directions between the BL and above the inversion over the region due to the thermal wind balance and the blocking of the Andes. Overall, the back trajectories indicated that most of the above-inversion air masses moved in a direction opposite to those of the air masses within the BL. The back trajectories at 3000m (not shown here) are generally similar to the back trajectories at 2000m, indicating that even there are strong stratifications near the inversion, the middle-level flows (2000-3000 m) above inversion were generally similar.

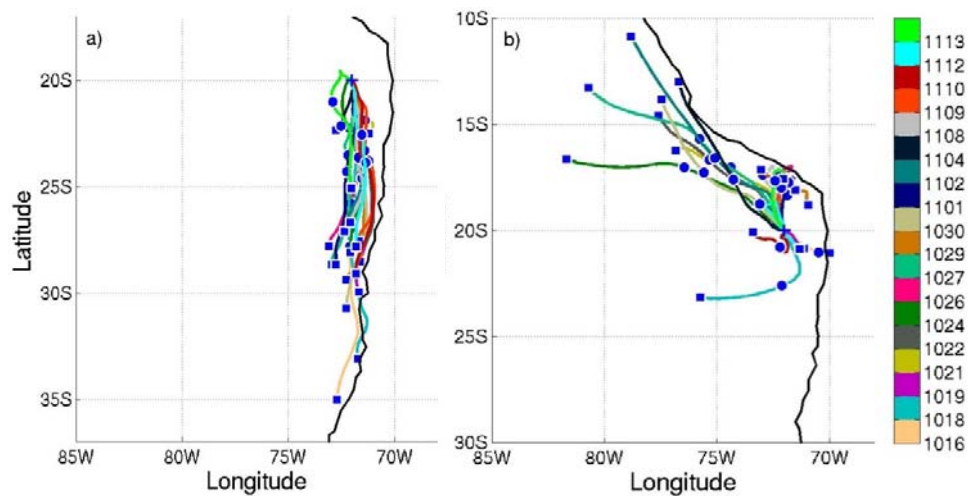


Figure 2.5 a) Two-dimensional isobaric back trajectories starting at 500 m from Point Alpha (Plus sign) for the 18 cases (color bar) with the 24-hour point (Blue Circle), and the 48-hour point (Square); b) Three-dimensional back trajectories starting at 2000 m from Point Alpha.

2.3.4 Synoptic variations

Time evolution of sea level pressure and 700-hPa geopotential height around Point Alpha and Iquique indicate that the synoptic pattern over the near-coastal region did not vary as much as over the open ocean south of 25° S (Fig. 2.6). The NCEP sea level pressure at Point Alpha fluctuated between 1013 and 1018 hPa. The sea level pressure was also estimated from the aircraft 30-m level observations of pressure and virtual temperature on each day; these estimates tended to be about 3 hPa higher than the NCEP values. Both showed the sea level pressure at Point Alpha gradually decreasing by about 5 hPa by the end of the study period; however, the magnitude of the pressure change is not significant enough to be considered a seasonal signal because of the uncertainty of data and the potential synoptic variations. The NCEP 700-hPa geopotential height at Point Alpha revealed a relatively constant pattern and varied from 3130 to 3180 m during the study period. Three 700-hPa geopotential height minima occurred on Oct. 22, Nov. 1 (Fig. 2.2c), and Nov. 13. Meanwhile, the NCEP 700-hPa geopotential height at Iquique showed the same minima on the same days, which might be linked to midlevel troughs. Comparing these results with the 700-hPa geopotential height calculated from the Iquique radiosonde measurements, the NCEP 700-hPa geopotential height was about 25 m higher in October, and the bias clearly decreased in November. The synoptic evolution over this region altered the BL depth, the low-level wind, and the moisture properties, which will be discussed in the next sections.

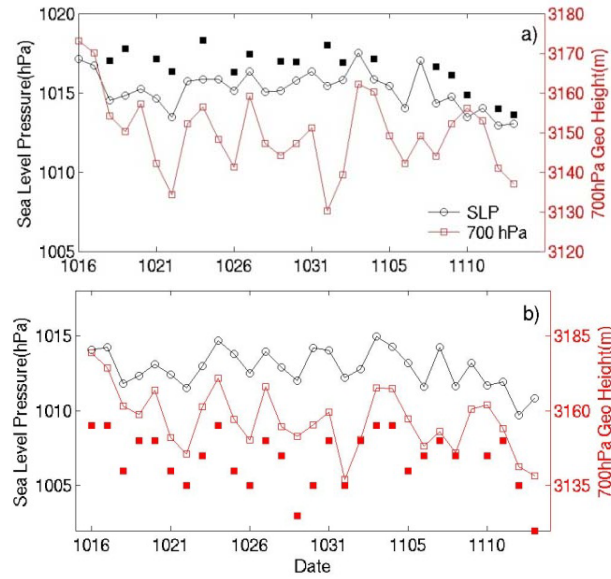


Figure 2.6 Synthesis of sea level pressure and 700hPa geopotential height a) at Point Alpha from NCEP reanalysis (12:00 UTC, open symbols) and aircraft observations (~12:00 UTC, solid symbols); b) at Iquique from NCEP reanalysis (12:00 UTC, open symbols) and radiosonde data (~12:00 UTC, solid symbols).

2.4 Boundary layer vertical structure

2.4.1 Thermodynamic profiles

The typical Sc topped BL is well mixed and capped by a strong inversion (Albrecht et al. 1988). Previous studies have revealed that the inversion height (z_i) could be an important indicator of the structure of the BL in terms of decoupling, cloud cover, etc. (Albrecht et al. 1995a). However, excluding the variation of z_i could help better estimate the composite thermodynamic and dynamic structures within the BL. In this study, z_i is quantified as the height at which the vertical gradient of θ_i is the largest. Figure 2.7a-c shows the profiles of θ_i , q_i , and LWC using a height scale normalized by z_i . In general, the profiles of θ_i and q_i show a well-mixed BL capped by a sharp inversion during most of the

flights. Within the BL θ_l was about 289 K and the change across the inversion (denoted by $\Delta\theta_l$) ranged from 10 to 17 K. The average q_t within the boundary layer was about 7.6 g kg^{-1} and the change across the inversion (denoted by Δq_t) varied from +2 to -8 g kg^{-1} (Table 2.3). During most of the flights q_t decreased sharply above the inversion. However, during two of the flights (Nov. 1-2), $\Delta\theta_l$ was relatively small, and q_t increased above the inversion due to a moist layer above the inversion related to the synoptic system discussed above. The soundings launched at Iquique also captured the moist layer above the inversion from Oct. 31 to Nov. 8 (Fig. 2.8a) and the time-height diagram of the meridional winds at Iquique (not shown) indicate a clear southerly wind above the inversion around the similar period. The enhanced southerly wind from Oct. 31 to Nov. 8 combined with the 700-hPa geopotential height minima on Nov.1 and the following increasing (Fig. 2.6b) may be due to synoptic systems that passed by and modified the flow pattern in this region. The time-height diagram of the potential temperature at Iquique (Fig. 2.8b) shows that the BL depth varied between 700 m and 1400 m over the course of the observation period.

To quantify how well mixed the BL was, we calculated the decoupling parameters α_q and α_θ (Wood and Bretherton, 2004), which measure the relative difference between the surface and the upper part of the BL.

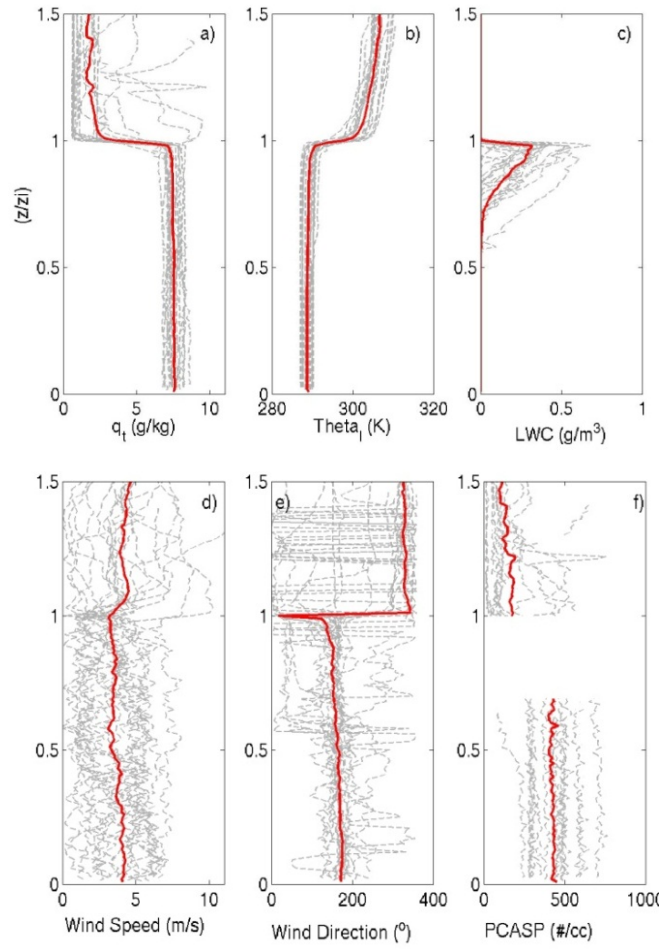


Figure 2.7 Profiles scaled by the PBL heights. a) total-water mixing ratio (g kg^{-1}); b) liquid water potential temperature (K); c) LWC (g m^{-3}); d) wind speed (ms^{-1}); e) wind direction (degree), and f) N_a from PCASP (\#cm^{-3}) for all 18 flights. The gray lines indicate all individual flights, and the red solid lines show the composite soundings.

$$\alpha_\theta = \frac{\theta_l(z_i^-) - \theta_l(0)}{\theta_l(z_i^+) - \theta_l(0)} \quad (2.1)$$

$$\alpha_q = \frac{q_t(z_i^-) - q_t(0)}{q_t(z_i^+) - q_t(0)} \quad (2.2)$$

where z_i^+ / z_i^- is the level 25 m above/below the inversion, $\theta_l(z)$ and $q_t(z)$ are θ_l and q_t at z , $\theta_l(0)$ and $q_t(0)$ are at the surface.

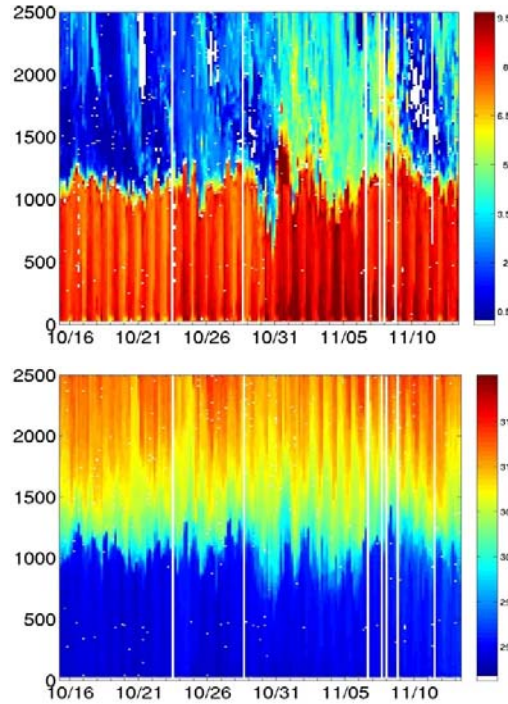


Figure 2.8 Time–height section of (top) mixing ratio (g kg^{-1}); (bottom) potential temperature (K) from the soundings launched at Iquique during VOCALS-REx.

If these values are close to zero, the BL tends to be completely well-mixed. However, the BL is not always completely well-mixed due to solar radiation, drizzle, and BL deepening. Previous observations (e.g., Albrecht et al. 1995a) suggest that if α_q exceeds a certain value (~ 0.3), which indicates that the upper part of the BL is clearly drier than the lower BL, the BL is decoupled. Thus the Sc layer may breakup and transition to trade wind cumulus conditions.

Values of α_q and α_θ from each flight sounding were calculated and their respective averages are 0.08 ± 0.06 and 0.14 ± 0.09 , which are within the regime of “well-mixed”. The results imply that for most of this season the BL over Point Alpha was well-mixed ($\alpha_q < 0.1$ and $\alpha_\theta < 0.15$), except for Oct. 29, Nov. 1–2, Nov. 4 and Nov. 8. On Oct. 29, Nov. 4, and Nov. 8, the BL was decoupled and some

small cumulus developed below the Sc layer as indicated by the LWC profiles and the flight reports. Because of the synoptic forcing (Nov. 1 and Nov. 2, Fig. 2.2c and Fig. 2.6b), the air above the inversion was no longer dry. On Nov. 1, an α_θ of 0.42 reflects that drizzle processes enhanced the BL decoupling. The BL on Nov. 2 with an α_θ of 0.15 was less decoupled than that on Nov. 1.

Table 2.3 Mean values of boundary layer at Point Alpha during VOCALS-REx.

Project	VOCALS Twin Otter
Location	20° S 72° W
Time	Oct.16 - Nov.13
Sc Regime	SE Pacific coastal region
z_i (m)	1140±120
θ_l (K)	289.5±1.2
$\Delta\theta_l$ (K)	11.8±1.9
q_t (gkg ⁻¹)	7.2±0.5
Δq_t (gkg ⁻¹)	-5.2±2.2
α_θ	0.14±0.09
α_q	0.08±0.06
ω_e (mms ⁻¹)	2.0±1.4
F_L (W m ⁻²)	48.5±15.5
F_θ (W m ⁻²)	7.1±2.5
$F_{\theta v}$ (W m ⁻²)	9.7±2.7
SST (°C)	18±1.0

2.4.2 Wind profiles

The vertical profiles of the horizontal wind are shown in Fig. 2.7d-e. On most of the flight days, the wind speed and wind direction were nearly constant within the BL. The wind speed within the BL ranged between 1 and 7 m s⁻¹ with an average value of ~ 4 m s⁻¹, which is lower than the BL wind speed (> 7 m s⁻¹) over the remote ocean during VOCALS-REx (Bretherton et al. 2010; Wang et al.

2011). The wind speed at Point Alpha was also lower than the average BL wind speed of 7-8 m s⁻¹ off the southern California coast during DYCOMS-II (Stevens et al. 2003). The wind direction below the inversion was mostly southerly (150°-250°), turning to northerly (270°-30°) above the inversion.

On Oct. 24 and Nov. 4, the wind direction shifted sharply from southerly to northerly in the upper part of the BL. The wind direction on Oct. 30 shifted from southerly to easterly in the upper part of the BL. The horizontal legs of observations within the BL on these three days showed the same wind patterns, which confirmed that the observed vertical wind shear within the BL was not due to sampling errors (Fig. 2.9). This type of directional wind shear within the BL is not common and is probably linked to coastal processes such as the propagation of the upsidence wave (Garreaud and Muñoz 2004; Rahn and Garreaud 2010b).

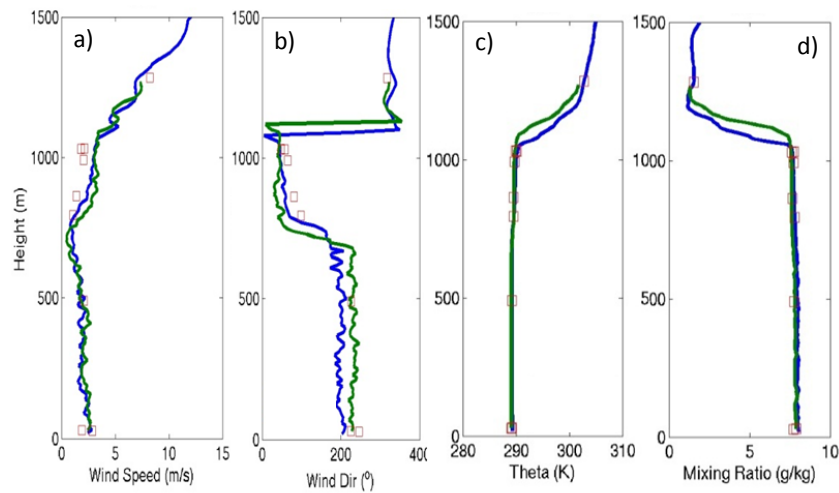


Figure 2.9 The soundings of a) wind speed, b) wind direction, c) potential temperature and d) mixing ratio on Oct. 24. The average values from the horizontal legs are denoted as red squares.

2.4.3 Turbulence structure

On each flight day, several 10-minute legs were flown at different levels. The turbulence and thermodynamic data gathered from these legs were processed to calculate the vertical distributions of leg-mean vertical velocity variance $\overline{w'w'}$, the total water flux F_{qt} , and the liquid water potential temperature flux F_{θ_l} for all of the flights (Fig. 2.10) from Eq. 2.3-4:

$$F_{qt} = L_v \bar{\rho} \overline{w'q_t'} \quad (2.3)$$

$$F_{\theta_l} = C_p \bar{\rho} \overline{w'\theta_l'} \quad (2.4)$$

where $L_v = 2.45 \times 10^6 \text{ J kg}^{-1}$ is the latent heat of vaporization at 20°C , $\bar{\rho}$ is the air density, $C_p = 1005 \text{ J kg}^{-1} \text{ K}^{-1}$ is the specific heat of air.

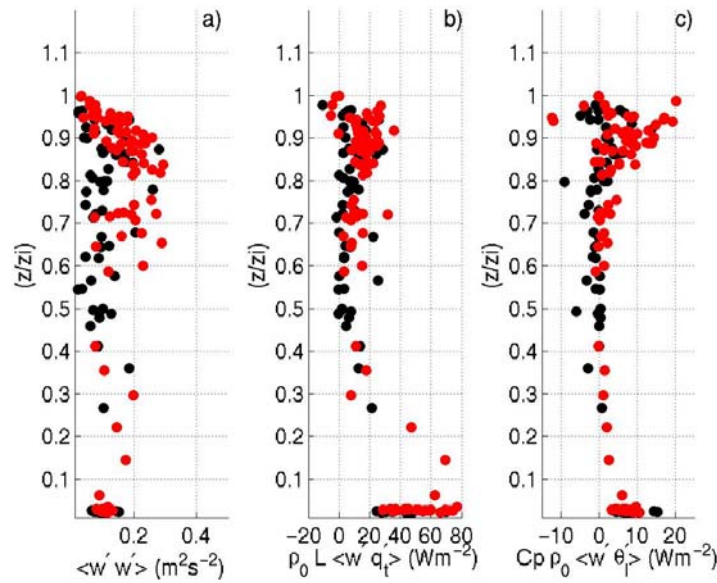


Figure 2.10 a) Vertical velocity variance (m^2s^{-2}), b) Total water flux (W m^{-2}), and c) Liquid water potential temperature flux (W m^{-2}) vs. normalized height calculated from all the flight legs for the 18 flights. Red solid symbols (10 flights) are the typical well-mixed boundary layer, non-drizzling Sc discussed in Zheng et al. 2010, black solid symbols (8 flights) are the cases with complications involving strong wind shear within the BL, moist layers above the inversion, strong decoupled BL with cumulus below Sc.

The normalized cloud base heights were between 0.6 and 0.8 for most of the cases (Fig. 2.7c). In the lower part of the BL ($z/z_i < 0.6$), $\overline{w'w'}$ ranged from 0.05 to 0.30 $\text{m}^2 \text{s}^{-2}$, and near the cloud base or within the cloud layer the values vary substantially. For most of the flights, F_{qt} varied between 20 and 80 W m^{-2} near the surface, and then decreased with height in the lower part of the BL. F_{θ_l} ranged between -10 and 15 W m^{-2} below the cloud and generally decreased with height. Therefore, F_{qt} tended to moisten the BL at a rate of 1.5 $\text{g kg}^{-1} \text{day}^{-1}$, and F_{θ_l} heated the lower BL at a rate of about 1 K day^{-1} . The southerly low-level wind along the coast brought cold and dry air from the south. Based on the soundings launched along the coastline during VOCALS-REx (Rahn and Garreaud 2010a), a rough estimate of the temperature tendency due to horizontal advection was about -1 K day^{-1} , which could approximately balance the warming by the vertical sensible heat fluxes. Near the cloud top, F_{θ_l} reached about 20 W m^{-2} in some flights due to cloud top radiative cooling. Within the cloud layers, F_{qt} increased and then decreased rapidly with height. The values reflect the considerable flight-to-flight diversity. Since F_{θ_l} and F_{qt} on most flight days had minima near the cloud, the turbulence structure showed some tendency of decoupling, probably due to the solar radiation. The thermodynamic profiles shown in Fig. 2.7, however, indicated the BL during the flight mission time was well-mixed. The observed in-cloud vertical velocity variance ($\overline{w'w'}$) at Point Alpha was systematically lower than that over the remote ocean area (80° W-85° W, 20° S), which had an estimated mean value of about 0.36 $\text{m}^2 \text{s}^{-2}$ during VOCALS-REx (Bretherton et al. 2010). The aircraft measurements of a nocturnal

non-drizzling marine Sc off the southern California coast during the first research flight of DYCOMS-II (Stevens et al. 2005) also revealed a stronger turbulence structure than that at Point Alpha. In their observations, the in-cloud $\overline{w'w'}$ was larger than $0.4 \text{ m}^2 \text{ s}^{-2}$, and the maximum of $0.5 \text{ m}^2 \text{ s}^{-2}$ was near cloud base. The different measurements and calculation methods from their studies and this study, however, may partly affect the values as well.

2.5 Temporal variation of BL structure

2.5.1 BL depth variation

Figure 2.11 shows the time series of inversion height z_i measured from the aircraft soundings data at Point Alpha. It increased from about 1000 m at the beginning of the study period to about 1200 m by the end. On Oct. 29 and Nov. 4, inversions at 1300 m and 1450 m respectively were observed. The BLs on those days were decoupled and small cumuli were observed below the Sc layer. There was a transition zone at the top of the BL, where entrainment processes were critical to the growth of the BL, the evolution of cloud depth, etc. We call this the entrainment zone, and define it based on the soundings (air temperature, q_t , LWC, etc.). The bottom of the entrainment zone is defined as the level where the soundings clearly started losing the BL feature and transiting to the free troposphere, while the top of the entrainment zone is the level where these soundings totally lose the BL features. The entrainment zone (Fig. 2.11) was less than 50 m thick at the beginning and the end of the study period indicating that the BL inversion is very sharp; however, there were 3 days (Oct. 24, 27 and Nov. 4) when an entrainment zone thicker than 100 m was observed. The thicker

entrainment zone reflects an interaction between the BL and the free air aloft that extended over a very large depth and can be linked to the strong vertical wind shear within the BL on Oct. 24 and Nov. 4 as mentioned before. On Oct. 27, the flight started around 15:00 UTC (11:00 LT), i.e., later than the usual 12:00 UTC (08:00 LT), which may also be a factor. The inversion levels from early morning soundings (07:00 UTC, 03:00 LT) launched at Iquique (Fig. 2.11), show that the BL structure at Iquique was more complicated than that at Point Alpha due to land surface and topography effects. The BL at Iquique showed double inversions on 5-6 days during the study, and thus the BL depth varied more significantly than that at Point Alpha. On average, z_i at Iquique was about 1070 ± 190 m, which was close to the BL depth at Point Alpha.

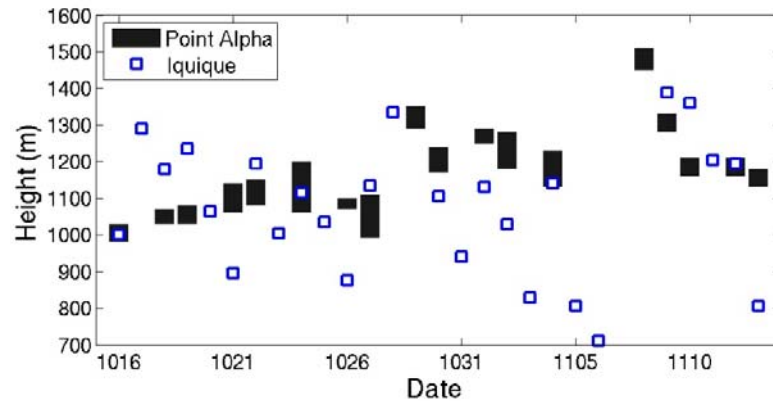


Figure 2.11 Synthesis of the inversion level at Point Alpha from flight data, and at Iquique from radiosonde data. The open squares indicate the early morning soundings (~07:00 UTC), and the black bar shows the inversion zone for each case.

2.5.2 Cloud LWP variation

The average sounding of LWC from the PVM-100 probe was integrated to represent the cloud LWP. The LWP in this study was integrated with the average profile of LWC from two soundings on each day rather than with the 12:00 UTC

(08:00 LT) soundings only (Zheng et al. 2010). Therefore, the LWP values in this study are slightly different from the values in Zheng et al. (2010). The LWC observations from the 10-minute horizontal legs within the cloud layer provide the spatial distribution of LWC. We used the standardized differences (%) between the averaged LWC from the in-cloud leg $\langle LWC_{leg}(z) \rangle$ and the sounding LWC at the same altitude $LWC_{profile}(z)$ to estimate the uncertainty range of the LWP estimate (Fig. 2.12):

$$error(\%) = \frac{|LWC_{profile}(z) - \langle LWC_{leg}(z) \rangle|}{LWC_{profile}(z)} \times 100 \quad (2.5)$$

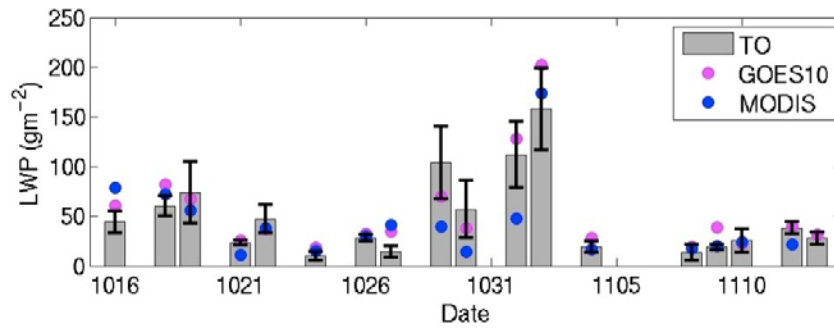


Figure 2.12 LWP integrated from aircraft soundings on all flight days. The estimated errors in LWP from Eq. 2.5 are indicated by the error bars. Magenta symbols are GOES retrievals averaged for each entire flight mission over an area within a radius of 20 km of Point Alpha. Blue symbols are average Terra MODIS retrievals for a 0.5° region centered on Point Alpha taken at between 14:20 and 15:50 UTC.

The uncertainties associated with the cloud water variances along the in-cloud leg, the sloping profiles flown, etc. are not included in the error formula, which might increase the uncertainty of the LWP estimate in highly inhomogeneous cloud layers. The observed cloud LWP ranged from less than 20 g m^{-2} to about 180 g m^{-2} . The GOES-derived cloud LWPs averaged over an area within a 20 km radius of the *in-situ* aircraft observations locations and the 0.5° -

average Terra LWPs over Point Alpha at ~15:00 UTC (11:00 LT) are generally close to those from the aircraft. This close correspondence further indicates that the observed clouds were nearly solid and homogeneous on most days during the aircraft observations, conditions for which the satellite retrievals perform best. The Terra LWP is less than the GOES average values on most days, primarily because the Terra measurements mostly occurred at the end of the flights when the clouds had thinned out. No Terra retrieval was obtained on 13 November. According to the GOES retrievals for all of the flights, the average LWP at 12:45 UTC (08:45 LT) was 62.0 g m^{-2} compared to 33.9 at 15:30 UTC (11:30 LT). For all 18 flights, the average *in-situ* LWP was 48.5 g m^{-2} . The GOES LWP values were, on an average flight day, $6.7 \pm 18.4 \text{ g m}^{-2}$ greater than the *in-situ* values and had a squared correlation coefficient $R^2 = 0.84$. The MODIS average is $6.3 \pm 27.4 \text{ g m}^{-2}$ less than the *in-situ* values with $R^2 = 0.59$. However, the MODIS average LWP is only $0.8 + 8.0 \text{ g m}^{-2}$ less than the GOES averages over Point Alpha at the times of the Terra overpasses for all 17 days. For those data, $R^2 = 0.98$.

The highest cloud LWP values of 112 ± 33 and $158 \pm 41 \text{ g m}^{-2}$, occurred on Nov. 1 and Nov. 2, respectively, on which days a moist layer above the inversion moved to this study region (Fig. 2.8a). The third highest LWP ($105 \pm 36 \text{ g m}^{-2}$) occurred on Oct. 29, when the BL was clearly decoupled and its depth reached 1300 m. On the days with vertical wind shear within the BL (Oct. 24 and Nov. 4), the BL was decoupled with thin and broken Sc, and the cloud LWPs were 10 ± 4 and $19 \pm 6 \text{ g m}^{-2}$, respectively. The cloud LWPs on the two decoupled days (Nov. 8 and Nov. 13) were 13 ± 8 and $28 \pm 6 \text{ g m}^{-2}$, respectively. From Fig. 2.12, the cloud

LWPs were about 50 g m^{-2} before Oct. 29 when a synoptic system affected conditions at Point Alpha. From this point in time to Nov. 2 the cloud LWP appears to be mainly controlled by synoptic disturbances.

2.5.3 Inversion and surface conditions

The inversion strength, Δq_t and $\Delta \theta_l$, indicates the extent to which the BL can resist the entrainment of the dry, warm air from the free atmosphere aloft.

$$\Delta \theta_l = \theta_l(z_i^+) - \theta_l(z_i^-) \quad (2.6)$$

$$\Delta q_t = q_t(z_i^+) - q_t(z_i^-) \quad (2.7)$$

The typical Sc-topped BL has large inversion strength in terms of Δq_t and $\Delta \theta_l$ (Albrecht et al. 1988; Serpetzoglou et al. 2009). Figure 2.13 shows that $\Delta \theta_l$ decreased to 8 K on Nov. 1, when the moist layer was observed above the inversion. From Nov. 4, $\Delta \theta_l$ was relatively consistent around 15 K until it decreased to around 12 K on Nov. 13, Δq_t was less than -4.8 g kg^{-1} on most flight days except Nov. 1-2 when a moist layer above the inversion moved to this location (as shown in Figs. 2.7-8). The inversion strength at Iquique appeared weaker than that at Point Alpha on almost all the days. From Oct. 31 to Nov. 13 the inversion strength at Iquique was clearly weaker than the earlier days of the study period, which is consistent with the water mixing ratio and the potential temperature pattern (Fig. 2.8).

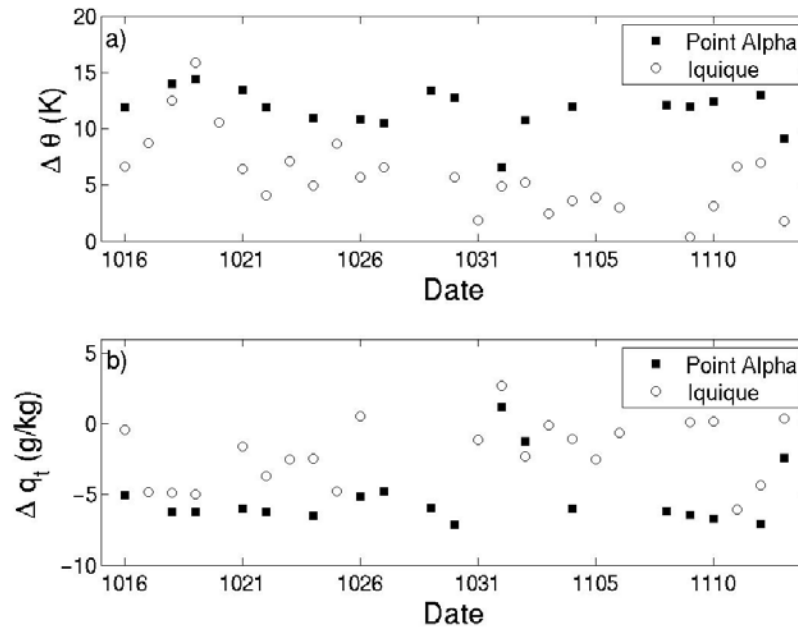


Figure 2.13 a) $\Delta \theta$ (K); b) Δq_t (g kg⁻¹). The solid squares represent the values at Point Alpha measured by the aircraft, and the open circles donate the values at Iquique measured by the radiosonde system.

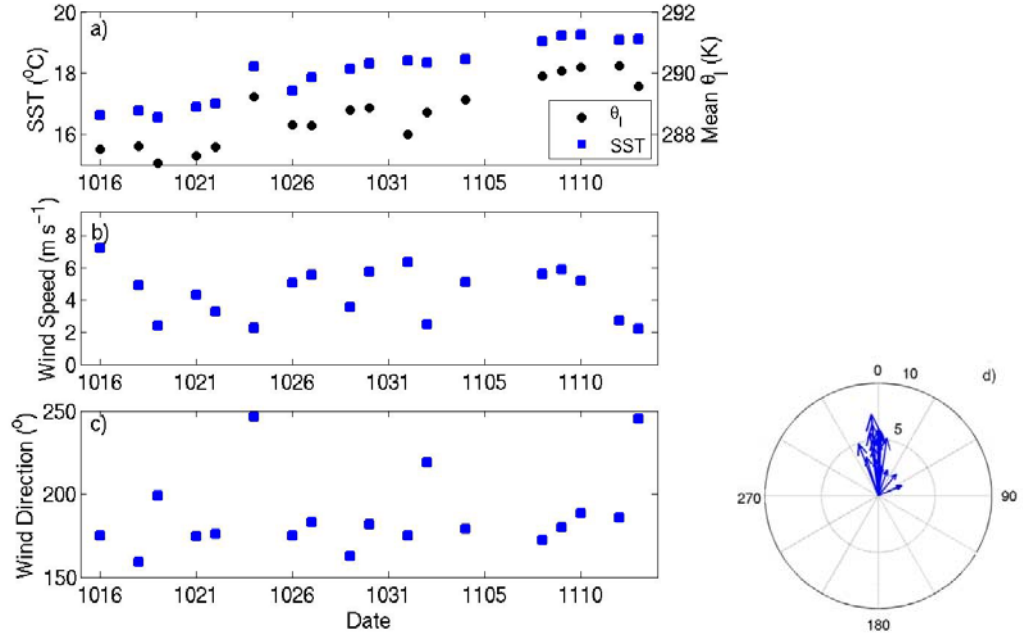


Figure 2.14 a) SST and BL-averaged θ_l , b) 30-m wind speed, c) 30-m wind direction, and d) surface wind vectors from flight data.

SST (Fig. 2.14a) increased steadily from 16.5°C on Oct. 16 to 19.5°C on Nov. 13 and the whole BL average θ_i increased in unison with the SST. The 3-day mean SST from the Tropical Rainfall Measuring Mission (TRMM) Microwave Imager (TMI) distributions on Oct. 16 and Nov. 13 (Fig. 2.15) revealed the trend of warming over the coastal region as well. We used monthly average TRMM TMI SST data (1998-2008) to examine the climatology of SST at Point Alpha. The seasonal cycle of the monthly SST increases from October to March. The climatological SST increase was about $1.1 \pm 0.4^{\circ}\text{C}$ from October to December at Point Alpha, which is less than the SST increase observed during the observational period. The relatively strong SST increase observed at Point Alpha during VOCALS-REx might be due to an inter-seasonal variation of SST over this region related to oceanic circulations. In terms of shorter temporal variability, the SST and BL-averaged θ_i on Oct. 24 were 1.5°C warmer than the two days before and 1°C warmer than the two days after it, probably because of some small-scale oceanic variations passing by Point Alpha. Based on the soundings, LWP, and satellite images, the cloud cover on Oct. 24 was very thin and broken.

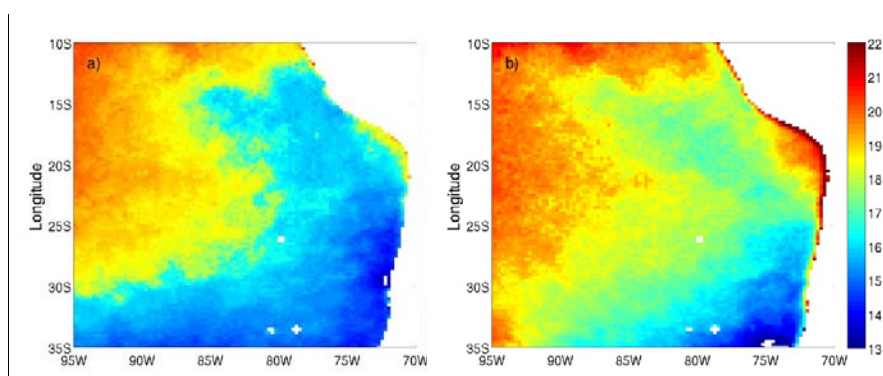


Figure 2.15 3-day mean TRMM TMI SST map ending on a) Oct. 16, 2008; b) Nov. 13, 2008

The wind speed and wind direction obtained from the 30-m level horizontal flight legs are shown in Fig. 2.14b-d. Consistent with the back trajectories and synoptic patterns discussed above, the surface wind was mainly southerly with a speed of 4 m s^{-1} on most of the flight days, except on Oct. 27, Nov. 2, and Nov. 13, when it was southeasterly with a speed of roughly 2 m s^{-1} . The average surface wind speed from QuikSCAT at Point Alpha was $4.1 \pm 1.5 \text{ m s}^{-1}$ and the wind direction was around 175° , which is consistent with the *in-situ* observations.

On each flight day, the aircraft collected one or two 10-minute legs at a height of 30 m. We used the turbulence and thermodynamic data to estimate the latent heat flux F_L , the sensible heat flux F_θ , and the buoyancy flux $F_{\theta v}$ (Table 2.3) directly from Eqs. 2.3 – 4 and Eq. 2.8:

$$F_{\theta v} = C_p \bar{\rho} \overline{w'\theta_v'} \quad (2.8)$$

where $\overline{w'q'}$, $\overline{w'\theta'}$, and $\overline{w'\theta_v'}$ are the 30-m level kinematic fluxes of moisture, heat and buoyancy, respectively. The average F_L was $48.5 \pm 15.5 \text{ W m}^{-2}$, and the average F_θ and $F_{\theta v}$ over the study period was $7.1 \pm 2.5 \text{ W m}^{-2}$ and $9.7 \pm 2.7 \text{ W m}^{-2}$, respectively.

2.5.4 Entrainment rates

The total water flux $\overline{w'q'_t}$ from the 10-minute legs near cloud top was used to calculate the entrainment rate (ω_e) in this study. If the entrainment zone is thin enough, ω_e can be estimated as:

$$\omega_e = -\frac{\overline{w'q'_t}}{\Delta q_t} \quad (2.9)$$

We extrapolate $\overline{w'q'_t}$ to the inversion according to the observational study of Gerber et al. (2005). The resulting uncertainty of the calculation can be

about 50%. The jump Δq_t was positive and $\overline{w'q'_t}$ was positive on Nov. 1-2; therefore these two days were excluded from our calculation. The extrapolation method was failed on Oct. 30 and Nov. 8 because there were not enough flight legs near the cloud top on these two days. The maximum ω_e is 3.7 mm s^{-1} and the minimum ω_e is 0.5 mm s^{-1} on Nov. 13 and Nov. 4, respectively. On the days with a large entrainment zone (Oct. 24, Oct. 27, Nov. 4), the entrainment rates were not significantly larger than the average value. However, the LWC profiles show that drier and thinner cloud layers were observed on these days. The average ω_e of $2.0 \pm 1.4 \text{ mm s}^{-1}$ (Table 2.3) tends to be lower than that obtained using reanalysis and satellite observations (Wood and Bretherton 2004). The relatively low ω_e values are consistent with the relatively weak TKE observed at Point Alpha (Fig. 2.10).

Possible explanations for the relatively low ω_e values in this study could be: 1) the observations during DYCOMS-II were during nighttime, when the BL was deepening and thus the entrainment rate tended to be large (Stevens et al. 2003). 2) ω_e in Wood and Bretherton (2004)'s study was derived from the balance between the horizontal advection of z_i and large scale subsidence. The large scale subsidence (D) at z_i can be loosely defined by divergence and inversion height: $w_s(z_i) = -Dz_i$. If we adopt the same calculation as Wood and Bretherton (2004) with the average divergence from QuikSCAT during the study period (Fig. 2.4), the average subsidence was about 3 mm s^{-1} , which is greater than the average ω_e in this study. The downstream deepening of z_i from the horizontal advection of z_i (Wood and Bretherton 2004) could balance out the

difference between the entrainment rate and the subsidence. It is unlikely to quantify the horizontal advection of z_i , however, due to the large uncertainty in the estimate of z_i . Nonetheless, the lower entrainment rate calculated from the near cloud top fluxes compared with the BL at the remote ocean west of Point Alpha and the coastal BL in the NE Pacific is consistent with the weaker turbulence in the BL discussed above.

2.6 Aerosol and cloud properties

For each flight, the average cloud droplet concentration N_d was calculated from the in-cloud legs where the cloud LWC was larger than 0.05 g m^{-3} and N_d exceeded 15 cm^{-3} . We averaged the PCASP aerosol concentrations N_a during the legs above the inversion level to get the average N_a above the inversion, and averaged N_a during the legs below the cloud base where LWC was less than 0.05 g m^{-3} to get the mean N_a in the subcloud layer (Fig. 2.16). During the study period, the CCN Spectrometer constantly measured CCN at a supersaturation of 0.2% (denoted as 0.2% CCN) except on the first four flights, during which the CCN Spectrometer constantly measured CCN at a supersaturation of 0.5% (denoted as 0.5% CCN). To estimate the temporal variation of CCN at the same supersaturation level, we adjusted the observed 0.5% CCN to 0.2% CCN on the first four flights. On the first four flights, the CCN Spectrometer also measured 0.2% CCN on another channel for several short time intervals. We averaged the concentration difference between 0.2% CCN and 0.5% CCN when both channels were on. Although the aerosol properties revealed significant variability from day to day over the coastal region during VOCALS-REx (Allen et al. 2011), the same

study also showed that the diurnal variability of aerosol composition can be neglected. We then assume that the aerosol chemical composition and size distribution did not vary significantly within each flight mission which lasted about four hours, and estimated the average 0.2% CCN from the 0.5 % values on days when the 0.2 % values were not available continuously. The average 0.5% CCN values for the first four days were also indicated in the related figures. The highest in-cloud drizzle rates were observed on Nov. 1 and Nov. 2, when the mean in-cloud drizzle water contents observed by the CIP probe were 0.0490 g m^{-3} and 0.0075 g m^{-3} respectively. The cloud LWP was highest on these two days as well (Fig. 2.12). On these two days, the peak observed in-cloud drizzle volume was 0.99 g m^{-3} and 0.22 g m^{-3} respectively. Very little drizzle was observed on the subcloud flight legs flown 100 m below the cloud base where small drizzle droplets might evaporate before reaching this level. The clouds at Point Alpha were non-drizzling or had very little drizzle compared with clouds over the open ocean during VOCALS-REx (Bretherton et al. 2010).

2.6.1 Aerosol and cloud droplet number concentrations

The average N_a above the inversion ranged between 50 cm^{-3} and 250 cm^{-3} and was lower than the average N_a below the cloud base on all flight days (Fig. 2.16). The above-inversion N_a was lower than N_d on most days except Nov. 1, during which the above-inversion N_a was close to the subcloud N_a and higher than N_d . The vertical N_a profiles on 18 flights (Fig. 2.7f) also indicate diverse concentrations within and above the BL. On most flight days, the above-inversion N_a was lower than 150 cm^{-3} , except for three soundings that captured high

aerosol concentration plumes (Oct. 24, Nov. 1, and Nov. 13). On those three days with high aerosol concentration plume above inversion, the above-inversion humidity was higher than the other days as well. The PCASP aerosol concentrations, typically comprising 80% of the total aerosol and those indicate the amount of aged aerosols (Pruppacher and Klett 1997). Although on most days an above-inversion relative humidity, which is much lower than that in the BL may cause the PCASP aerosol concentration to be poorly resolved due to a smaller dry size there, the above-inversion 0.2% CCN shows the similar pattern as the PCASP values (Fig. 2.16). The low above-inversion N_a compared with the BL N_a implies that during VOCALS-REx, the main aerosol source at Point Alpha was horizontal advection within the BL from the south, part of which might be entrained from above over further downwind days ago, rather than be entrained aerosol from above the inversion.

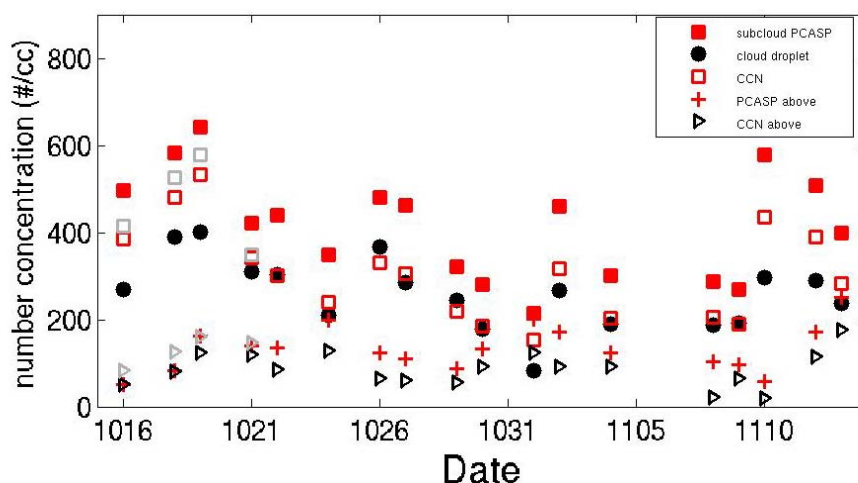


Figure 2.16 Average subcloud aerosol (red solid square), above-cloud aerosol (red cross), subcloud 0.2% CCN (open red square), above-cloud 0.2 % CCN (black triangle), and cloud droplet (black dot) number concentrations on all flight days. The average 0.5% CCN values for the first four flight days are marked as gray symbols.

The time series of the subcloud N_a , 0.2% CCN and N_d show large variations at Point Alpha during VOCALS-REx. The lowest N_a (250 cm^{-3}) occurred on Nov. 1, while the highest was close to 700 cm^{-3} on Oct. 19, which was nearly 2.5 times as large as the lowest value. The subcloud N_a were closely correlated to the temporal variation of N_d (Fig. 2.16) consistent with a strong coupling between the cloud and the subcloud layers in these nearly well-mixed conditions. The average N_d ranged between 80 and 400 cm^{-3} , with a minimum of 84 cm^{-3} on Nov. 1. The subcloud 0.2% CCN was almost equal to N_d on most of the flights. Based on a robust regression analysis, the relationship between N_d and 0.2% CCN from 18 flights is $N_d = 4.6 \times \text{CCN}^{0.71}$. Therefore, the power of 0.2% CCN in the formula from 18 cases is close to the commonly assumed value of 0.7 (e.g., Feingold et al. 2001). Previous climatological studies (George and Wood 2010; Painemal and Zuidema 2010) of satellite-derived N_d indicated that the October N_d at Point Alpha was greater than 160 cm^{-3} and the difference between the maximum and the minimum N_d exceeded 150 cm^{-3} .

We estimated the average R_e near cloud top using the same flight legs used to calculate entrainment rate. The average R_e near cloud top varied between 5.5 and $8.5 \text{ }\mu\text{m}$ yielding a mean value of $6.2 \text{ }\mu\text{m}$ for all 18 flights. The R_e values from the PVM-100 probe are estimated to be within about 15% of the actual value in the sample flow. The comparison of the *in-situ* R_e near cloud top and the GOES-10 and Terra R_e (Fig. 2.17) indicates that the satellite derived R_e is systematically larger than the *in-situ* observations. Moreover, the Terra values are all smaller than those from GOES. If the four days having cirrus

contamination (see below) are excluded, the mean R_e values from GOES and MODIS, respectively, are 2.4 ± 1.6 and 1.1 ± 1.2 μm larger than their *in-situ* counterparts. The corresponding values of R^2 are 0.91 and 0.82 for the satellite-*in-situ* matches. The matched GOES-derived LWP for these same 14 days exceeds the *in-situ* values, on average, by only 3.4 ± 19.9 g m^{-2} , a difference of only 6%. This indicates that the larger values of R_e on the cirrus-contaminated days contributed to the ~ 7 g m^{-2} bias in the GOES LWP noted earlier.

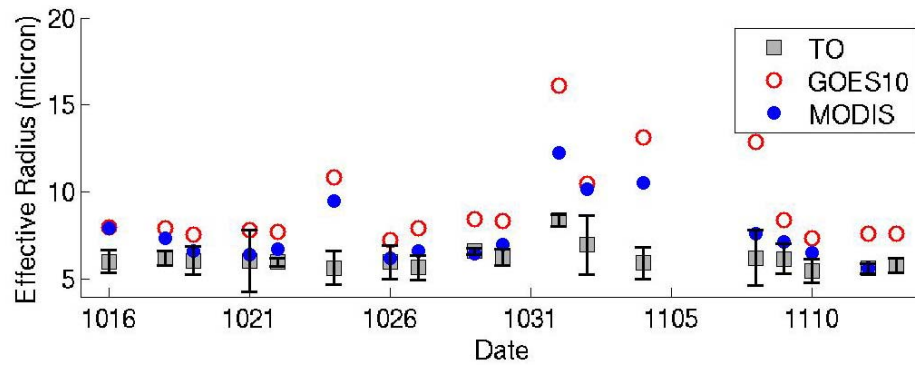


Figure 2.17 R_e from the near-cloud-top legs on all flight days. The standard deviations are indicated as the error bars. Red symbols are GOES retrievals averaged over an area within a radius of 20 km of aircraft observations. Blue symbols are average Terra MODIS retrievals for a 0.5° region centered on Point Alpha taken at between 14:20 and 15:50 UTC.

The bias between the satellite retrievals and aircraft measurements may result since for the non-drizzling Sc cloud the cloud droplet size increases with height and the aircraft measurements were made about 50 m lower than the cloud top. However, the average from the vertical profiles was very close to the cloud-top values. The largest differences occurred on October 24 and 27 and on November 1, 2, 4, and 8. The GOES retrievals were contaminated by overlying cirrus clouds on these days except for November 1 and 2. The cirrus clouds lead to an overestimate of R_e . (e.g., Dong et al. 2002). Drizzle droplets on November

1 and 2 are the most likely explanation for the large discrepancies in R_e during those days. For drizzling conditions, in which the vertical structure of LWC can be quite different from the adiabatic case, R_e can increase downward below cloud top because the larger droplets settle out and leave a greater concentration of smaller droplets in the upper portion of the cloud. The R_e retrieved using a 3.9- μm radiance corresponds to an optical depth of 5 or more for $R_e = 12\ \mu\text{m}$ and 8 or more for $R_e = 8\ \mu\text{m}$, so it actually corresponds to a significant portion of the mass in the cloud and may not exactly correspond to 50 m below cloud top. As shown by Dong et al. (2002), R_e and LWC profiles are often non-adiabatic near the cloud top in stratus clouds so differences between R_e in the top 50 m and integrated over some depth in the cloud are not surprising. Furthermore, the droplets may be smaller at that level in the cloud because of entrainment of the overlying air.

The R_e differences between Terra and GOES-10 are mostly due to the time differences, noted earlier, that affect the LWP comparisons (e.g., Fig. 2.12). The mean GOES R_e at 12:45 UTC (08:45 LT) is 9.2 μm compared to 7.7 μm at 15:30 UTC (11:30 LT) near the Terra overpass. Although the GOES results at the Terra overpass time essentially agree with the MODIS retrievals, there may also be some systematic algorithmic differences and spatial resolution effects that could contribute to those differences.

Despite the bias in the GOES retrievals of R_e relative the *in-situ* measurements, the good correlation in R_e and agreement in LWP indicate that the satellite retrievals are providing a realistic representation of the variation in

LWP and R_e , at least, for unbroken adiabatic clouds. Since LWP is computed from the product of R_e and optical depth from the satellite data, an overestimate of R_e would imply an underestimate of cloud optical depth. Such an underestimate may be due to calibration biases or to biases in the retrieval algorithms. Either error source will require additional study.

2.6.2 Cloud LWP and subcloud CCN concentrations

Since all 18 flight cases at Point Alpha were with little or -non-drizzling marine Sc, the temporal variations of cloud LWP and aerosol concentrations at Point Alpha offered us an opportunity to study aerosol-cloud interactions in non-drizzling Sc at a fixed location. The cloud LWP as a function of subcloud 0.2% CCN concentration for all flight cases is shown in Fig. 2.18. The synoptic variations, diurnal cycle of the BL, and the other BL processes have to be taken into account when the cloud LWP-aerosol relationship is tested, as they can affect the cloud LWP (e.g., Albrecht et al. 1995a; Stevens and Feingold 2009; etc.). Ten of those flights were made under similar meteorological conditions (Bold marked in Table 2.1 and highlighted in Fig. 2.18). The BL on those flight days were typically well-mixed, with solid non-drizzling Sc. The remaining eight flights involved complications as discussed in previous sections such as a moist layer above (Nov. 1-2, Nov. 13), strong wind shear within the BL (Oct. 24, Oct. 30, Nov. 4), strong decoupled BL with cumulus below the Sc layer (Oct. 29, Nov. 4, Nov. 8). The four flights marked on Fig. 2.18 from Oct. 29 to Nov. 2 demonstrated an enhanced cloud LWP compared with the other days. One of the possible explanations could be the impact of a synoptic system related with the

moist layer passing over this area. A positive relationship between the cloud LWP and aerosol in the typical well-mixed BL is observed in Fig. 2.18. However, this also shows that the meteorological factors and the BL processes that keep BL from being well-mixed can have large influences on the cloud LWP variation.

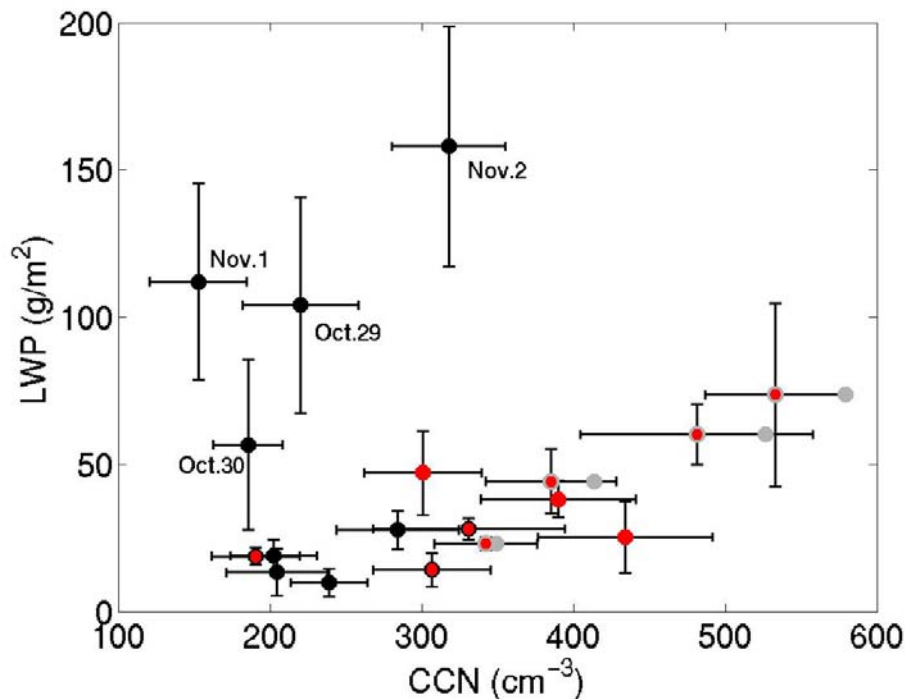


Figure 2.18. LWP as a function of subcloud CCN concentrations for all flight days. The horizontal error bars through these symbols indicate the standard deviation of CCN. The uncertainty of the LWP denoted as the vertical bars. Red solid symbols are the typical well mixed boundary with non-drizzling Sc discussed in Zheng et al., 2010. The average 0.5% CCN values for the first four flight days are indicated as the gray dots, and the corresponded 0.2% CCN values are marked as the red dots with gray edges.

2.7 Summary

The Twin Otter aircraft performed 18 flights at Point Alpha during VOCALS-REx from Oct. 16 to Nov. 13 2008. These observations provided a unique dataset for defining the characteristics of the near-coastal marine Sc and

the BL off the coast of Northern Chile. This study used these *in-situ* observations and meteorological reanalysis, radiosonde and satellite-derived data to study the BL, clouds, and aerosol variations at Point Alpha.

The results show that the BL at Point Alpha during VOCALS-REx was usually characterized by a typical Sc-topped BL except when some synoptic systems and meso-scale processes affected this region. The BL depth was about 1140 ± 120 m and the BL was well-mixed and capped by a very sharp inversion. The wind direction switched from southerly within the BL to northerly above the inversion. The surface wind speed was lower than that over the remote ocean west of Point Alpha due to the topography. On some flight days, wind shear appeared within the BL. The wind profile from the soundings are consistent with the average wind field from the horizontal flight legs, therefore, the observed vertical wind shear within the BL stayed constant throughout the flight mission. This phenomenon is rare and possibly due to the complex coastal processes. Compared with the BL depth west of Point Alpha over the remote ocean, the BL at Point Alpha was about 200-400 m shallower and more well-mixed (Bretherton et al. 2010). The BL depth was about 300 m higher than that over the coastal region in the NE Pacific (Stevens et al. 2003; Sharon et al. 2006). The surface wind and the surface fluxes at Point Alpha were weaker than those over the remote ocean and also weaker than the observations in the NE Pacific during DYCOMS-II. Turbulence in the near-coastal BL appeared to be weaker than that in the BL over the open ocean and the BL over the coastal region in the NE Pacific in terms of vertical velocity variance. The weaker turbulence in the BL at

Point Alpha might contribute to the lower entrainment rate calculated from the near cloud top fluxes compared with the BL at the remote ocean west of Point Alpha and the coastal BL in the NE Pacific (Bretherton et al. 2010; Stevens et al. 2003; Stevens et al. 2005).

Throughout the study period, the BL evolved gradually with variations influenced by synoptic systems. From the end of October to the beginning of November, the cloud LWP was higher than the other days by around 40 g m^{-2} (Fig. 2.12). This is most likely due to an intense mid-latitude disturbance controlling the coastal area (Rahn and Garreaud 2010b; Toniazzo et al. 2011). On Nov. 1 and Nov. 2, a moist layer above the inversion moved over Point Alpha. The cloud LWP reached a maximum on these two days. The total-water specific humidity above the inversion was larger than that within the BL. The inversion strength became significantly weaker on these two days and the BL was decoupled due to drizzle.

The accumulation mode aerosol and 0.2% CCN measurements indicated N_a within the BL at Point Alpha varied between 250 and 700 cm^{-3} during VOCALS-REx. The main aerosol source at Point Alpha was the horizontal advection within the BL from south of Point Alpha. The average N_d ranged between 80 and 400 cm^{-3} . This range was consistent with the satellite-derived N_d . However, the GOES-derived cloud droplet R_e tended to be larger than that observed near cloud top, although the GOES-derived LWP was essentially the same as that determined from the aircraft vertical profiles of LWC. The aerosol and cloud LWP relationship reveals that during the typical well-mixed BL days

the cloud LWP was positively correlated with the 0.2% CCN concentrations. At the same time, meteorological factors and the decoupling processes have large influences on the cloud LWP variation as well. The aircraft flights lasted no more than five hours on each flight days and the time gap between two flights was generally longer than 24 hours. Thus, it was not possible to capture the continuous evolution of the cloud layer and the processes affecting the boundary layer structure and clouds at the time scales from hours to days, which could also be critical for the cloud LWP variation. (e.g. Albrecht et al., 1995b; Sandu et al., 2008). Additionally, only 18 flights were completed, which is insufficient for finding a statistically significant correlation. The observations available are inadequate to full study the causes of the observed perturbation from the mixed layer state. Further modeling and diagnostic studies are required to fully explain the cloud LWP variation and its relationship with the aerosol variations at Point Alpha during VOCALS-REx.

In summary, the BL at Point Alpha exhibited the typical well-mixed BL topped by a thin and non-drizzling Sc layer on days without the dominant influence of the synoptic system and the coastal processes, which could be an ideal environment to study the aerosol-cloud interaction. The variability we observed allowed us to document the complex processes in the near-coastal region on some flight days. This dataset will be used for the further study of aerosol-cloud interactions and the evaluation of models operating at a variety of scales to study near-coastal marine stratocumulus during VOCALS-REx.

Chapter 3: Liquid water path and cloud condensation nuclei relationships in marine stratocumulus

3.1 Motivation and objectives

Anthropogenic aerosol particles are considered to modify marine stratocumulus cloud properties by changing the cloud droplet size distribution (Twomey 1977) that will increase cloud albedo for a fixed liquid water path and by suppressing drizzle processes that may increase cloud liquid water path and increase cloud amount and life time (Albrecht 1989). These two effects are called the first and the second aerosol indirect effect. Although the first indirect effect has been established (e.g., Lu and Seinfeld 2005; Coakley and Walsh 2002; et al.), the second indirect effect has controversial aspects and caveats that are revealed by numerical simulations (e.g., Lu and Seinfeld 2005) and satellite based observations (Coakley and Walsh 2002).

Large-eddy simulations indicate that the introduction of aerosols can reduce cloud droplet size and inhibit cloud droplet sedimentation, which is important for turbulence maintenance (Ackerman 2004; Bretherton 2007). Thus in this case the enhanced evaporation and entrainment at the cloud top reduces liquid water path. Wood (2007) used a mixed layer model to show that entrainment in polluted clouds with high cloud bases was enhanced and this process resulted in a thinning of the cloud and that was more important than drizzle reductions in liquid water path during the first 24 hours of simulation. For longer simulations, however, the precipitation effects on liquid water path were dominant. In Wood's hypothesis, the enhanced entrainment is due to increased turbulence in polluted clouds, which is opposite to the Ackerman (2004) and

Bretherton (2007)'s results. Satellite based observations (Christensen et al. 2009) indicate that the cloud water amounts of both polluted and unpolluted marine stratus decrease from morning to afternoon, however, the rate at which the cloud water amount of polluted marine stratus falls is clearly slower than that for the unpolluted cases.

There are two main challenges for observations (Stevens and Feingold 2009). First, satellite observations of aerosols are limited in cloudy regions. Further, in some cases it is difficult to use satellite observations to distinguish between cloud droplets and aerosols (Koren et al. 2007). Second, for both satellite and *in-situ* measurements, meteorological factors also control the change of cloud water content (e.g., Klein and Hartmann 1993; Stevens and Brenguier 2008; Klein 1997; George and Wood 2010; Painemal and Zuidema 2010; etc.). Thus these effects must be minimized or removed to study the response of the clouds to aerosol perturbations. The scientific objective of this study is using the same *in-situ* aircraft and satellite observations described in chapter 2 to investigate the second aerosol indirect effect in marine stratocumulus clouds under relatively constant meteorological conditions.

3.2 Data and methods

In-situ aircraft observations for this study were from the Twin Otter project during the VOCALS-REx from Oct.16 to Nov.13 2008. Instruments on the aircraft measured standard meteorological variables, turbulence, aerosol, cloud, and precipitation (Table 2.2), which have been fully described in chapter 2.2.

According to the results in Chapter 2.5, the cloud and boundary layer structures observed on 8 of the 18 flights included complications involving strong wind shear within the BL, moist layers above the inversion, and strong decoupled BL with cumulus below Sc. In this study, 10 remaining cases (bold marked in Table 2.1) in which inversion heights varied between 1000 and 1300 m, potential temperature increased across the capping inversion in a range of 12-17°C, and total water mixing ratio decreased across the inversion in a range of 5.5 to 8 g kg⁻¹. The drizzle water contents from the Cloud Imaging Probe (CIP) on the 10 days were less than 10⁻³ g m⁻³. Based on this analysis, the clouds occurring during these selected 10 days are assumed to exist in relatively similar meteorological conditions, although the sea-surface temperature (SST) at Alpha increased from 16.5-19.3°C during the course of the study. Therefore, the influences of meteorological factors (including coastal effects) are assumed to be minimal. The majority (7) of the ten flights were made around 0900 Local Time (LT) (1300 UTC), while the others were conducted from around 1200 to 1300 LT.

The thermodynamic structures for these flights are shown in Fig. 3.1 using a height scale normalized by the inversion height. These structures show well-mixed BL capped by sharp inversions and similar BL thermodynamics for all the cases selected. The cloud thicknesses and liquid water contents, however, for these cases vary substantially among the 10 cases.

PCASP measured particles between a size range of 0.1 and 2 micron diameter, which was divided into 20 bins. CAPS counts and sizes cloud droplet particles into 20 size bins ranging between 2.07 and 40.2 micron diameter. The

particle size range of CIP is between 15.5 and 1500 micron diameter and it has been divided into 62 size bins. Uncertainties for aerosols and cloud droplet concentrations (N_d) measured by these probes are estimated to be generally within 15% in the sample flow.

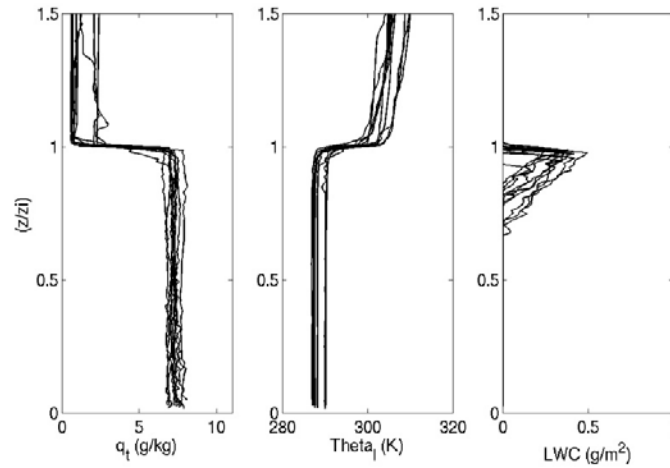


Figure 3.1 Vertical profiles of total water mixing ratio, liquid water potential temperature, and liquid water content for the ten cases in the study (Oct. 16, Oct. 18, Oct.19, Oct. 21, Oct. 22, Oct. 26, Oct. 27, Nov. 9, Nov. 10, Nov. 12, 2008).

For each flight day, all CCN measurements (at a super-saturation of 0.2%) below cloud base are averaged to give mean CCN concentrations (See Chapter 2.6 for further details and discussions). The sub-cloud and above-inversion PCASP accumulation mode aerosol concentrations (PCASP concentrations hereafter) in the sub-cloud layer and N_d in the cloud layer are calculated in a similar way.

Instead of integrating the 12:00 UTC sounding of liquid water content (LWC) from the Gerber probe to estimate LWP (Zheng et al. 2010), this study calculated the average LWP from two available soundings on each day. The LWC from the soundings and the horizontal leg averages at different levels have

mean difference for all flights of $0.03 \pm 0.04 \text{ g m}^{-3}$, indicating that the LWC from soundings are representative of the larger-scale cloud area.

To further analyze the history of the air masses sampled by the aircraft, we use the Hybrid Single Particle Lagrangian Integrated Trajectory Model (HYSPLIT) model (Draxler and Rolph 2003) driven with the NCEP Global Data Assimilation System (GDAS) data to calculate the two-dimensional backward trajectories starting at the 500-m level from Point Alpha for 36 hours. In addition, radiances from the Tenth Geostationary Operational Environmental Satellite (GOES-10) were used to retrieve cloud properties using the methods of Minnis et al. (2011a,b) for areas in the vicinity of the aircraft measurements and at times prior to and after the measurements.

Statistical analyses based on decades of cloud field observations and numerical studies have been shown that the horizontal mean precipitation rate of marine stratocumulus clouds primarily depends on the cloud geometrical thickness/LWP and N_d (e.g., Pawlowska and Brenguier 2003; Wood 2005; Geoffroy et al. 2008; et al.). Although different relationships have been established from different field experiments and numerical studies (e.g., Table 3.1), the precipitation rate in marine Sc scales with the cloud geometrical thickness/LWP and N_d as the following uniform formula:

$$R = C_1 \frac{LWP^\alpha}{N_d^\beta} + C_2 \quad (3.1)$$

where R is the rain/drizzle rate ($\text{g m}^{-2} \text{ hour}^{-1}$), and C_1 , C_2 , α , β are parameters obtained from the best fit derived from previous observational data. β

is also named precipitation susceptibility (Stevens and Feingold 2009). The higher the β is, the more sensitive the rain rate is to changes in N_d .

By assuming that N_d stayed constant during the study period (12 hours), the possible range of the earlier drizzle rates in the observed clouds before flight observations can be calculated with the GOES-10 derived LWP and the observed N_d (Eq. 3.1). The possible changes in drizzle rates modulated by N_d are also estimated with the following empirical formulas via varying N_d within the observed range.

Table 3.1 Summary of drizzle rate as the functions of LWP/cloud depth and cloud droplet concentration observations (Table 1, Geoffroy et al. 2008).

	$N \text{ (cm}^{-3}\text{)}$	$H \text{ (m)}$	LWP ($10^{-3} \text{ kg m}^{-2}$)	R ($10^{-6} \text{ kg m}^{-2} \text{ s}^{-1}$)	Formulation
ACE-2	N_{act} [51 256]	H_g [167 272]	$\frac{1}{2}C_w H_g^2$ [27 74]	$\langle R \rangle$ [0.6 18.6]	$R = 0.3 \cdot 10^6 \cdot \frac{LWP^2}{N} - 10^{-6}$
EPIC	$\langle N \rangle$ [61 190]	- -	$\langle LWP \rangle$ [47 275]	$\langle R_{\text{base}} \rangle$ [0.02 24.5]	$R = 24.37 \cdot 10^9 \cdot \left(\frac{LWP^2}{N}\right)^{1.75}$
DYCOM S-II	$\langle N \rangle$ [58 254]	$\langle H \rangle$ [265 515]	$\frac{1}{2}C_w \langle H \rangle^2$ [70 265]	$\langle R_{\text{base}} \rangle$ [0.5 19.1]	$R = 21.5 \cdot 10^3 \cdot \frac{LWP^{1.5}}{N} - 2.3 \cdot 10^{-6}$

3.3 Results

The CCN concentrations in the sub-cloud layer varied from 190 to 565 cm^{-3} among the 10 flights and were positively correlated with N_d , which ranged from 188 to 392 cm^{-3} . The LWPs in these relatively thin clouds ranged from 14 to 74 g m^{-2} and are positively correlated with the aerosol and N_d (Fig. 3.2). The cloud LWP estimated from the GOES analyses are also shown in this figure. The

average difference between the aircraft and satellite (20 km) LWP is $-5.2 \pm 11 \text{ g m}^{-2}$. These results further support the idea that the sounding estimates of the LWP are representative of a larger area as viewed by the satellite.

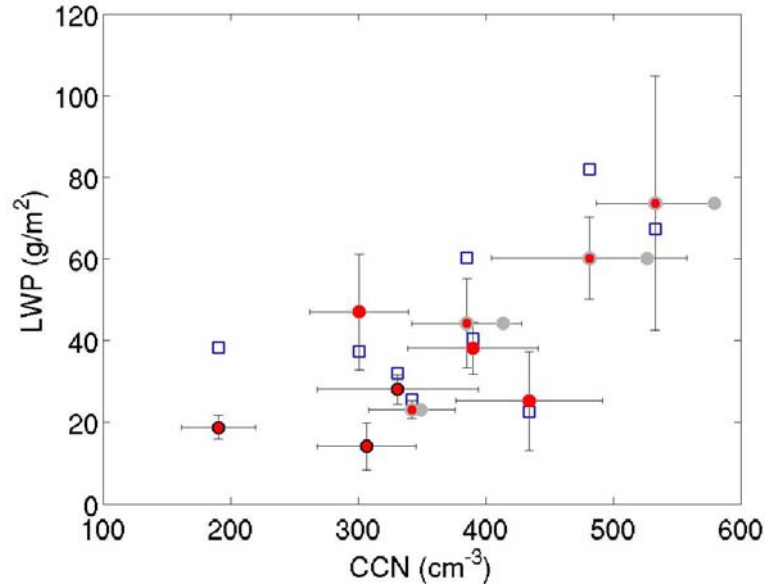


Figure 3.2 LWP as a function of sub-cloud CCN concentrations for selected 10 flights. The horizontal error bars through these symbols indicate the standard deviation of CCN. The uncertainty of the LWP denoted as the vertical bars. The average 0.5% CCN values for the first four flight days are indicated as the gray dots, and the corresponded 0.2% CCN values are marked as the red dots with gray edges. Open blue squares are GOES retrievals averaged for each entire flight mission over an area within a radius of 20 km of Point Alpha.

The positive correlation between the CCN concentrations and N_d are shown in Fig. 3.3 where the probe concentrations are sorted from lowest to highest CCN concentrations. The correlation between the CCN (and PCASP), and N_d is evident, although the deviation between the CCN and N_d increases with increasing CCN (and PCASP) concentrations. The PCASP concentrations above the inversion are lowest when the N_d are high and indicate no major influence of the above-inversion aerosols on the BL aerosol conditions.

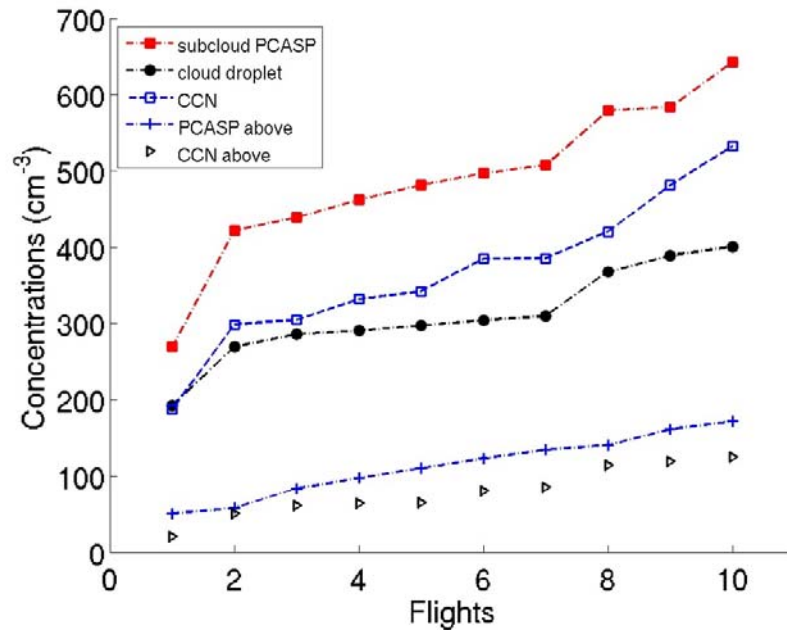


Figure 3.3 Sub-cloud layer CCN, PCASP and N_d for 10 cases sorted by increasing CCN from flight 1 to 10. Above-inversion PCASPs and CCN are also shown for comparison.

Two-dimensional backward trajectories starting at the 500-m level on the 10 flight days (Fig. 2.5) indicate a flow from the southeast of Point Alpha from points close to the coast of Chile 36 hours earlier. During the 36 hour periods, 6 of the air masses moved less than 700 km and remained over water, while the air masses for the other 2 cases (Oct 16 and 18) moved more than 1000 km from the south. The SST isotherms in this area are oriented southeast to northwest, and since the synoptic patterns for the cases are similar, advective effects did not vary substantially from case to case as indicated by the similar trajectories on all but one case. Although there are uncertainties in these back trajectories due to errors in the GDAS, the errors should be smallest in the early history of the trajectories.

To further investigate BL, aerosol, and cloud characteristics for the cases with high and low CCN concentrations, we averaged two cases (October 18 and 19) with the highest CCN (HC) and the three cases (October 22, October 27, and November 9) with the lowest CCN (LC) because CCN concentrations on October 22 (the second lowest CCN concentration day) and November 9 (the third lowest CCN concentration day) are close to each other (Fig. 3.3). Characteristics of the BL, clouds, and aerosols for the HC and LC cases are given in Table 2 along with the averaged features for the highest 5 cases and the lowest 5 cases. The HC PCASP concentration is about double that for the LC cases, which is consistent with the CCN values. The higher CCN concentrations for the HC cases are associated with N_d of 395 cm^{-3} , which are 153 cm^{-3} higher than that in the LC case. Both the mean *in-situ* LWP and the mean GOES LWP within a 20-km radius circle around Point Alpha are higher for the HC (65 g m^{-2} and 75 g m^{-2}) cases compared to those for the LC (18 g m^{-2} , 37 g m^{-2} and 36 g m^{-2}) cases. The LWP difference between HC and LC is larger than the data uncertainty. The SST in the HC cases is 1.5°C lower than that for LC. The lower SSTs and surface wind speeds for the HC case are also associated with a surface virtual temperature flux ($F\theta_v$) that is 2.5 W m^{-2} lower, and a water vapor flux (Fq_v) that is 10.2 W m^{-2} lower as well. Mixed layer theory (Schubert et al. 1979) would indicate that an increase in either SST or surface wind speed would increase the cloud depth (and LWP), which is counter to the observations. The potential temperature jumps across the inversion are 15.8 K and 13.8 K for the HC and LC, respectively, and the corresponding total water mixing ratio jumps are 6.2

and 5.8 g/kg. The average HC cloud top is 100 m lower than its LC counterpart, while the HC cloud base is 233 m lower than that for the LC cases. The ratio of the observed LWP to the adiabatic LWP is about 0.79 compared with 0.7 for the LC data. Thus for the HC case the larger LWP is due to a cloud that is both thicker and closer to adiabatic than the LC cases. The averages for the 5 highest and the 5 lowest CCN cases also show similar, but somewhat reduced differences between the two cases.

Table 3.2 Cloud, aerosol, and BL characteristics averaged for the two cases with the highest CCN, the three cases with the lowest CCN, the five highest CCN cases, and the five lowest CCN cases.

	HIGH CCN (2 Cases)	LOW CCN (3 Cases)	HIGH CCN (5 Cases)	LOW CCN (5 Cases)
PCASP(cm^{-3})	613	384	561	415
CCN (cm^{-3})	510	263	441	293
N_d (cm^{-3})	395	260	329	286
LWP (g/m^2)	67	26	49	26
LWP _{SAT} (g/m^2)	75	37	55	33
LWP/LWP _{adia}	0.79	0.70	0.74	0.73
SST ($^{\circ}\text{C}$)	16.7	18.3	17.7	17.7
$F\theta_v$ (W/m^2)	8.8	11.3	7	8.4
Fq (W/m^2)	30.4	40.6	40.5	50.9
w variance (m^2s^{-2})	0.26	0.16	0.18	0.17
CLD TOP (m)	1050	1148	1070	1088
CLD Base (m)	750	983	850	940
$\Delta\theta$ (K)	15.8	13.8	12.3	11.1
$-\Delta(q+l)$ (g/kg)	-6.2	-5.8	-6.3	-5.7
$\Delta\theta_l$ (K)	14.2	11.5	13.1	11.7
w_e (mm/s)	1.1	1.9	1.3	1.8
30m Wind Speed (m/s)	3.7	4.9	4.5	4.8

Compared with the LC results, the HC cases have stronger and lower inversions, which are consistent with either stronger large-scale subsidence or weaker entrainment rates. Using the eddy fluxes of total water at cloud top, the estimated entrainment rates $w_e = -(\overline{w'(q' + \ell')})/(\Delta q_i)$ are 1.1 and 1.9 mm/s respectively. Although there is substantially uncertainty in these estimates of entrainment, they suggest that the entrainment rates in the HC case are lower than those in the LC case (consistent with the lower HC inversion height), although the w variance in the cloud layer (Table 2) is $0.26 \text{ m}^2\text{s}^{-2}$ for the HC case compared with $0.16 \text{ m}^2\text{s}^{-2}$ in LC case, although the 5-case averages are similar.

Although the effects of large-scale advection on the cloud evolution cannot be fully addressed due to the lack of upstream *in-situ* observations prior to the flight mission, the time tendency of the cloud base height caused by the cold and dry advections can be roughly estimated in terms of the mixed layer theory. We assume that the thermodynamic features of the BL and SST reach equilibrium status quickly (Schubert et al. 1979b). As a result, the time tendencies of the BL θ and q can be estimated by the advection of SST. In addition, the cloud base height is approximated to be the height of the lifted condensation level, which is controlled by both time tendencies of the BL θ and q :

$$\frac{\partial \theta}{\partial t} \cong -\vec{V} \cdot \nabla SST \quad (3.2)$$

$$\frac{\partial q}{\partial t} \cong -\vec{V} \cdot \nabla q_s \times RH/100 \quad (3.3)$$

$$\frac{\partial Z_{LCL}}{\partial t} \cong -\eta_1 \frac{\partial q}{\partial t} + \eta_2 \frac{\partial \theta}{\partial t} \quad (3.4)$$

where \vec{V} is wind vector, ∇SST is horizontal gradient of SST, q_s is saturated water mixing ratio, RH is relative humidity, $\eta_1 \approx 200 \text{ m kg g}^{-1}$, $\eta_2 \approx 103 \text{ m K}^{-1}$

We used three-day average SST data from the Tropical Rainfall Measuring Mission (TRMM) Microwave Imager (TMI) and *in-situ* observations at Point Alpha to estimate the time tendencies of the cloud base height on the LC and HC flight days (Table 3.3) by assuming the BL relative humidity to be 70%. The cold SST advection on the HC case was more than three times larger than that on the LC case; and the dry advection on the HC was also larger than that on the LC case. The effects of the cold advection and the dry advection tend to compensate each other. Therefore, the difference in the time tendencies of the cloud base height between the LC case and the HC case is less than 3 m day^{-1} , while the observed difference in the cloud base height between the LC case and the HC case is larger than 200 m (Table 3.2).

Table 3.3 Large-scale advection estimation for the two cases with the highest CCN and the three cases with the lowest CCN.

	HIGH CCN (2 Cases)	LOW CCN (3 Cases)
$\left(\frac{\partial \theta}{\partial t}\right)_{SST} (\text{K day}^{-1})$	-1.27	-0.39
$\left(\frac{\partial q}{\partial t}\right)_{SST} (\text{g kg}^{-1} \text{ day}^{-1})$	-0.66	-0.22
$\left(\frac{\partial Z_{LCL}}{\partial t}\right) (\text{m day}^{-1})$	1.2	3.8

The GOES-10 satellite retrievals offer us an opportunity to see the upstream large scale-cloud field prior to the flight observations. The six-hour average fields of LWP and cloud droplet effective radius (R_e) before the aircraft measurements on the HC and LC cases are shown Fig 3.4. The large-scale cloud fields on the HC days were solid and homogenous over large area with clearly higher LWP than those on the LC days (Fig 3.4e,g,i) back to 6 hours

before the observations. On the other hand, the cloud fields on the LC days revealed more spatial variation along the back trajectories. Particularly, there were small cellular like structures and rifts showing up on 27 October and 09 November on both LWP and R_e fields. The LWPs around Point Alpha were low on the LC days compared with the HC days ($\sim 70 \text{ g m}^{-2}$ vs. $\sim 140 \text{ g m}^{-2}$). Although the LWPs on the HC days are much higher, the R_e fields are comparable between the two groups might due to the aerosol indirect effects.

To explore the time history of the observed differences in the LWP for the HC and LC cases, the cloud properties along the back trajectories from the GOES satellite retrievals are also considered. Figure 3.5 shows the Lagrangian-like time evolution of LWP and R_e for the HC and LC cases from 12 hours before to 1 hour before the flights each day. The LWP from the satellite retrievals decreased sharply after sunrise in all five cases, during the night the HC cases had much larger LWP than the LC cases. After sunrise, LWP in the HC cases decreased, but remained larger than those in the LC cases. The relatively sharp drops in LWP after sunrise, especially for the greater of the HC cases are due to the change in the satellite retrieval algorithms between day and night (Minnis et al. 2011a). Nevertheless, the nighttime algorithm shows some skill in discriminating between optically thick and thin clouds and areas with small or

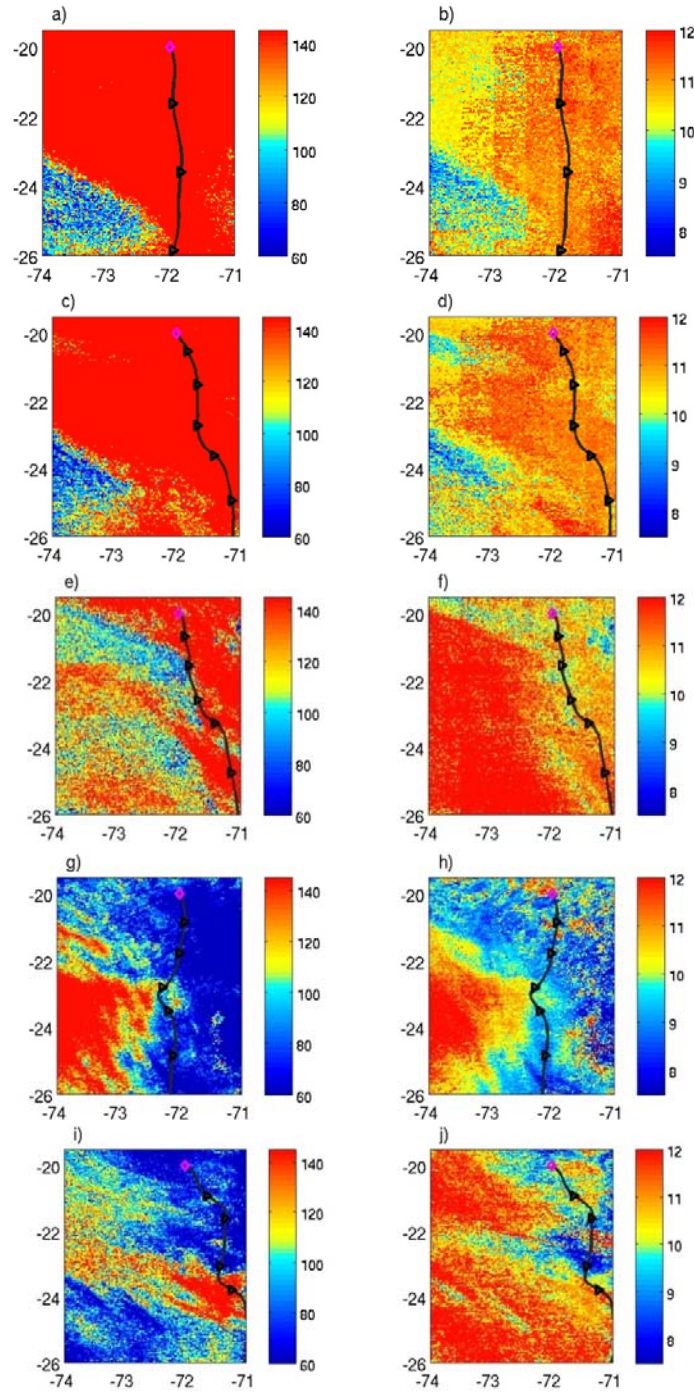


Figure 3.4 The six-hour average fields of LWP (unit: g m^{-2}) prior to the flight observation on a) 18 October (HC), c) 19 October (HC), e) 22 October (LC), g) 27 October (LC), i) 09 November (LC), and the six-hour average fields of R_e (unit: micron) prior to the flight observation on b) 18 October (HC), d) 19 October (HC), f) 22 October (LC), h) 27 October (LC), j) 09 November derived from

GOES-10 data. The back line on each panel represents six-hour marks of two-dimensional isobaric back trajectory starting at 500 from Point Alpha.

large droplets, especially for Sc (Minnis et al. 2011b). The time series of R_e for those five cases show that on the HC days, although the LWP were much higher, the high CCN concentrations reduced the cloud droplet sizes to be similar to the low CCN clouds.

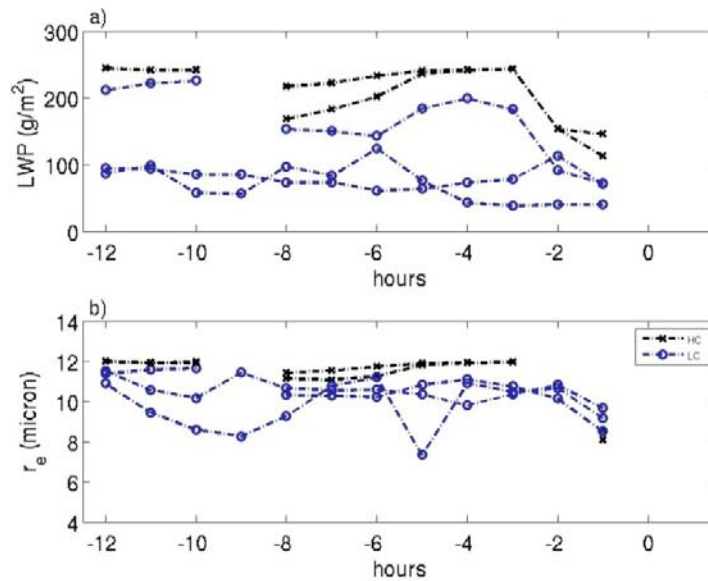


Figure 3.5 Time evolution of GOES-derived LWP and R_e for the two highest (black cross symbols) and the three lowest (blue open symbols) CCN concentrations from 12 hours prior to the flight (marked as t=-12hr) to 1 hour before flight time (t=-1hr).

The Lagrangian analysis indicates that the differences observed by the aircraft may have existed at least 12 hours prior to the observations, which implies that the LWP differences for the extreme cases mainly resulted from cloud evolution rather than differences in external meteorological influences. On the high CCN days, the reduced droplet size might suppress the drizzle production and help to maintain the high LWP (Wood 2005; Albrecht 1989). To

study the possible drizzle-suppression effect on the high CCN days, we used four different empirical relationships between drizzle rate, LWP and droplet concentration determined from previous observations to estimate the possible LWP difference between the HC cases and the LC cases due to the different N_d values. According to these empirical relationships (Eq. 3.1, Table 3.2), the drizzle rates in the HC cases were lower than the cloud with the same LWP but lower N_d (i.e. N_d in LC cases). The drizzle water reduction due to higher N_d can be calculated as following:

$$\Delta R = C_1 \left(\frac{LWP^\alpha}{N_{d1}^\beta} - \frac{LWP^\alpha}{N_{d0}^\beta} \right) \quad (3.5)$$

where ΔR is the drizzle rate reduction, C_1 , α , β are from Eq 3.1, N_{d1} is the average N_d in the LC cases, N_{d0} is the average N_d in the HC cases, LWP is the hourly LWP in the HC cases as Fig 3.5 shown.

After getting the drizzle rate reduction, we assume all of the reduced drizzle water stayed in the cloud layer and became one part of LWP within that particular hour:

$$\Delta LWP = \Delta R \times 1\text{hour} \quad (3.6)$$

We calculate ΔLWP back to 12 hours before the HC flights and get an average ΔLWP and an hourly LWP for the HC case (Fig. 3.6). The average LWP on the HC days is about 200 g m^{-2} , while the counterpart on the LC days is around 100 g m^{-2} . The equivalent LWP due to one-hour drizzle reduction on the HC days ranges from around 30 g m^{-2} to about 140 g m^{-2} , depending on how sensitive the empirical formula is to the change of aerosol concentration. In other words, without aerosol induced drizzle suppression, the LWP might have

reduced to such range by drizzling. The most aerosol-sensitive empirical relationship produced very high drizzle rate that can decrease the LWP to be similar to the clean cases within one hour. Therefore, the satellite retrievals obtained upstream prior the flight observations provide evidence that the clouds under the high CCN concentrations have minimal LWP loss due to precipitation suppression effects.

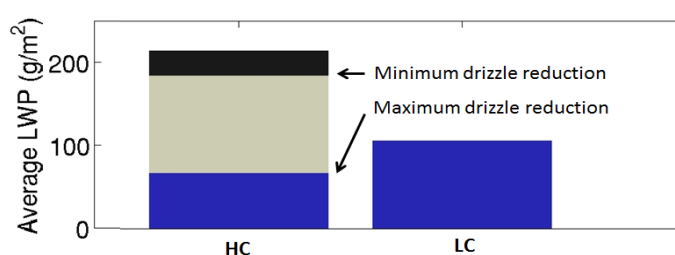


Figure 3.6 12-hour average LWP along the back trajectories prior to the flights on the HC days (left bar) and LC days (right bar) with the range of the equivalent LWP proportion (gray bar) due to one-hour drizzle reduction.

3.4 Conclusion and discussion

The boundary layer, aerosol, and cloud properties observed on ten eight research flights made off the coast of Northern Chile with the CIRPAS Twin Otters indicate a strong positive correlation between boundary layer CCN concentrations and cloud LWP associated with similar boundary layer and synoptic conditions. A detailed study of the two highest and the two lowest CCN concentration cases further confirms that the differences in the large-scale advections and the thermodynamic jumps at the top of the boundary layer and the turbulent fluxes at the surface cannot explain the observed differences in the LWP. Satellite retrievals from GOES 10 show that the LWP differences observed at the time of the aircraft flights are also prevalent during the night-time hours

prior to the aircraft observations made at approximately 0900 local time. The cases with low LWP and CCN concentrations are associated with clouds that are thinner and a water content that is a smaller fraction of the adiabatic value than the high CCN and LWP cases.

The positive correlation observed in this study is inconsistent with some of the conclusions from previous modeling studies (e.g., Ackerman 2004; Bretherton 2007; Wood 2007) and satellite analyses (e.g., Coakley et al. 2002). The disagreements among previous studies may be partly accounted for by the different statistical stratagems and methodologies. For instance, Coakley et al. (2002) compared the cloud properties for ship tracks and the surrounding environment by only taking account of the solid cloud pixels; however, broken clouds (open cells) occur frequently in the clean environment. Thus elimination of these cases may bias the statistics of the liquid water path comparisons between the ship tracks (and associated high CCN) and their environment. In our study, the ratio of LWP and adiabatic LWP is much less than unity in some clouds, which implies that processes such as entrainment and drizzle could be forcing cloud liquid water contents to deviate from the adiabatic values. Consequently, in these cases the boundary layer may not be strictly well-mixed. The treatment of non-adiabatic clouds may cause problems in mixed layer formulations (e.g., Woods 2009), since these treatments constrain the LWP be adiabatic. The diurnal cycle of the boundary layer results in changes of the liquid water path as well. This study used the data collected around the same time of day, which minimizes the influence of diurnal cycle. Although models (Ackerman et al. 2004;

Bretherton 2007) indicate that the sedimentation of the larger droplets near cloud top may under some conditions decrease entrainment efficiency that can increase the cloud water content when CCN concentrations are low, in the cases we have studied these effects appear to be dominated by other processes. Although the variance of the vertical velocity in the cloud layer associated with the thicker cloud is greater than that of the thinner clouds, we were unable to show that the entrainment rates for the high CCN case are significantly larger than the low CCN cases. Since the observed liquid water path may result from processes operating before the observations were made, any enhanced precipitation that may have occurred during the earlier history of the clouds could have been a contributing factor. The satellite derived LWP and R_e fields obtained upstream prior to the flight observations indicate that the clouds under the low CCN concentrations were characterized with small cellular like structures and cloud rifts. Because the clouds were thicker with higher LWP during the night hours, the cellular like structures and cloud rifts could be a sign of drizzling event based on previous observational and numerical studies (e.g., Sharon et al. 2006; Feingold et al. 2010). Further, precipitation earlier in the history of the low CCN clouds may have resulted in aerosol scavenging and removal that could either reduce the CCN concentrations or help maintain the low values observed. On the other hand, the satellite retrievals show that the clouds under the high CCN concentrations were solid over large area and have minimal LWP loss due to precipitation suppression effects.

These results provide new evidence for CCN and LWP relationships that are not fully explained by current hypotheses from numerical modeling. Although the strategy we used here of comparing cases where the meteorology and the boundary layer structure are very similar, we cannot eliminate the possibility that the changes in CCN may be associated with small changes in the large-scale forcing that in turn may also affect the LWP. True cause and effect cannot be established. Thus this work may motivate further studies to better explain the factors that control LWP and the role that the second indirect effects may play in the evolution of clouds.

Chapter 4: The impact of large-scale forcing and aerosol variation on simulated stratocumulus clouds

4.1 Motivation and background

As noted in Chapter 1.2, meteorological and aerosol factors can control the variations of marine Sc cloud amount. Previous studies established that lower tropospheric stability, SST and SST gradient, surface wind and divergence, and the relative humidity of the cloud layer, etc. are the main meteorological factors (Norris 1998; Klein and Hartmann 1993; Stevens and Brenguier 2008; Klein 1997). At synoptic and subseasonal time scales, such large scale factors have significant correlations with the variations of marine stratocumulus clouds. However, these factors can only explain less than 20% of the variance in marine Sc clouds amount (Klein 1997; Xu et al. 2005). The weak correlations between the large scale forcing and the Sc cloud amount at synoptic time scale might be due to the contributions of nonlocal factors such as the history of large scale forcing (i.e. upstream effects), the contributions of mesoscale systems, the effects of the internal marine boundary layer (BL) process and aerosols.

Because large eddies usually dominate the turbulent transports within the BL (Nucciarone and Young 1991), large-eddy simulation (LES), which can explicitly resolve the energetics of the large eddies, has been an important tool to study the Sc-topped BL (e.g., Ackerman et al. 2009; Hill and Feingold 2009). The Global Energy and Water Exchange Cloud System Study (GCSS) project Boundary Layer Cloud Working Group conducted several inter-comparison studies with a range of LES models (e.g., Moeng et al. 1996; Stevens et al. 2005; Ackerman et al. 2009), aiming at evaluating the performance of LES in marine Sc

clouds. An inter-comparison project of a non-drizzling Sc case (Stevens et al. 2005) indicated that LESs with high enough vertical resolution ($\leq 5\text{m}$ near the inversion) or low enough sub-grid mixing at cloud top are able to well capture the general features of the non-drizzling Sc-topped BL and the turbulence structure. An evaluation of LESs of a drizzling Sc (Ackerman et al. 2009) found that the mean LWPs of most models with drizzle and cloud water sedimentation were consistent with the observations, while the simulated turbulence structures (e.g., vertical velocity variance $\overline{w'w'}$ and the mean third moment of the vertical wind) were shown to have some discrepancies from observations. The temporal variability of large-scale forcing can be represented in LES in terms of horizontal advection, subsidence rate, and pressure gradient force etc. Considering the time-varying large scale forcing in long simulations was found to reproduce the observed temporal variations of the BL properties with some fidelity in previous LES studies (de Szoeke and Bretherton 2004; Caldwell and Bretherton 2009).

Although with limitations (see Chapter 4.6 for details), the state-of-art three dimensional LES model that can fill the gap between the low-resolution mesoscale numerical model and the direct numerical simulation (DNS) mode and has several advantages in Sc studies: 1) the key cloud controlling processes and prescribed external forcing in LES are controllable, and thus it can be used to examine the contribution of each process on the cloud and BL evolution; 2) the comprehensive continuous 3D model output offers us a chance to investigate the physical mechanisms that underline the limited observations in the real world; 3) LES could be a guide line for mixed-layer models and cloud parameterization schemes

because LESs involve the vertical variations of the turbulence transports and the nonlinear responses of BL processes that are found to be important to Sc clouds simulations (e.g., Sandu et al. 2009; Zhu et al. 2005; Cheng and Xu 2009).

These advantages of LES motivate us to explore the contributions of the important metrological controlling factors such as SST, large-scale subsidence, and vertical wind shear, along with the aerosol factors such as CCN number concentrations on the observed cloud and BL variations at Point Alpha by way of LES studies. Section 4.2 describes the LES model adopted in this study. Two sets of LES to study the impact of large-scale forcing and the impact of CCN number concentrations are discussed in section 4.3 and 4.4, respectively. Section 4.5 summarizes the main results and discusses some limitations and issues regarding the LES technique.

4.2 Model description

The LES model adopted in this study is System for Atmospheric Modeling (SAM), which is described by Khairoutdinov and Randall (2003) in detail. SAM was one of the model members in the GCSS LES intercomparison projects and showed a similar simulation capability of representing the Sc-topped BL to that of other model members (Moeng et al. 1996; Siebesma et al. 2003; Stevens et al. 2005; Cheng and Xu 2009; Ackerman et al. 2009; etc.). SAM has also been used in studies of diurnal cycle, cloud top entrainment, and aerosol indirect effects in Sc (Bretherton et al. 2007; Yamaguchi and Randall 2008; Caldwell and Bretherton 2009).

4.2.1 Dynamic framework

SAM is a non-hydrostatic model based on the Ogura-Phillips anelastic equations (Ogura and Phillips 1962). There are four main prognostic variables in SAM: 1) velocity vectors (u , v , w); 2) total water mixing ratio q_T , including water vapor mixing ratio q_v , cloud liquid water mixing ratio q_c if cloud is allowed, cloud ice mixing ratio q_i if ice phase cloud is considered, and total precipitating water mixing ratio q_p (rain q_r , snow q_s , and graupel water mixing ratio q_g if precipitation component is allowed; 3) liquid/ice water static energy $s_l = c_p T + gz - L_c(q_c + q_r) - L_s(q_i + q_s + q_g)$; and 4) subgrid-scale (SGS) TKE.

The prognostic equations used in SAM (Khairoutdinov and Randall 2003) are described in tensor notation as:

$$\frac{\partial u_i}{\partial t} = -\frac{1}{\bar{\rho}} \frac{\partial}{\partial x_j} (\bar{\rho} u_i u_j + \tau_{ij}) - \frac{\partial}{\partial x_i} \frac{p'}{\bar{\rho}} + \delta_{i3} B + \epsilon_{ij3} f (u_j - U_{gj}) + \left(\frac{\partial u_i}{\partial t} \right)_{l.s.} \quad (4.1)$$

$$\frac{\partial}{\partial x_i} \bar{\rho} u_i = 0 \quad (4.2)$$

$$\frac{\partial s_l}{\partial t} = -\frac{1}{\bar{\rho}} \frac{\partial}{\partial x_i} (\bar{\rho} u_i s_l + F_{sli}) - \frac{1}{\bar{\rho}} \frac{\partial}{\partial z} (L_c P_r + L_s P_s + L_s P_g) + \left(\frac{\partial s_l}{\partial t} \right)_{rad} + \left(\frac{\partial s_l}{\partial t} \right)_{l.s.} \quad (4.3)$$

$$\frac{\partial q_T}{\partial t} = -\frac{1}{\bar{\rho}} \frac{\partial}{\partial x_i} (\bar{\rho} u_i q_T + F_{qTi}) - \left(\frac{\partial q_T}{\partial t} \right)_{mic} + \left(\frac{\partial q_T}{\partial t} \right)_{l.s.} \quad (4.4)$$

$$\frac{\partial q_p}{\partial t} = -\frac{1}{\bar{\rho}} \frac{\partial}{\partial x_i} (\bar{\rho} u_i q_p + F_{qp i}) + \frac{1}{\bar{\rho}} \frac{\partial}{\partial z} (P_r + P_s + P_g) + \left(\frac{\partial q_p}{\partial t} \right)_{mic} + \left(\frac{\partial q_p}{\partial t} \right)_{l.s.} \quad (4.5)$$

where u_i ($i=1, 2, 3$) are the resolved velocities (u , v , w), respectively; $\bar{\rho} = \rho_o(z)$ is the mean state profile of air density; p is pressure; f is Coriolis parameter; U_g is prescribed geostrophic wind; B is buoyancy; g is gravitational acceleration; c_p is the specific heat of dry air at constant pressure; L_c is latent heat of evaporation and L_s is latent heat of sublimation; τ_{ij} is subgrid-scale stress tensor; F_{xx} are corresponded subgrid-scale scalar fluxes; P_x are precipitation fluxes of

each specific phase; $()_{\text{rad}}$ represents the tendency due to radiative processes; $(\frac{\partial q_T}{\partial t})_{\text{mic}}$ denotes the q_T tendency including evaporation/condensation and precipitation which have been parameterized by a bulk microphysical scheme (see Chapter 4.2.2); $(\frac{\partial q_p}{\partial t})_{\text{mic}}$ denotes the q_p tendency due to autoconversion and accretion processes (see Chapter 4.2.2); $()_{\text{l.s.}}$ indicates the tendency due to the prescribed large-scale tendency. All the terms related to the ice phase (q_s , q_i , q_g , P_s , P_i , P_g) can be ignored in this study since we are focusing on marine Sc.

The momentum equations are spatially discretized with second-order centered difference scheme and integrated using the third-order Adams-Bashforth scheme with a variable time step determined by the Courant–Friedrichs–Lewy condition. A second-order monotonic and positive definite advection scheme (Smolarkiewicz and Grabowski 1990) is used for all scalars. A 5th- order flux-corrected advection scheme with the similar computational efficiency (Yamaguchi et al. 2011) has been available since version 6.9.

The available SGS schemes include a 1.5-order sub-grid scale closure (prognostic SGS TKE, Khairoutdinov and Kogan 1999) and a simple first-order Smagorinsky-type closure. The 1.5-order closure scheme is similar to the Deardorff (1980) SGS model. The model uses periodic lateral boundary conditions and a rigid lid at the top of the domain with a Newtonian damping layer in the upper third of the domain to reduce gravity wave developing and reflection. The surface fluxes can be prescribed as constant values or computed using Monin–Obukhov similarity.

4.2.2 Microphysical scheme

This study employs a double - moment bulk microphysics parameterization (Morrison et al. 2005) in SAM. Although this microphysical scheme parameterizes ice phase and mixed phase clouds processes, we just discuss the warm cloud component here.

Three prognostic water mass variables and number concentration variables are used in this microphysical scheme if the simulated clouds are liquid phase:

water vapor mixing ratio q_v (g/kg), cloud liquid water mixing ratio q_c (g/kg), rain/drizzle water mixing ratio q_r (g/kg), cloud droplet number concentration N_d ($\#/cm^3$), and rain/drizzle drop number concentration N_r ($\#/cm^3$).

The time tendencies of q_c and N_d due to condensation/evaporation are derived from q_t , air temperature, and pressure by assuming zero super-saturation, a so-called saturation adjustment. Therefore, condensation/evaporation in this scheme occurs instantaneously and is independent of the size distribution of the cloud droplets.

There are two options for autoconversion and accretion processes in this microphysical scheme (Khairoutdinov and Kogan 1999; Seifert and Beheng 2001). The drizzle and cloud droplet self-collections are parameterized as Seifert and Beheng (2001, Eq. A8-9). The size threshold between droplets and drizzle drops is 50 micron in diameter. The sub-cloud evaporation of rain water is considered as well. The terminal fall velocities of cloud droplets and rain/drizzle drops are based on a formula in Morrison et al. (2005, Eq. A4).

Droplet activation is based on Eq. (14-17) in Morrison et al. (2005). The cloud droplets activated at any time step is equal to the difference between the diagnostic CCN number concentration based on a derived pseudoequilibrium peak supersaturation and the existed cloud droplet number concentration. Aerosol regeneration and cloud processing has not yet been considered in this scheme.

4.2.3 Radiative scheme

The longwave and shortwave radiative schemes in this study are from the National Center for Atmospheric Research (NCAR) Community Atmosphere Model (CAM 3.0; Collins et al 2006). The longwave radiative transfer in CAM3.0 is based on an absorptivity/emissivity formulation of the longwave radiation (Ramanathan, V., and P. Downey, 1986). The parameterization for water vapor is from Collins et al. (2002), while the other major absorbers (O_3 and CO_2) are the same in all of the simulations in order to minimize the effects of these absorbers. The radiative transfer and the net radiation heating rate are calculated for each grid column with the simulated cloud water mixing ratios.

In CAM 3.0, insolation is computed based on the method of Berger (1978). The δ -Eddington approximation (Joseph et al. 1976; Coakley et al. 1983) has been adopted to simulate the reflection, absorption, and scattering of the shortwave radiation under both clear-sky and overcast conditions. The liquid water cloud scattering and absorption are computed from the cloud liquid water path and cloud droplet effective diameter according to Slingo (1989). In this scheme, the cloud droplet effective diameter over the ocean is assumed to be 14 micron. The effects

of aerosol-absorbing properties on the simulated cloud are not considered in this study.

4.3 The impact of large-scale forcing

4.3.1 Simulation design

Table 4.1 Summary of the simulations.

Type	Variables	Range
Initial conditions	Latitude, longitude	20°S, 72°W
	Local time	From 18:00 LT to 09:00 LT
	Surface reference pressure	1015 hPa
	Geostrophic wind speed and direction	No wind; 4 m/s, 180° within the BL, 2 m/s, 360° above
	Initial SST	18°C
	Initial large-scale divergence	$2\text{--}3.5 \times 10^{-6} \text{ s}^{-1}$
	Boundary layer θ_l	288.5 K
	Boundary layer q_t	7.2 g/kg
	θ_l just above the inversion	300.6 K
	q_t just above the inversion	[1.1 2.1] g/kg
	Cloud number concentration	100 cm^{-3}
	Domain	4.8kmx4.8kmx1860m
	Horizontal resolution	50 m
Model configuration	Vertical resolution	Stretched grids with the highest resolution of 5m within the cloud layer and near the inversion
	Vertical levels	192
	Boundary conditions	Periodic lateral boundary condition A sponge layer in the upper third of the domain
	Time step	0.5 s
	Duration	15 hours
	SGS model	1.5-order closure scheme
	Radiation heating rates	Updated every 5s.

This numerical study includes 11 three-dimensional numerical simulations with varied conditions to estimate the sensitivity of the simulated cloud to large-scale subsidence, surface fluxes, moisture above the inversion, vertical wind shear and solar radiation. The initial conditions and prescribed large-scale forcing such as large-scale wind field, SST, and surface friction velocity are based on the observed ranges at Point Alpha during VOCALS-REx (Table 4.1).

The initial profiles of θ_i and q_i within the BL and the cloud droplet number concentration are the same among all 11 simulations (Fig. 4.1). The 11 simulations (see Table 4.2 for details) consist of five with relatively large large-scale divergence ($3.5 \times 10^{-6} \text{ s}^{-1}$, Cases 1-3, Case 8, Case 10) and the other six with a small divergence of $2.0 \times 10^{-6} \text{ s}^{-1}$ (Cases 4-7, Case 9, Case 11). Among Cases 1-3, the surface latent heat fluxes and sensible heat fluxes vary due to the different evolutions of SST. In addition, q_i above the inversion is set to be either 1.1 g/kg or 2.1 g/kg, and $\Delta\theta_i$ across the inversion is set to be either 12 K or 16 K to capture the observed variation during the Twin Otter project (Chapter 2). Cases 1-4 have no background flow, while Cases 5-7 consider a vertical wind shear of 6 m/s right across the inversion, a typical wind pattern at Point Alpha during the Twin Otter project (Zheng et al. 2011). There is no large scale horizontal wind when geostrophic wind is set to zero ($\bar{\vec{V}} = 0$). However, the total wind field is not zero due to the BL processes ($\vec{V} \neq 0$). Due to the existence of surface wind, the surface fluxes in Case 6 are significantly larger than those in the other cases (e.g., LHF is about 100 W m^{-2} vs. 67 W m^{-2} in Cases 1-5). Therefore, to exclude the effects of increased surface heat and moisture supply on the simulated cloud and BL, Case

5 is set with prescribed constant surface fluxes at a magnitude similar to those in the other cases. All simulations, except Case 7, exclude shortwave radiation, i.e., the clouds are treated as nocturnal Sc. Case 7 includes solar radiation during the last three hours of the simulation, because most of the Twin Otter flights started a couple of hours after sunrise and lasted about three hours. The surface fluxes in Cases 8-9 are prescribed to be similar to those in Case 6 (Table 4.2). The large-scale subsidence is specified by the large-scale divergence:

$$w(z) = -D \times z \quad (4.6)$$

where D is the mean large-scale divergence (s^{-1}) and z is the altitude (m).

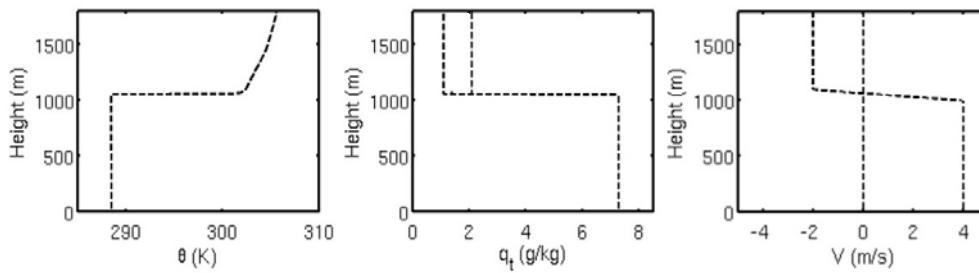


Figure 4.1 Initial soundings of a) potential temperature (K); b) total water mixing ratio (g/kg); c) south-north wind component (m/s).

In Table 4.2, Div is the prescribed surface divergence in the simulations. It controls the large scale subsidence at the top of the BL. q_{ta} is the initial total water mixing ratio above the inversion. V shows the magnitude of the vertical wind shear.

Each simulation is integrated for 15 hours with a time step of 0.5 s. After about a 2-3 hour “spinup” period, the turbulence becomes fully built up, and the evolutions of the simulated cloud and BL structures of the 11 cases clearly differ due to the impacts of the prescribed large scale forcing. Most of the analyses shown in the following section mainly focus on the last hour of the simulations.

Table 4.2 Summary of the large-scale forcing in the simulations.

Case	Div $\times 10^{-6} \text{ s}^{-1}$	SST $^{\circ}\text{C}$	LHF, SHF W m^{-2}	Δq_t g kg^{-1}	$\Delta \theta_l$ K	Geostrophic wind	Radiation
1	3.5	18	Diagnostic values	6.1	12	0	Longwave
2	3.5	17	Diagnostic values	5.1	12	0	Longwave
3	3.5	18	Diagnostic values	5.1	12	0	Longwave
4	2.0	18	Diagnostic values	5.1	12	0	Longwave
5	2.0	18	67, 10.3	6.1	12	4m/s, 180° within the BL, 2m/s, 360° above the inversion	Longwave
6	2.0	18	Diagnostic values	6.1	12	Same as above	Longwave
7	2.0	18	67, 10.3	6.1	12	Same as above	Shortwave and longwave
8	3.5	18	100,14	6.1	12	0	Longwave
9	2.0	18	100,14	6.1	12	0	Longwave
10	2.0	18	Diagnostic	6.1	16	0	Longwave
11	3.5	18	Diagnostic	6.1	16	0	Longwave

4.3.2 Simulation results

a) Overview

A snapshot of the simulated albedo (Fig. 4.2a) calculated based on the cloud LWP and cloud droplet concentration (Savic-Jovcic and Stevens 2008) indicates that the simulated clouds in most cases are solid non-drizzling Sc. The vertical profiles of the simulated and observed $\overline{w'w'}$, buoyancy flux, and total water flux are shown in Fig. 4.3. The simulated turbulence profiles capture the general patterns of the observed turbulence profiles but with substantial variations among these cases. The simulated total water fluxes have minimum near the cloud base

on all 11 cases probably because most of the simulated inversion heights are larger than 1000m and the BL is unable to completely mixed, which is similar to the observed features. However, the simulated profiles, especially at the upper BL, tend to be stronger than the observations. The simulated $\overline{w'w'}$ at the upper BL vary between 0.25 and 0.55 $\text{m}^2 \text{s}^{-2}$, while the observed range is from 0.15 to 0.3 $\text{m}^2 \text{s}^{-2}$. The simulated total water fluxes near the cloud top reveal a clear diversity from less than 60 W m^{-2} to $\sim 120 \text{ W m}^{-2}$, which are much larger than the observed values of 10 to 40 W m^{-2} .

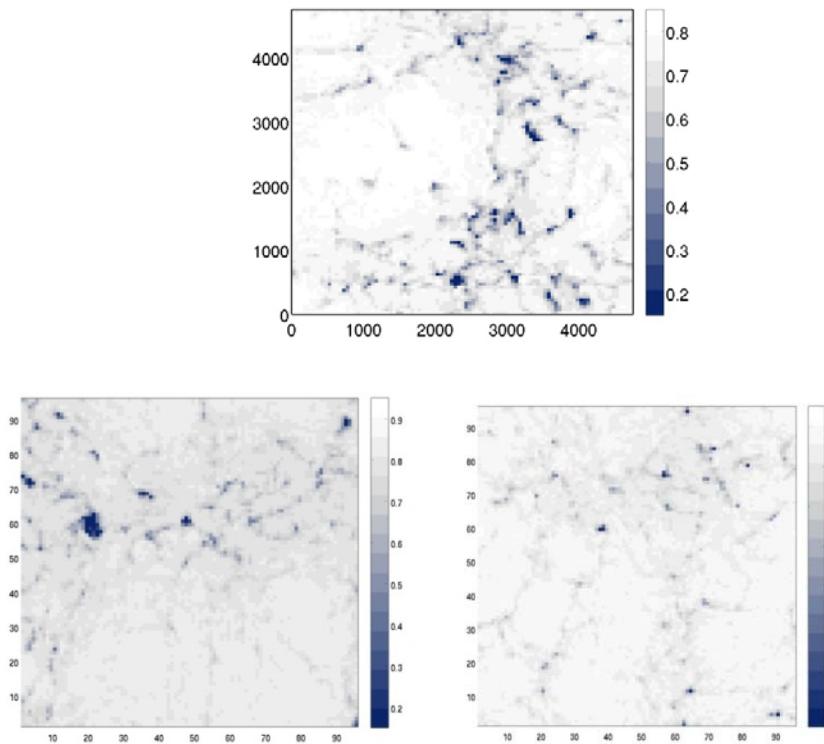


Figure 4.2 Snapshots of the albedo estimated with cloud water and cloud droplet number concentration a) Case 1, $t = 15$ hour; b) Case A0, $t = 15$ hour; c) Case A1, $t = 15$ hour.

The simulated in-cloud buoyancy fluxes are stronger than the observed in-cloud buoyancy fluxes in all 11 cases. There are two explanations for the stronger in-

cloud turbulence in the simulations: 1) there is no horizontal advection in the simulations, as shown in Chapter 2.4.3, to balance out part of the effects of the surface fluxes; 2) most simulations, except Case 7, exclude solar radiation. Previous studies (e.g., Hignett 1991; Bretherton et al. 2004; Caldwell et al. 2005) reveal that the in-cloud solar absorption could inhibit the BL turbulence, reduce the coupling of the cloud with the surface moisture supply, and decrease the cloud-top entrainment rate. The effect of solar radiation on the simulated clouds in this study will be discussed separately at the end of this section.

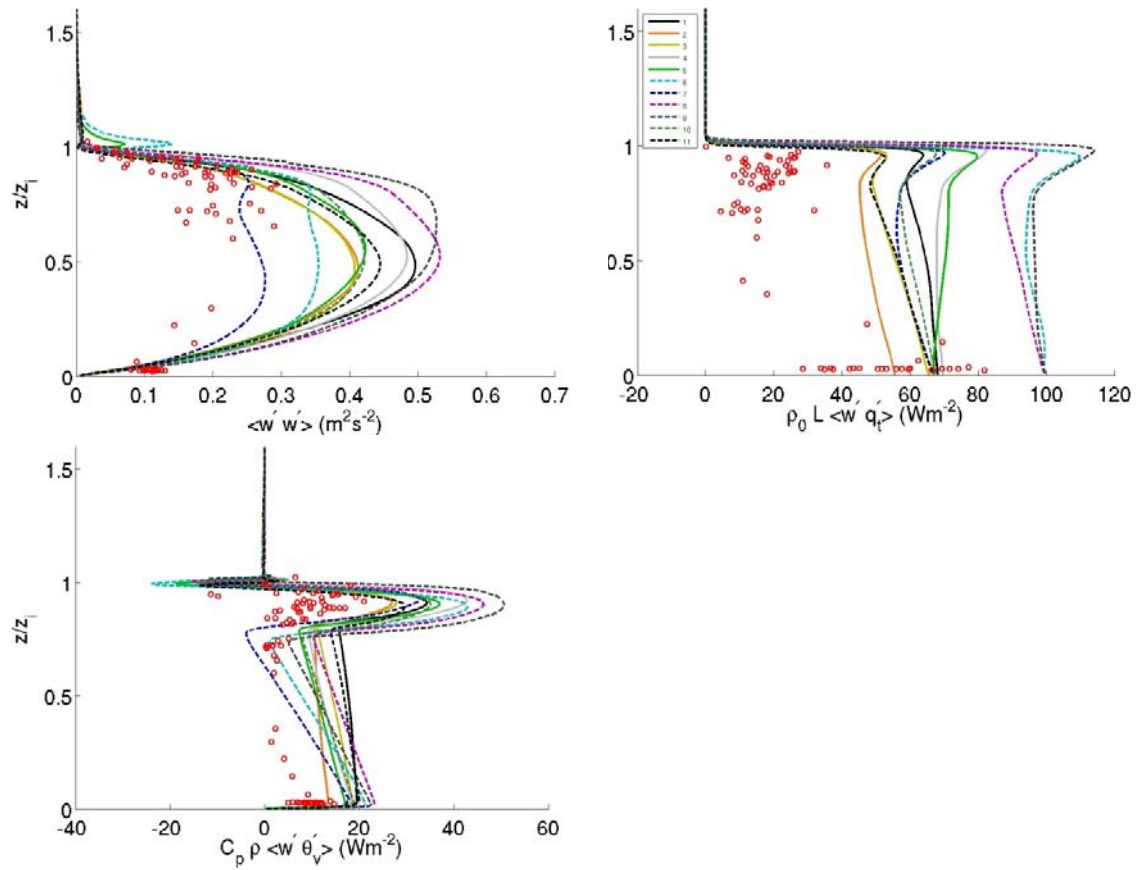


Figure 4.3 a) Vertical velocity variance ($\text{m}^2 \text{s}^{-2}$), b) Total water flux (W m^{-2}), and c) Buoyancy flux (W m^{-2}) vs. normalized height calculated from all 11 cases, $t=15$ hour. Red open symbols are from observations (10 flights) of the typical well-mixed boundary layer and non-drizzling Sc discussed in Chapter 2.

There are several different definitions of the inversion height such as the mean height of the maximum vertical gradient of θ_l (e.g., Serpetzoglou et al. 2008; Zheng et al. 2011) and the mean height of the largest vertical advection of q_t (Caldwell and Bretherton 2009). In this study, the inversion height is defined as the domain-mean height of the 5.5 g/kg q_t isosurface, which is similar to the definition used in the GCSS workgroup (Ackerman et al. 2009; Stevens et al. 2005). All of these definitions produce similar inversion height levels(not shown here) in the simulations, indicating that the simulated inversion height in this study is not sensitive to what definition is adopted.

$$z_i = \overline{z_{q_t=5}(l, j)} \quad (4.7)$$

$$LWP = \int q_c(z) dz \quad (4.8)$$

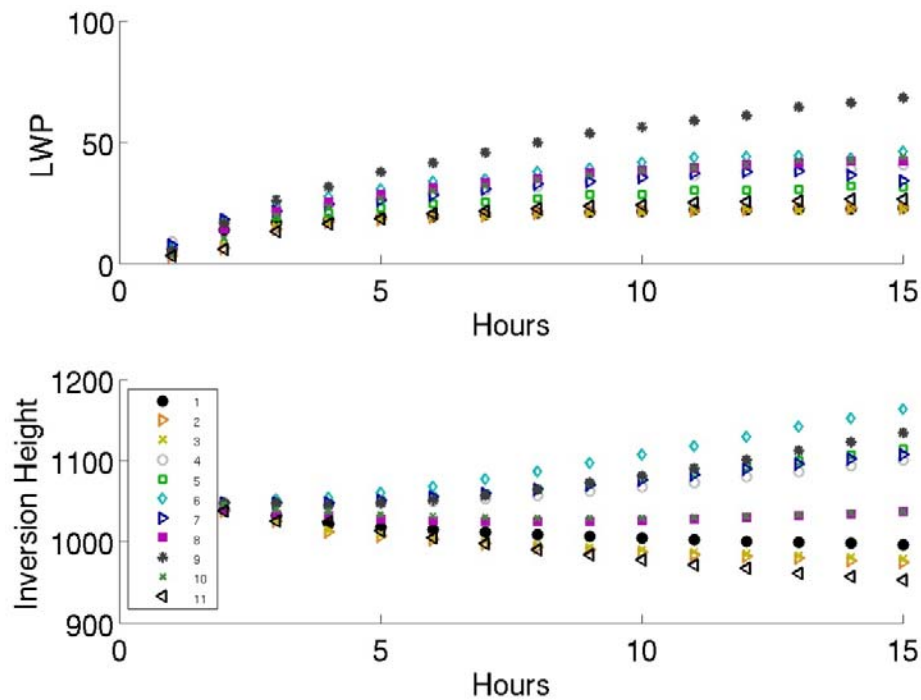


Figure 4.4 Time evolutions of a) LWP (g m^{-2}); b) BL inversion height (m) for all 11 cases.

The cloud LWPs and inversion heights vary substantially among these cases (Fig. 4.4). The cloud LWP in Case 9, a case with higher surface fluxes and lower surface divergence (Table 4.2), gradually increases and reaches a maximum value of 68.1 g m^{-2} , which is about three times those of Cases 1-3 at $t = 15$ hour. For Cases 1-3 with the same surface divergence of $3.5 \times 10^{-6} \text{ s}^{-1}$, the LWP is almost identical, with a value of 22 g m^{-2} , indicating that the observed variation of q_t above the inversion and surface fluxes have a limited impact on the cloud LWP within the framework of LES. In Case 7, the LWP reaches its maximum of 38 g m^{-2} right before sunrise ($t = 13$ hour), and then drops to 33.8 g m^{-2} due to the solar radiation warming. The inversion levels in Case 1-3 with the large surface divergence of $3.5 \times 10^{-6} \text{ s}^{-1}$ decrease with a similar trend throughout the simulation period, while those in Case 4-7 and Case 9 with the small surface divergence of $2.0 \times 10^{-6} \text{ s}^{-1}$ gradually deepen to different levels. Although the surface divergence in Case 8 is $3.5 \times 10^{-6} \text{ s}^{-1}$, the BL with significantly higher surface fluxes supply can offset the effect of the large-scale subsidence on the inversion height. Therefore, the inversion height in Case 8 keeps at a steady level.

In these cases, higher LWP corresponds to higher inversion height except for the higher $\Delta\theta_i$ cases (Cases 10-11). This relationship between LWP and inversion height is opposite to that observed at Point Alpha during VOCALS-REx (Chapter 3). A possible explanation for this discrepancy is that the observed Sc layers originated from different air masses and also experienced different large scale conditions prior to the flights (i.e. non-local effects). Nevertheless, the

simulations indicate the important role of large-scale divergence (i.e. large-scale subsidence) on the BL and cloud evolutions. The high sensitivity of the simulated BL and cloud layer to the large-scale subsidence implies that the large-scale circulation, particularly the large-scale subsidence, must be accurate enough to successfully simulate the Sc cloud.

We diagnose the different features of these 11 cases, including entrainment rate w_e , integrated turbulence kinetic energy (TKE), and convective vertical velocity (w^*) to explore the possible main factors contributing to the simulated LWP and inversion height variations.

$$w_e = \frac{\delta z_i}{\delta t} + Div(z_i) \times z_i \quad (4.9)$$

$$|TKE| = \int TKE(z) dz \quad (4.10)$$

$$w^* = (2.5 \int \overline{w'b'} dz)^{1/3} \quad (4.11)$$

In Table 4.3, LWP is the simulated LWP at $t = 15h$. z_i is the inversion height at $t = 15h$. SHF and LHF are the surface sensible heat flux and the surface latent heat flux, respectively, at $t = 15h$. w_e is the entrainment rate diagnosed from the growth rate of the BL depth and the large scale subsidence at the top of the BL (Eq. 4.9). $|TKE|$ is the vertical integrated TKE, which can represent the turbulence intensity through the whole BL (Eq. 4.10). w^* is the convective velocity scale related to the buoyancy flux and the BL depth (Eq. 4.11). b) The effect of the vertical wind shear

Over the SE Pacific coastal region, the large scale atmospheric circulation produces a strong persistent vertical wind shear across the inversion due to the existence of the Andes (Bretherton et al. 2010; Zheng et al. 2011; Jiang et al.

2010). Numerical and observational studies (e.g., Katzwinkel et al. 2011; Wang et al. 2012) suggest that the vertical wind shear could enhance the cloud-top turbulent mixing and entrainment rate in marine stratocumulus. Detailed observations near the top of the Sc layer indicate that the inversion zone itself can buffer the impact of the vertical wind shear (Katzwinkel et al. 2011). On the other hand, Wang et al. 2012 found that vertical wind shear can cause Sc-topped BL decoupling, and hence strongly impact on the cloud LWP and cloud amount.

Table 4.3 Results from the sensitivity to large-scale forcing.

Case	Comments*	LWP (g m ⁻²)	z _i (m)	SHF (W m ⁻²)	LHF (W m ⁻²)	w _e (mm s ⁻¹)	TKE (m ³ s ⁻²)	w* (m s ⁻¹)
1	LD_SF	22.7	996	11.8	68.1	3.1	761	1.12
2	LD_SSF	22.7	974	7.8	55.5	2.7	551	0.98
3	LD_SF_M	22.4	979	10.8	65.7	2.9	567	1.04
4	SD_SF	40.9	1101	11.0	69.0	4.2	755	1.12
5	SD_SF_VS	31.4	1114	10.3	67	4.2	692	1.06
6	SD_LF_VS	46	1163	13.3	99.5	5.7	586	1.09
7	SD_SF_VS_SR	33.8	1107	10.5	67	3.7	416	0.93
8	LD_LF	42.3	1038	14	100	4.4	747	1.17
9	SD_LF	68.1	1134	14	100	5.3	836	1.2
10	LD_HT	43.8	1037	11.5	68.0	2.7	645	1.07
11	SD_HT	26.3	952	12.0	67.0	2.1	645	1.07

* LD and SD denote large and small surface divergence, respectively; LF and SF represent large and small surface fluxes, respectively; VS means vertical wind shear; M is higher moisture above inversion; SS stands for solar radiation; HT indicates higher potential temperature above inversion.

To estimate the impact of the observed vertical wind shear on the cloud LWP and BL structure, we introduce a vertical wind shear of 6 m/s right across the inversion into Cases 5-6. In Case 5, whose surface fluxes are set to be comparable to the observed values, the cloud LWP is smaller by 9.5 g m^{-2} (25%) than that in Case 4; while in Case 6, whose surface flux supplies are much larger than the observed values, the cloud LWP still decreases by 22 g m^{-2} (32%) compared with Case 9.

As for the BL turbulence structure, w_e in the cases with vertical wind shear are clearly larger than that in the cases without the vertical wind shear. The shear-induced mixing processes, however, have similar effects on the low surface fluxes cases (Case 4 and Case 5) and the large fluxes cases (Case 6 and Case 9) in terms of TKE and w^* . For the small surface fluxes cases, the $|TKE|$ and w^* in Case 5, a case with vertical wind shear, are lower by $63 \text{ m}^3 \text{ s}^{-2}$ (11%) and 0.06 m s^{-1} , respectively, than those in Case 4. The profile of $\overline{w'w'}$ also shows that the cloud-top $\overline{w'w'}$ in Case 5 is clearly higher than that in Case 4. The total water flux at the lower BL in Case 5 is slightly larger than that in Case 4. For the large surface fluxes cases, the $|TKE|$ and w^* in Case 6 are higher by $250 \text{ m}^3 \text{ s}^{-2}$ (-30%) and 0.11 m s^{-1} (-9%), respectively, than those in Case 9. The shear-induced turbulence in Case 6 increases the cloud-top $\overline{w'w'}$, but weakens the buoyancy flux near the cloud base compared with Case 9 (Fig. 4.3).

Based on the above results, the shear-induced decoupling process mentioned in the numerical study of Wang et al. (2012) tends to happen in Case 6. The shear-induced mixing near the cloud top is stronger in Case 6 than in

Case 5 as shown in the profiles of $\overline{w'w'}$. The BL in Case 5 shows slightly lower buoyancy production near the cloud base than that in Case 4. In Case 6, the strongly increased cloud-top mixing entrains more warm and dry air above the inversion. The enhanced entrainment process combining with the effect of large surface fluxes (Bretherton and Wyant 1997) causes the BL decoupling.

c) The effect of the surface fluxes

The sensitivity of Sc-topped BL to the surface fluxes has been estimated in several studies with mixed-layer models and cloud-resolving models (e.g., Schubert et al. 1979; Bretherton and Wyant 1997; etc.). However, how the surface fluxes interact with other large scale factors such as vertical wind shear is less known. In order to estimate the different roles that the surface fluxes might play under different large scale conditions, we arrange six of the 11 simulations to form three groups of simulations: 1) G_LD, including Case 1 and Case 8, which have a larger surface divergence of $3.5 \times 10^{-6} \text{ s}^{-1}$ and no vertical wind shear; 2) G_SD, including Case 4 and Case 9 with a smaller surface divergence of $2.0 \times 10^{-6} \text{ s}^{-1}$ and no vertical wind shear; 3) G_SD_VS, including Case 5 and Case 6, which have the same smaller surface divergence and a 6 m/s vertical wind shear.

Clearly, cases with larger surface fluxes have larger total water fluxes throughout the whole BL at $t = 15$ hour (Fig. 4.3b). The inversion heights, entrainment rates, and LWPs in these cases are higher than the others. The profiles of buoyancy flux and $\overline{w'w'}$, however, show different feature among these three groups. In G_LD, |TKE| in Case 8 is lower by $14 \text{ m}^3 \text{ s}^{-2}$ (-2%) than that in Case 1, while in G_SD, |TKE| in Case 9 is higher by $214 \text{ m}^3 \text{ s}^{-2}$ (34%) than that in

Case 4 (Table 4.4). In G_SD, the BL and cloud layer in Case 9 are still growing, and the BL turbulences are clearly stronger than that in Case 4 in terms of $\overline{w'w'}$ and in-cloud buoyancy flux. In G_SD_VS, |TKE| in the case with large surface fluxes (Case 6) is lower by $106 \text{ m}^3 \text{ s}^{-2}$ (15%) than the case with small surface fluxes (Case 5), because the vertical wind shear enhances the entrainment process and deepens the BL depth. Furthermore, the buoyancy flux indicates that the BL in Case 6 tends to decouple due to the effects of vertical wind shear and large surface fluxes.

Therefore, increasing surface fluxes under the condition of large surface divergence can significantly increase the cloud LWP by raising the cloud-top height. Under the condition of vertical wind shear, increasing surface fluxes enhances entrainment processes, and then weakens the buoyant production of turbulence. This process may cause BL decoupling later in the simulation.

Table 4.4 Summary of the differences between the cases with large and small surface fluxes.

Group	ΔLWP		Δw_e		$\Delta \text{TKE} $		Δw^*	
	(g m^{-2})	(%)	(mm s^{-1})	(%)	($\text{m}^3 \text{ s}^{-2}$)	(%)	(m s^{-1})	(%)
G_LD	19.6	86%	1.3	42%	-14	-2%	0.05	4%
G_SD	16.2	39%	1.2	2.9%	214	34%	0.15	14%
G_SD_VS	14.6	46%	1.5	35%	-106	-15%	0.03	3%

d) The effect of the large scale divergence

The time series of hourly LWP and inversion height (Fig. 4.4) reveal the large impact of surface divergence on the simulated Sc-topped BL. When the surface divergence reduces from $3.5 \times 10^{-6} \text{ s}^{-1}$ to $2 \times 10^{-6} \text{ s}^{-1}$ (Case 1-3 vs. Case 4-6), the cloud LWP clearly increases from $\sim 20 \text{ g m}^{-2}$ to 40 g m^{-2} , and the entrainment

rate significantly increases as well (Table 4.3). Case 1 and Case 4 have the same setting except the surface divergence. The LWP and turbulence structures in Case 1 and Case 4 show that the Sc-topped BL could grow much deeper with a lower surface divergence; and if the surface moisture supply is sufficient, the cloud layer could be thicker during the BL deepening. Case 4 has a higher total water flux (Fig. 4.3b) in cloud layer with a peak value of about 75 W m^{-2} compared with Case 1 with a maximum of about 65 W m^{-2} . As the BL becomes deeper, however, $\overline{w'w'}$ (Fig. 4.3a) below the cloud layer in Case 4 is slightly weaker than that in Case 1 in the whole BL at $t = 15$ hour. The buoyancy fluxes (Fig. 4.3c) indicate that Case 4 has clearly lower buoyancy flux below the cloud layer. The integrated TKE in Case 1 ($761 \text{ m}^3 \text{ s}^{-2}$, Table 4.3) is similar to that in Case 4 ($755 \text{ m}^3 \text{ s}^{-2}$).

For the cases with much higher surface fluxes (Case 8 vs. Case 9), the cloud layer with lower surface divergence becomes thicker and the BL is deeper by about 100 m, which is consistent with the cases discussed above. The LWP in Case 9 is 68.1 g m^{-2} , while it is 42.3 g m^{-2} in Case 8. All of the parameters (e.g., $|\text{TKE}|$, w^* , $\overline{w'w'}$ and buoyancy flux) indicate that the BL turbulence intensity in Case 9 is stronger than Case 8 due to the prescribed much higher surface fluxes compared with observations.

e) The effect of solar radiation

Among the 11 cases, $\overline{w'w'}$ and buoyancy fluxes in Case 7 are the closest to the observations (Fig. 4.3 a,c). To exam the effect of solar radiation, we compare Case 7 with Case 5 that has the same conditions as Case 7 except

without solar radiation. After three hours of solar radiative warming, the BL turbulence in Case 7 weakens with decreasing entrainment rate. Case 7 has a $|TKE|$ is $276 \text{ m}^3 \text{ s}^{-2}$ lower than that in Case 5. The profile of $\overline{w'w'}$ in Case 7 shows that $\overline{w'w'}$ near the cloud base is lower than those in cloud layer and in the lower BL, which is similar to the observed pattern. The cloud-base total water flux and the in-cloud total water flux in Case 7 (Fig. 4.3 b) are lower by 20 W m^{-2} and $\sim 10 \text{ W m}^{-2}$, respectively, than those in Case 5. In addition, the buoyancy flux below the cloud layer becomes negative in Case 7. This indicates that the BL tends to decouple later on.

f) The effect of the BL-top stability ($\Delta\theta_i$)

Previous studies (e.g. Wood and Bretherton 2006) found that higher static stability near the BL top can weaken the cloud top entrainment and increase the cloud amount. We test the effect of the BL-top stability on the BL and cloud layer by performing Case 10 and Case 11 with a higher $\Delta\theta_i$ (16K) than that in Case 4 and Case 1 (12K, Table 4.2). In both of the higher $\Delta\theta_i$ cases (Case 10 and Case 11), the LWP are higher and z_i are lower than those in the lower $\Delta\theta_i$ cases (Case 1 and Case 4, Table 4.3). Comparison of the turbulence fluxes in those cases indicated that a higher $\Delta\theta_i$ can lead to reduced total water flux near the cloud top and decreased buoyancy flux in the cloud layer. Therefore, the turbulence becomes weaker in terms of $|TKE|$ and w^* in both Case 10 and Case 11 compared with Case 4 and Case 1, respectively.

4.4 The impact of CCN number concentrations

4.4.1 Simulation design

In order to estimate the impact of CCN number concentrations on the simulated Sc , particularly to isolate the sedimentation-entrainment feedback from the other controlling factors and to test it under different situations, we designed three different groups of simulations (Fig. 4.5, Table 4.5). The initial condition and large scale forcing among the three groups are within the observed ranges and represent three different scenarios of BL and Sc evolutions. The model configuration for all of these simulations is same as the simulations in section 4.3.1 (Table 4. 1).

The initial soundings and surface conditions for group A is based on the observed sounding on Oct. 19, 2008 with some modifications. The surface divergence is set to $3.5 \times 10^{-6} \text{ s}^{-1}$. The large-scale forcing is fixed throughout the simulation period. Group B adopts the observed sounding and surface conditions from the observed sounding on Oct. 27, 2008 with some modifications. The surface divergence is set to $2.0 \times 10^{-6} \text{ s}^{-1}$, and the prescribed SST increases from 292.6 to 293.2 K during the simulation. The initial soundings of group C are similar to those in group A (Fig. 4.5), except that the BL depth of group C is 155 m shallower than that of group A. In group C, the surface divergence is set to decrease from 2.0×10^{-6} to $1.5 \times 10^{-6} \text{ s}^{-1}$, and the SST is set to increase from 290.5 to 291.6 K during the simulation.

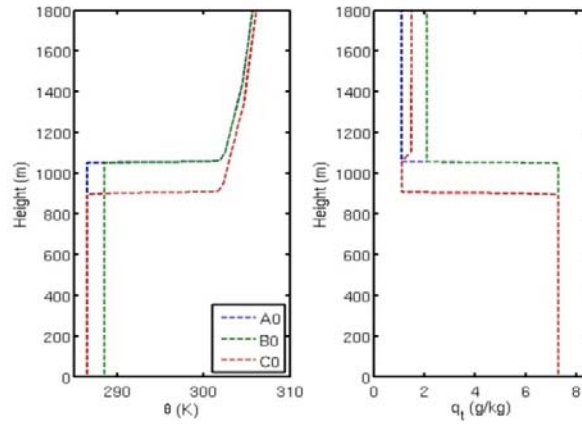


Figure 4.5 Initial soundings of a) potential temperature (K) and b) total water mixing ratio (g/kg) in group A, B, C.

Table 4.5 Sensitivity test for the aerosol number concentrations.

Case	Comments	SST (K)	Div ($\times 10^{-6} \text{ s}^{-1}$)	z_{i0} (m)	LWP ₀ (g m ⁻²)	LHF ₀ (W m ⁻²)	SHF ₀ (W m ⁻²)	CCN (cm ⁻³)
A0	Constant BL with thinning cloud layer	290.5	3.5	1055	117	50.1	9.6	200
A1				1055	117	50.1	9.6	2000
B0	Deepening BL with deepening cloud layer	292.6-293.2	2	1055	18	69.2	10.4	200
B1				1055	18	69.2	10.4	2000
C0	Deepening BL with constant cloud layer	290.5-291.6	2.0-1.5	900	47	51	9.7	200
C0.5				900	47	51	9.7	400
C1				900	47	51	9.7	2000

In each group, all the conditions and forcing are identical except that the CCN is set to 200 cm⁻³ for clean cases but to 2000 cm⁻³ for polluted cases. This difference of CCN is much larger than the observed aerosol variation (Fig. 2.16). Therefore, we test an additional case named C0.5 with CCN equal to 400 cm⁻³. The cloud droplet concentration (N_c) at the last hour of simulation in C0.5 is 150 cm⁻³, nearly twice as much as those in the clean cases (Table 4.6), to account for the largest observed variation of N_c . Since the turbulence structure in the

simulation at the spin-up period has not fully developed, we set the CCN number concentrations to be 200 cm^{-3} in both clean and polluted cases during the spin-up period ($t = 0 - 3$ hour). Similar to Sandu et al. (2009), the CCN number concentrations in polluted cases increase abruptly to 2000 cm^{-3} afterwards. We mainly focus on the simulation results after $t = 6$ hour, when the cloud processes have already adjusted to the increased CCN number concentrations.

4.4.2 Results

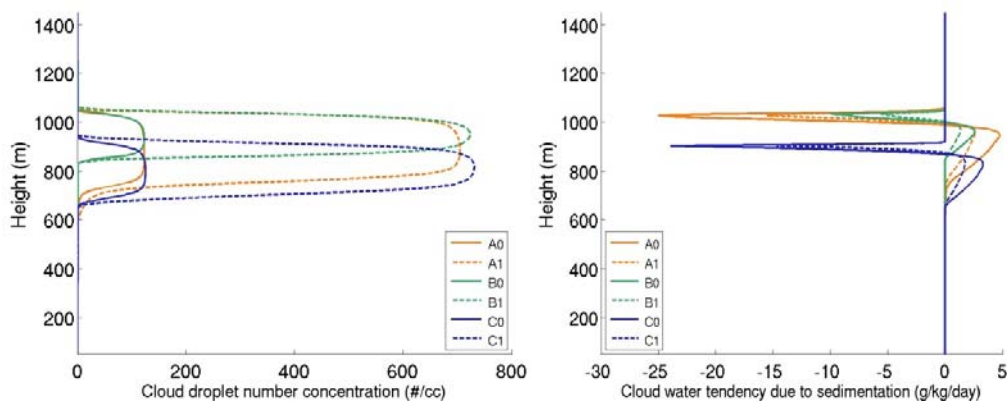


Figure 4.6 Domain-averaged profiles of a) cloud droplet number concentrations ($\#/\text{cm}^{-3}$); b) cloud water tendencies due to sedimentation (g/kg/day) in group A, B, C at $t = 6$ hour.

About three hours after increasing CCN number concentration in the polluted cases, the peak cloud droplet concentrations in polluted cases increase from around 100 cm^{-3} to 700 cm^{-3} , which are six times as much as the clean cases at the same time (Fig. 4.6a, Table 4.5). The differences are much larger than the observed variations (See chapter 2.6). The cloud droplet sedimentation in the polluted cases is about half of that in the clean cases (Fig. 4.6b). The BL turbulences become slightly weaker (Fig. 4.7a) compared with the clean cases, which is consistent with Bretherton et al. (2007). The LWPs of the polluted

clouds decrease by less than 10% at $t = 15$ hour and the LWP in the double-CCN case (C0.5) is even almost identical to the clean case C0 (Table 4.6, Fig. 4.8). The entrainment rates in A1 and B1 are 0.2 mm s^{-1} higher than those in A0 and B0, respectively, whereas C1 has an entrainment rate identical to that in C0. The snapshots (Fig. 4.2b, c) of the simulated albedo in Group A indicate that the clouds are nearly solid Sc. The clean cloud is slightly darker than the polluted cloud due to the first aerosol indirect effect (Twomey, 1977).

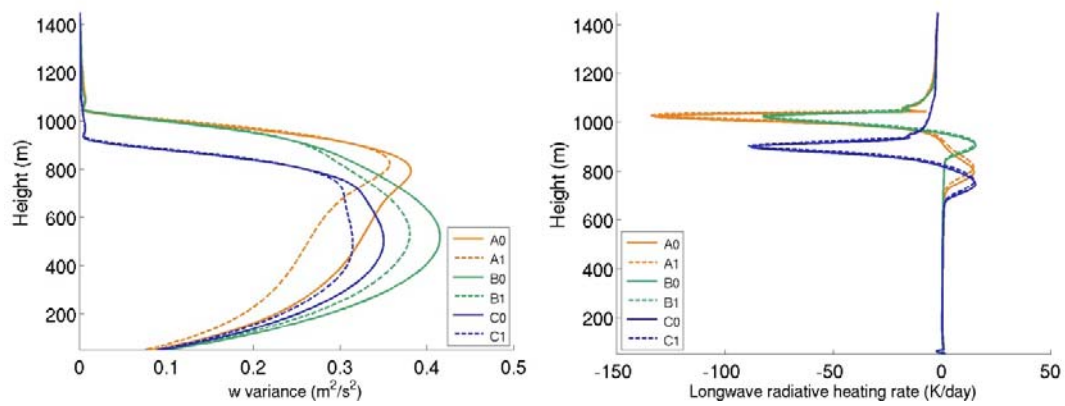


Figure 4.7 The 4-9 hour mean profiles of a) vertical velocity variance (m^2s^{-2}); b) longwave radiative heating (K day^{-1}) in group A, B, C.

In order to estimate the feedback of cloud-top entrainment to increased cloud droplet concentration, we analyze the simulated 3-D cloud-top interfaces in all cases at $t = 15$ hour. When a warm and dry air parcel above the cloud is entrained, it is lighter than the cloudy air around it. Without mixing, it will stop sinking and even rise up due to the positive buoyancy. In fact, however, it tends to mix with the cloudy air by small scale eddies and molecular diffusivity (Haman et al. 2007; Mellado 2010). As a result, the air could be cooled by the evaporation of cloud water, and become easier to sink into the BL. There are several indexes representing how likely the cloud will be impacted by the evaporation driven

entrainment processes (e.g., Randall, 1980; Kuo and Schubert, 1988; Siems et al. 1990; Duynkerke 1993 et al. see a summary in Yamaguchi and Randall, 2008). This study adopts the entrainment criteria k (Eq. 5.1, Lilly 2002) to diagnose the ratio of the available evaporation cooling and the stable stratification the parcel needs to overcome:

$$k = - \frac{L\Delta q_t}{c_p\Delta\theta_l} \quad (4.12)$$

where L is the latent heat of condensation, c_p is the specific heat of dry air at constant pressure, Δq_t is the jump of q_t across the cloud-top interface, $\Delta\theta_l$ is the jump of liquid water potential temperature across the cloud-top.

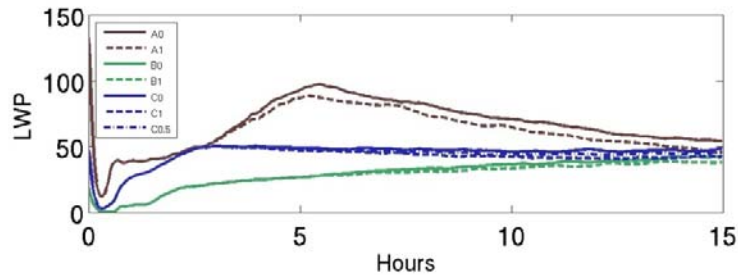


Figure 4.8 Time evolutions of the simulated LWP (g m^{-2}).

For each group, the polluted case has lower k than that of its clean counterpart, indicating that the cloud liquid water near the cloud top alone cannot cause the buoyancy reversals in both cases (Table 4.6). Therefore, the analyses show that the increased liquid water evaporation within the entrainment zone is not the main cause of the LWP decrease in the high-CCN cloud. The evaporative cooling within the entrainment zone is limited by the small cloud water mixing ratio in non-drizzling Sc. Furthermore, the cloud – top long wave radiative cooling

around the entrained air prevents the entrained air mass from being turned in to negative buoyant parcel by evaporative cooling (Fig. 4.7b).

Table 4.6 Results from the sensitivity to CCN number concentrations.

Case	A0	A1	B0	B1	C0	C0.5	C1
\overline{N}_c (cm ⁻³)	86	520	82	465	86	150	481
LWP (g m ⁻²)	53	47	42	38	47	45	43
k	1.03	1.02	1.24	1.23	1.14	1.13	1.12
w_e (mm s ⁻¹)	3.3	3.5	4.1	4.3	3.9	3.9	3.9

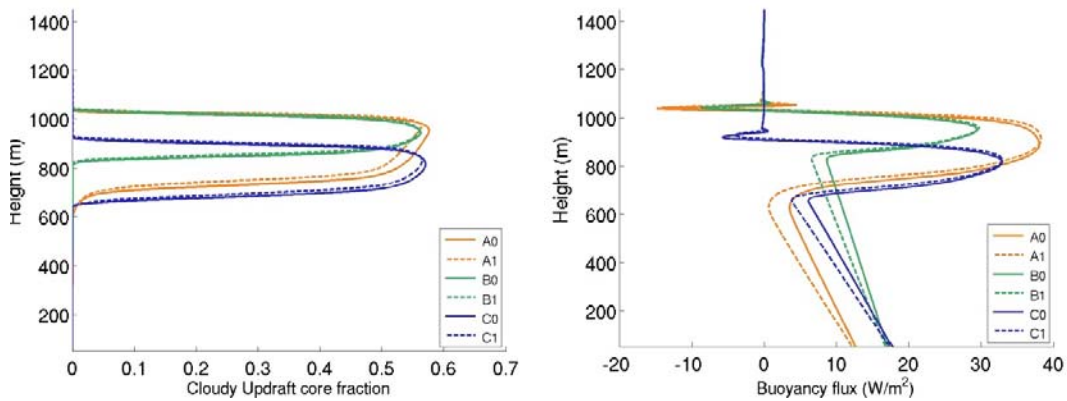


Figure 4.9 the 4-9 hour mean profiles of a) updraft fraction in the cloudy area; b) Buoyancy flux (W m⁻²) in group A, B, C.

Instead, the results show that the cloud droplet sedimentation modulates the cloud updrafts and downdrafts through stabilizing the upper part and destabilizing the lower BL. In the lower part of the cloud layer, the cloud droplet sedimentation supplies liquid water within the cloudy updrafts and increases evaporation cooling in the downdrafts. The net contribution of the cloud droplet sedimentation increases the updraft fraction (Fig. 4.9a), and cloud liquid water at the lower BL (Fig. 4.6b), and also lowering the static stability at the lower part of the cloud (Fig. 4.9b). In the upper part of the cloud layer, the liquid cloud water is

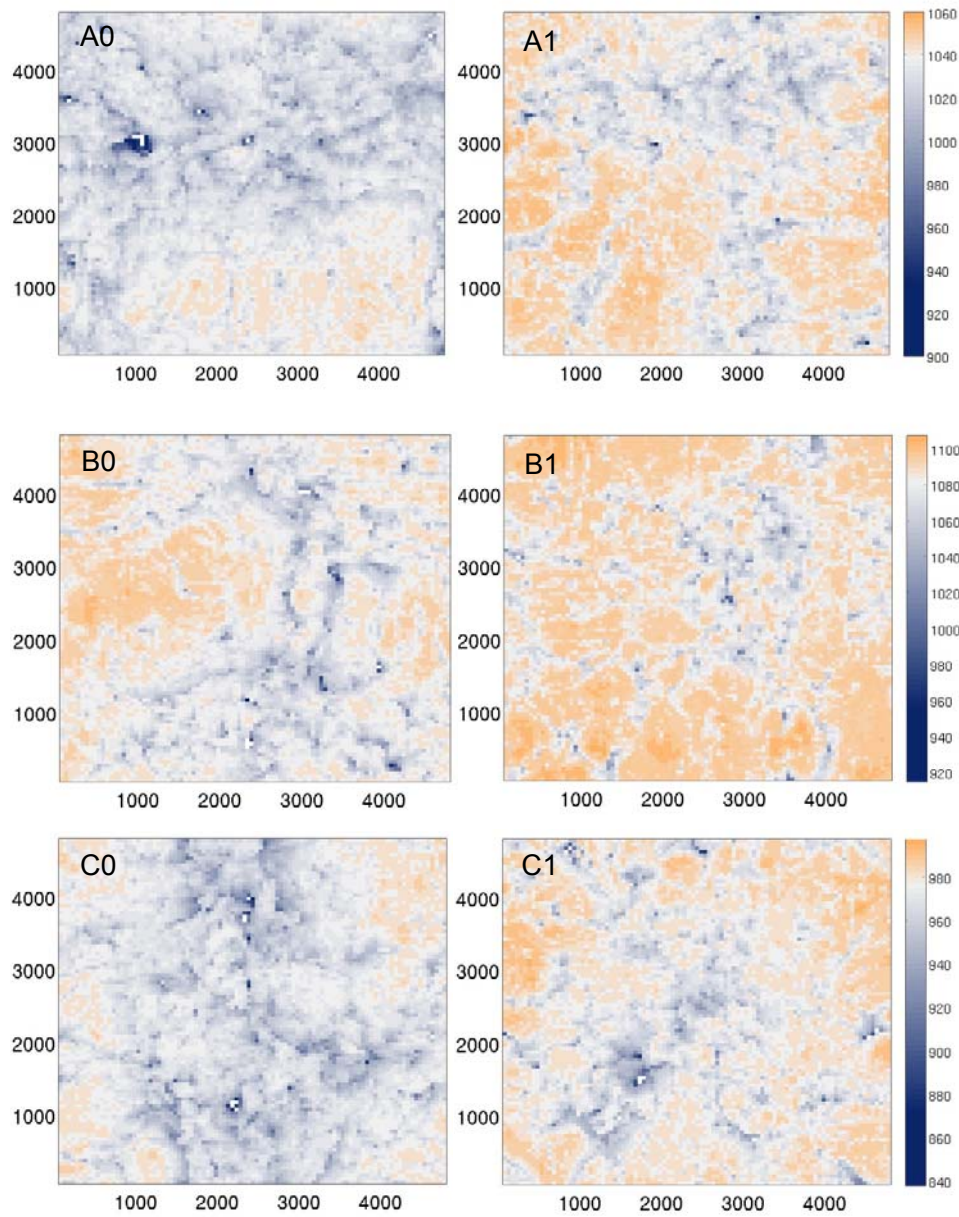


Figure 4.10 Horizontal distribution of cloud-top height in group A, B, C at $t = 15$ hour.

moved downward, especially in the updrafts where the liquid water is abundant and droplets are large. The large water loading in the updrafts inhibit the cloudy updrafts from reaching higher level. When the cloud droplet sedimentation is

reduced, the cloudy updrafts grow higher without the negative buoyancy of the water loading, which causes a more undulated cloud top (Fig. 4.10) and a slightly increased entrainment rate (Table 4.6). Meanwhile, the lower BL becomes less buoyant, and hence the condensation and cloud liquid water growth within the lower part of the cloud layer decreases. Therefore, the cloud LWPs slightly decrease in some of the polluted cases (Fig. 4.8) with weakened vertical velocity variances (Fig. 4.7). Because the cloud water sedimentation is small compared to the updrafts and downdrafts in the BL (a few cm s^{-1} vs. 1 m s^{-1}), its impact on the cloud LWP is not significant and the reduce of LWP due to decoupled CCN number concentration is less than 10%.

4.5 Summary and discussion

In this chapter, we utilize simplified and idealized LESs with prescribed large scale forcing based on the observed variations during VOCALS-Rex Twin Otter project to explore the impacts of the important metrological controlling factors such as vertical wind shear, surface fluxes, large-scale subsidence, solar radiation, and the BL-top stability, and also of the aerosol factors such as CCN number concentrations on the simulated cloud and BL variations.

The simulations capture the general features of the observed BL and cloud layer except for relatively stronger turbulence structure that is possibly due to the lack of large scale advection and larger surface fluxes than observations. Based on the results from sensitivity tests for the large-scale forcing, among these important large scale factors, large-scale subsidence controls most variation of the simulated LWPs. This implies that the variability of Sc cloud at the

time scale of days and the horizontal spatial scale of several to tens of kilometers are mainly dominated by the variation of local circulations, which also control the surface wind speed and, in turn, the surface fluxes. Large-scale vertical wind shear clearly induces cloud-top mixing and enhances entrainment rate. Within the range of observed large-scale forcing variations, the vertical wind shear could increase the whole BL turbulence intensity and decrease the simulated LWP by 25% (Case 4 vs Case 5). The solar radiation could weaken the BL turbulences, reduce the entrainment rate and decouple the BL. The contribution of the surface flux variations is not as significant as the other factors unless the surface fluxes increase to be twice as large as the observed values (Case 6, 8 and 9). The BL-top stability could inhibit the cloud-top entrainment processes, decrease the inversion height, increase the simulated LWP by 5-10%, and also weaken the BL turbulences.

The results from section 4.4 suggest that the effect of evaporation feedback on the entrainment rate is not as important as the prior study proposed. As we have shown before, the observed high CCN cases show no sign of drying effect and the entrainment rate is lower than that in the low CCN cases. Instead, the contributions of the different buoyancy feedbacks at the upper and the lower BL need to be considered. Based on the results from three different cloud scenarios, the LWP differences between the polluted and clean cases are lower than 10%. Therefore, it might not be necessary to add the sedimentation-entrainment feedback into the entrainment parameterization as some previous studies proposed.

At the end, we should emphasize again that all these results are based on idealized LESs. We used a two-momentum bulk microphysics scheme in which the cloud droplets activation processes are highly approximated and the impacts of clouds on the aerosol distributions are ignored. Therefore, additional tests with an explicit spectral-bin microphysics scheme are demanded in the future. Because it is computationally expensive to increase grid points, integration time, and prognostic variables, the current available vertical resolution (5m) near the cloud-top might overestimated the cloud-top mixing processes (Stevens et al. 2005), whose scales vary from tens of meters to several centimeters. The domain size in this study is 4.8 kmx4.8 km, therefore mesoscale fluctuations of thermodynamic variables (e.g., q_t) are not resolved in these simulations (de Roode and Duynkerke 2004), which might contribute to the vertical transports as well (Faloona et al. 2005). Furthermore, the periodic lateral boundary condition and horizontally homogenous constant large-scale forcing exclude the impacts of the mesoscale variations of the large-scale forcing (Moeng et al. 2007). All of the aforementioned issues are expected be addressed by increasing computational capability (i.e. increasing grid points and resolutions) and adopting more realistic numerical techniques such as multiple-scale numerical simulations (e.g., Zhu et al. 2010).

Chapter 5: Summary, conclusions and future work

5.1 Summary and conclusions

This dissertation seeks to investigate the impacts of meteorological factors and aerosol indirect effects on marine stratocumulus variations. In pursuit of this goal, both observational and numerical studies are conducted with the focus on observations from research aircraft project in the coastal region in the SE Pacific during VOCALS-REx, 2008.

Chapter 2 overviews the Twin Otter flight project and analyzes these *in-situ* observations and meteorological reanalysis, radiosonde and satellite-derived data to investigate the BL, clouds, and aerosol variations at 72° W, 20° S (Point Alpha) from Oct.16 to Nov. 13, 2008. It is shown that the BL at Point Alpha was the typical well-mixed BL topped by a thin and non-drizzling Sc layer on days without the dominant influence of the synoptic system and the coastal processes. The surface wind, the surface fluxes and the BL turbulence at Point Alpha appeared to be weaker than those over the other ocean regions. The weaker turbulence in the BL at Point Alpha might contribute to the lower entrainment rate calculated from the near cloud top fluxes. An additional finding obtained by comparing the *in-situ* data with the satellite retrievals is that the GOES-derived LWP was essentially the same as that determined from the vertical profiles of LWC observed in-situ, while the GOES-derived cloud droplet R_e tended to be larger than that observed near cloud top.

Because of the relatively constant meteorological conditions over this area during days with the typical well-mixed BL, this region can be an ideal

environment to study the aerosol-cloud interaction. During days with the typical well-mixed BL, the cloud LWP varied from 20 to 80 g m⁻², and the CCN ranged from 200 to 550 cm⁻³. In general, the cloud LWP increased with the sub-cloud CCN concentrations. On the other hand, the BL evolved gradually in response to factors influenced by synoptic systems. During an intense mid-latitude disturbance that affected the coastal area, the cloud LWP was clearly higher than the other days, indicating that meteorological factors and the decoupling processes have large influences on the cloud LWP variation as well. These results in chapter 2 provide a unique dataset for documenting the characteristics of the near-coastal marine Sc and the BL off the coast of Northern Chile, which can be valuable for the evaluation of models operating at a variety of scales to study near-coastal marine stratocumulus during VOCALS-REx.

With the goal of investigating the second aerosol indirect effect in marine stratocumulus clouds under relatively constant meteorological conditions, Chapter 3 further analyzes the clouds occurring on 10 of 18 flight days in well-mixed BL and relatively similar meteorological conditions. The results indicate a strong positive correlation between boundary layer CCN concentrations and cloud LWP associated with similar boundary layer conditions, which is inconsistent with some of the conclusions from previous modeling studies. The differences in the thermodynamic jumps at the top of the boundary layer and the turbulent fluxes at the surface cannot explain the observed differences in the LWP between the high CCN cases and the low CCN cases. The different contributions of large-scale advection to the time evolution of cloud layers are

found to be inadequate to cause the observed difference in the cloud depths between the high and the low CCN cases. The satellite retrievals show that the observed LWP differences were also prevalent during the night-time hours prior to the aircraft observations. As for the large-scale cloud structure, the satellite retrievals also reveal that the clouds with high CCN concentrations were solid over large area and have minimal LWP loss due to precipitation suppression effects. On the other hand, the clouds with low CCN concentrations revealed small cellular like structures and cloud rifts, which could be a sign of a drizzling event occurring during the night time when the clouds were thicker. Therefore, these results, which cannot be fully explained by current hypotheses from numerical modeling, motivate further studies to better explain the factors that control LWP and the role that the second indirect effects may play in the evolution of clouds.

As noted in chapter 3, in the observational study, it is impossible to completely rule out the possibility that the changes in CCN may be associated with small changes in the large-scale meteorological forcing that also largely affect the LWP. Therefore, Chapter 4 provides results from two sets of simplified and idealized LES simulations to explore the individual contributions of the important metrological factors along with the aerosol factors -- such as CCN number concentrations -- to the observed cloud and BL variations at Point Alpha. The simulations capture the general features of the observed BL and cloud layer except for relatively stronger turbulence structure, possibly due to the larger surface fluxes than observed and the lack of large scale advection and solar

radiation. The results from sensitivity tests for the large-scale forcing indicate that among these important large scale factors, large-scale subsidence controls most variation of the simulated LWPs. Large-scale vertical wind shear clearly induces cloud-top mixing and enhances entrainment rate. The solar radiation could weaken the BL turbulences, reduce the entrainment rate and decouple the BL. The contribution of the surface flux variations is not as significant as other factors unless the surface fluxes are increased to be twice as large as the observed values. Based on the simulation results, the variability of Sc cloud at the time scale of hours to one day and the horizontal spatial scale of several to tens of kilometers appears to be dominated by the variation of local circulations, which also controls the surface wind speed and the surface fluxes. The results from the sensitivity tests for the aerosol indirect effects suggest that without drizzling processes, simulated clouds decrease by less than 10% as the CCN number concentrations increase by about six times. Therefore, the effect of evaporation feedback on the entrainment rate is not as important as prior numerical studies proposed.

5.2 Future work

As discussed in previous chapters, the results in this study identify several possible directions for further work. The current observational study is focused on eighteen flight cases of near-coastal marine Sc in the SE Pacific which has been largely unexplored. In order to better understand the aerosol and cloud processes and the relationship between the cloud LWP and aerosol concentrations, it would be worthwhile to collect more *in-situ* observations of

aerosol and cloud properties over this area in the future to extend the dataset of the BL, clouds, and aerosol variations. More *in-situ* observations are also critical to the calibration of the satellite retrievals and the validation of numerical model simulations over this region, which is especially important because the near-coastal marine Sc off the coast of Northern Chile is still a major challenge of the modeling community. Furthermore, longer observations following the main flows will be useful to test the speculations proposed in Chapter 3 about the drizzle suppression effect of aerosols that occurred during the earlier history of the observed clouds.

The numerical study in this dissertation can be extended to simulations of both the larger scale processes and the smaller scale processes in future investigations. Currently, this study uses simplified and idealized LES. Consequently, further study with more realistic conditions will be useful to capture more the observed characteristics discussed in chapter 2. For instance, the large-scale horizontal advections can be included in the LES simulations. A regional model with nest-domain configuration that is able to capture the effects of the large-scale systems on the BL cloud layers will be one alternative to include the impact of realistic meteorological conditions. As for the smaller scale processes, it would be worthwhile to adopt an explicit spectral bin microphysical scheme into the idealized LES simulations, in which each type of aerosol and cloud hydrometeors is explicitly calculated and thus the shapes of the aerosol and cloud drop size distributions are prognosed rather than being prescribed as in the bulk microphysical scheme. Therefore, these simulations are expected to

be able to more realistically resolve cloud microphysical processes than the bulk microphysical scheme used in the current study.

References

- Ackerman, A. S., and Coauthors, 2009: Large-eddy simulations of a drizzling, stratocumulus-topped marine boundary layer. *Mon. Wea. Rev.*, **137**, 1083–1110.
- Ackerman, A. S., M. P. Kirkpatrick, D. E. Stevens, and O. B. Toon, 2004: The impact of humidity above stratiform clouds on indirect aerosol climate forcing. *Nature*, **432**, 1014–1017.
- Albrecht, B. A., 1989: Aerosol, cloud microphysics, and fractional cloudiness. *Science*, **245**, 1227–1230.
- Albrecht, B. A., D. A. Randall, and S. Nicholls, 1988: Observations of marine stratocumulus clouds during FIRE. *Bull. Amer. Meteor. Soc.*, **69**, 618–626.
- Albrecht, B. A., M. P. Jensen, and W.J. Syrett, 1995a: Marine boundary layer structure and fractional cloudiness. *J. Geophys. Res.*, **100**, D7209.
- Albrecht, B. A., C. S. Bretherton, D. Johnson, W. H. Scubert, and A. S. Frisch, 1995b: The Atlantic Stratocumulus Transition Experiment—ASTEX. *Bull. Amer. Meteor. Soc.*, **76**, 889–904.
- Berger, A. L., 1978: Long-term variations of daily insolation and quaternary climatic changes, *J. Atmos. Sci.*, **35**, 2362–2367.
- Betts, A. K., and W. Ridgway, 1989: Climatic equilibrium of the atmospheric convective boundary layer over a tropical ocean. *J. Atmos. Sci.*, **46**, 2621–2641.
- Bony, S., and J. -L. Dufresne, 2005: Marine boundary layer clouds at the heart of cloud feedback uncertainties in climate models. *Geophys. Res. Lett.*, **32**, L20806, doi:10.1029/2005GL023851.
- Bretherton, C. S., T. Uttal, C. W. Fairall, S. E. Yuter, R. A. Weller, D. Baumgardner, K. Comstock, R. Wood, and G. B. Raga, 2004: The EPIC 2001 stratocumulus study. *Bull. Amer. Meteor. Soc.*, **85**, 967–977.
- Bretherton, C. S., and M. C. Wyant, 1997: Moisture transport, lower-tropospheric stability, and decoupling of cloud-topped boundary layers. *J. Atmos. Sci.*, **54**, 148–167.
- Bretherton, C. S., R. Wood, R. C. George, D. Leon, G. Allen, and X. Zheng, 2010: Southeast Pacific stratocumulus clouds, precipitation and boundary layer structure sampled along 20 S during VOCALS-REx, *Atmos. Chem. Phys. Discuss.*, **10**, 15921–15962, doi:10.5194/acpd-10-15921-2010.

- Bretherton, C. S., P. N. Blossery, and J. Uchida, 2007: Cloud droplet sedimentation, entrainment efficiency, and subtropical stratocumulus albedo. *Geophys. Res. Lett.*, **34**, L03813, doi: 10.1029/2006GL027648.
- Brioude, J., and Coauthors, 2009: Effect of biomass burning on marine stratocumulus clouds off the California coast. *Atmos. Chem. Phys.*, **9**, 8841-8856.
- Caldwell, P., R. Wood, and C. S. Bretherton, 2005: Mixed layer budget analysis of the diurnal cycle of entrainment in SE Pacific stratocumulus. *J. Atmos. Sci.*, **62**, 3775–3791.
- Caldwell, P., and C. S. Bretherton, 2009: Large eddy simulation of the diurnal cycle in Southeast Pacific stratocumulus. *J. Atmos. Sci.*, **66**, 432-449.
- Cheng, A., and K.-M. Xu, 2009: A PDF-based microphysics parameterization for simulation of drizzling boundary layer clouds. *J. Atmos. Sci.*, **66**, 2317-2334.
- Christensen, M. W., J. A. Coakley, and W. R. Tahnk, 2009: Morning-to-afternoon evolution of marine stratus polluted by underlying ships: Implications for the relative lifetimes of polluted and unpolluted clouds, *J. Atmos. Sci.*, **66**, 2097-2106.
- Coakley, J. A., and C. D. Walsh, 2002: Limits to the aerosol indirect radiative effect derived from observations of ship tracks. *J. Atmos. Sci.*, **59**, 668–680.
- Coakley, J. A., R. D. Cess, and F. B. Yurevich, 1983: The effect of tropospheric aerosols on the Earth's radiation budget: A parameterization for climate models, *J. Atmos. Sci.*, **40**, 116-138.
- Collins, W. D., J. K. Hackney, and D. P. Edwards, 2002: A new parameterization for infrared emission and absorption by water vapor in the National Center for Atmospheric Research Community Atmosphere Model, *J. Geophys. Res.*, **107** (D22), 4664, doi:10.1029/2001JD001365.
- Collins, W. D., and Coauthors, 2006: The formulation and atmospheric simulation of the Community Atmosphere Model version 3 (CAM3). *J. Climate*, **19**, 2144–2161.
- Cronin, M. F., N. Bond, C. Fairall, J. Hare, M. J. McPhaden, and R. A. Weller, 2002: Enhanced oceanic and atmospheric monitoring underway in eastern Pacific. *Eos, Trans. Amer. Geophys. Union*, **83** (19), 205, 210–211.

- de Szoeke, S. P., and C. S. Bretherton, 2004: Quasi-Lagrangian large eddy simulations of cross-equatorial flow in the east Pacific atmospheric boundary layer. *J. Atmos. Sci.*, **61**, 1837–1858.
- de Roode, S. R., P. G. Duynkerke, and H. J. Jonker, 2004: Large eddy simulation: how large is large enough? *J. Atmos. Sci.*, **61**, 403–421.
- Deardorff, J. W., 1980: Stratocumulus-capped mixed layer derived from a three-dimensional model. *Boundary-Layer Meteorol.*, **18**, 495–527.
- Dong, X., P. Minnis, G. G. Mace, W. L. Smith, Jr., M. Poellot, R. T. Marchand, and A. D. Rapp, 2002: Comparison of stratus cloud properties deduced from surface, GOES, and aircraft data during the March 2000 ARM Cloud IOP. *J. Atmos. Sci.*, **59**, 3256–3284.
- Draxler, R.R. and G. D. Rolph, 2011: HYSPLIT (HYbrid Single-Particle Lagrangian Integrated Trajectory) Model access via NOAA ARL READY Website (<http://ready.arl.noaa.gov/HYSPLIT.php>). NOAA Air Resources Laboratory, Silver Spring, MD
- Duynkerke, P. G., 1993: The stability of cloud top with regard to entrainment: Amendment of the theory of cloud-top entrainment instability. *J. Atmos. Sci.*, **50**, 495–502.
- Feingold, G., L. A. Remer, J. Ramaprasad, and Y. Kaufman, 2001: Analysis of smoke impact on clouds in Brazilian biomass burning regions: An extension of Twomey's approach, *J. Geophys. Res.*, **106**, 22,907–22,922, doi:10.1029/2001JD000732.
- Feingold, G., I. Koren, H. Wang, H. Xue, and W. A. Brewer, 2010: Precipitation-generated oscillations in open cellular cloud fields. *Nature*, **466**, doi:10.1038 /nature09314.
- Faloona, I., and Coauthors, 2005: Observations of entrainment in eastern pacific marine stratocumulus using three conserved scalars. *J. Atmos. Sci.*, **62**, 3268–3285.
- Garreaud, R. D. and R. Muñoz, 2004: The diurnal cycle in circulation and cloudiness over the subtropical southeast Pacific: A modeling study. *J. Climate*, **17**, 1699–1710.
- Garreaud, R. D. and R. C. Muñoz, 2005: The low-level jet off the west coast of subtropical South America: Structure and variability, *Mon. Wea. Rev.*, **133**, 2246–2261.

- Garreaud, R. D., J. Rutllant, J. Quintana, J. Carrasco, and P. Minnis, 2001: CIMAR-5: A snapshot of the lower troposphere over the subtropical southeast Pacific, *Bull. Amer. Meteor. Soc.*, **92**, 2193-2208.
- Geoffroy, O., J. L. Brenguier, and I. Sandu, 2008: Relationship between drizzle rate, liquid water path and droplet concentration at the scale of a stratocumulus cloud system. *Atmos. Chem. Phys.*, **8**, 4641–4654.
- George, R. C., and R. Wood, 2010: Subseasonal variability of low cloud radiative properties over the 20 southeast Pacific Ocean. *Atmos. Chem. Phys.*, **10**, 4047–4063, doi:10.5194/acp-10-4047- 2010.
- Gerber, H., B. G. Arends, and A. S. Ackerman, 1994: A new microphysics sensor for aircraft use. *Atmos. Res.*, **31**, 235–252.
- Gerber, H., G. Frick, S. P. Malinowski, J.-L., Brenguier and F. Burnet, 2005: Holes and entrainment in stratocumulus, *J. Atmos. Sci.*, **62**, 443-459.
- Ghate, V. P., B. A. Albrecht, C. W. Fairall, and R. A. Weller, 2009: Climatology of surface meteorology, surface fluxes, cloud fraction and radiative forcing over south-east Pacific from buoy observations. *J. Climate*, **22**, 5227-5540.
- Hahn, C. J., and S. G. Warren, 2007: A gridded climatology of clouds over land (1971-96) and ocean (1954-97) from surface observations worldwide. Numeric Data Package NDP-026E ORNL/CDIAC-153, CDIAC, Department of Energy, Oak Ridge, Tennessee.
- Haman, K. E., S. P. Malinowski, M. J. Kurowski, H. Gerber, and J.-L. Brenguier, 2007: Small scale mixing processes at the top of a marine stratocumulus - a case study. *Quart. J. Roy. Meteorol. Soc.*, **133**, 213–226.
- Hartmann, D. L., M. E. Ockert-Bell, and M. L. Michelsen, 1992: The effect of cloud type on earth's energy balance - Global analysis. *J. Climate*, **5**, 1281–1304.
- Hignett, P., 1991: Observations of diurnal variation in a cloud-capped marine boundary layer. *J. Atmos. Sci.*, **48**, 1474–1482.
- Hill, A. A., and G. Feingold, 2009: The influence of entrainment and mixing assumption on aerosol–cloud interactions in marine stratocumulus. *J. Atmos. Sci.*, **66**, 1450-1464.
- Jiang, Q., Wang, S., and L. O'Neill, 2010: Some insights into the characteristics and dynamics of the Chilean low-level coastal jet. *Mon. Wea. Rev.*, **138**, 3185–3206.

- Joseph, J. H., W. J. Wiscombe, and J. A. Weinman, 1976: The delta-Eddington approximation for radiative flux transfer, *J. Atmos. Sci.*, **33**, 2452-2459.
- Katzwinkel, J., H. Siebert, and R. A. Shaw, 2011: Observation of a self-limiting, shear-induced turbulent inversion layer above marine stratocumulus, *Bound.-Lay. Meteorol.*, doi:10.1007/s10546-011-9683-4, in press.
- Khairoutdinov, M. F., and Y. L. Kogan, 1999: A large-eddy simulation model with explicit microphysics: Validation against aircraft observations of a stratocumulus-topped boundary layer. *J. Atmos. Sci.*, **56**, 2115-2131.
- Khairoutdinov, M.F., and D. A. Randall, 2003: Cloud resolving modeling for the ARM summer 1997 IOP: Model formulation, results, uncertainties, and sensitivities. *J. Atmos. Sci.*, **60**, 607-625.
- Kistler, R., and Coauthors, 2001: The NCEP–NCAR 50-Year Reanalysis: Monthly means CD-ROM and documentation. *Bull. Amer. Meteor. Soc.*, **82**, 247-267.
- Klein, S. A., and D. L. Hartmann, 1993: The seasonal cycle of low stratiform clouds. *J. Climate*, **6**, 1587–1606.
- Klein, S. A., 1997: Synoptic variability of low-cloud properties and meteorological parameters in the subtropical trade wind boundary layer. *J. Climate*, **10**, 2018–2039.
- Kollias, P., C. W. Fairall, P. Zuidema, J. Tomlinson, and G. A. Wick, 2004: Observations of marine stratocumulus in SE Pacific during the PACS 2003 cruise. *Geophys. Res. Lett.*, **31**, L22110, doi: 10.1029/2004GL020751 .
- Koren, I., L. A. Remer, Y. J. Kaufman, Y. Rudch, and J. V. Martins, 2007: On the twilight zone between clouds and aerosols. *Geophys. Res. Lett.*, **34**, L08805, doi:10.1029/2007GL029253.
- Kuo, H.-C., and W. H. Schubert, 1988: Stability of cloud-topped boundary layers. *Quart. J. Roy. Meteor. Soc.*, **114**, 887–916.
- Lilly, D. K., 1968: Models of cloud-topped mixed layers under a strong inversion. *Quart. J. Roy. Meteorol. Soc.*, **94**, 292–309.
- Lilly, D. K., 2002: Entrainment into mixed layers. Part II: A new closure. *J. Atmos. Sci.*, **59**, 3353–3361.
- Lohmann, U. and J. Feichter, 2005: Global indirect aerosol effects: A review. *Atmos. Chem. Phys.*, **5**, 715–737.

- Lu, M.-L., and J. H. Seinfeld, 2005: Study of the aerosol indirect effect by large-eddy simulation of marine stratocumulus. *J. Atmos. Sci.*, **62**, 3909-3932.
- Lu, M. L., W. C. Conant, H. H. Jonsson, V. Varutbangkul, R. C. Flagan, and J. H. Seinfeld, 2007: The Marine Stratus /Stratocumulus Experiment (MASE): Aerosol-cloud relationships in marine stratocumulus. *J. Geophys. Res.*, **112**, D10 209.
- Mauger, G. S., J. R. Norris, 2010: Assessing the impact of meteorological history on subtropical cloud fraction. *J. Climate*, **23**, 2926–2940.
- Mellado, J. P., 2010: The evaporatively driven cloud-top mixing layer, *J. Fluid Mech.*, **660**, 5–36.
- Minnis, P., and Coauthors, 2011a: CERES Edition-2 cloud property retrievals using TRMM VIRS and Terra and Aqua MODIS data, Part I: Algorithms. *IEEE Trans. Geosci. Remote Sens.*, doi: 10.1109/TGRS.2011.2144601, in press
- Minnis, P., and Coauthors, 2011b: CERES Edition-2 cloud property retrievals using TRMM VIRS and Terra and Aqua MODIS data, Part II: Examples of average results and comparisons with other data. *IEEE Trans. Geosci. Remote Sens.*, doi: 10.1109/TGRS.2011.2144602.
- Moeng, C. H., and coauthors, 1996: Simulation of a stratocumulus-topped planetary boundary layer: Intercomparison among different numerical codes. *Bull. Am. Meteor. Soc.*, **77**, 261-278.
- Moeng, C. H., J. Dudhia, J. Klemp, and P. Sullivan, 2007: Examining two-way grid nesting for large eddy simulation of the PBL using the WRF Model, *Mon. Weather Rev.*, **135**, 2295–2311.
- Morrison, H., J. A. Curry, and V. I. Khvorostyanov, 2005: A new doublemoment microphysics parameterization for application in cloud and climate models. Part I: Description. *J. Atmos. Sci.*, **62**, 1665–1677.
- Nieuwstadt, F. T. M., and J. A. Businger, 1984: Radiative cooling near the top of a cloudy mixed layer. *Quart. J. Roy. Meteorol. Soc.*, **110**, 1073–1078.
- Norris, J. R., 1998: Low cloud type over the ocean from surface observations. Part I: Relationship to surface meteorology and the vertical distribution of temperature and moisture. *J. Climate*, **11**, 369-382.
- Norris, J. R., and S. A. Klein, 2000: Low cloud type over the ocean from surface observations. part III: Relationship to vertical motion and the regional synoptic environment. *J. Climate*, **13**, 245–256.

- Nucciarone, J. J., and G. S. Young, 1991: Aircraft measurements of turbulence spectra in the marine stratocumulus-topped boundary layer. *J. Atmos. Sci.*, **48**, 2382-2392.
- O'Dell, C.W., F.J. Wentz, and R. Bennartz, 2008: Cloud liquid water path from satellite-based passive microwave observations: A new climatology over the global oceans. *J. Climate*, **21**, 1721–1739.
- Ogura, Y. and N. A. Phillips, 1962: Scale analysis of deep and shallow convection in the atmosphere. *J. Atmos. Sci.*, **19**, 173-179.
- Painemal, D., and P. Zuidema, 2010: Microphysical variability in Southeast Pacific stratocumulus clouds: Synoptic conditions and radiative response. *Atmos. Chem. Phys.*, **10**, 6255-6269.
- Pruppacher, H. R., and J. D. Klett, 1997: Microphysics of clouds and precipitation, 954 pp., Kluwer Acad., Dordrecht, Netherlands.
- Rahn, D. A., and R. D. Garreaud, 2010a: Marine boundary layer over the subtropical southeast Pacific during VOCALS-REx. Part 1: Mean structure and diurnal cycle, *Atmos. Chem. Phys.*, **10**, 4491- 4506, doi:10.5194/acp-10-4491-2010.
- and -----, 2010b: Marine boundary layer over the subtropical southeast Pacific during VOCALS-REx. Part 2: Synoptic variability, *Atmos. Chem. Phys.*, **10**, 4507- 4519, doi:10.5194/acp-10-4507-2010.
- Ramanathan, V., and P. Downey, 1986: A nonisothermal emissivity and absorptivity formulation for water vapor, *J. Geophys. Res.*, **91**, 8649-8666.
- Randall, D. A., 1980: Conditional instability of the first kind upside-down. *J. Atmos. Sci.*, **37**, 125–130.
- Rozendall, M. A., and W. B. Rossow, 2003: Characterizing some of the influences of the general circulation on subtropical marine boundary layer clouds. *J. Atmos. Sci.*, **60**, 711-728.
- Sandu, I., J.-L. Brenguier, O. Geoffroy, O. Thouron, V. Masson, 2008: Aerosol impacts on the diurnal cycle of marine stratocumulus. *J. Atmos. Sci.*, **65**, 2705–2718.
- Sandu, I., J.-L. Brenguier, O. Thouron, and B. Stevens, 2009: How important is the vertical structure for the representation of aerosol impacts on the diurnal cycle of marine stratocumulus? *Atmos. Chem. Phys.*, **9**, 4039–4052.

- Savic-Jovicic, V., and B. Stevens, 2008: The structure and mesoscale organization of precipitating stratocumulus. *J. Atmos. Sci.*, **65**, 1587-1605.
- Schubert, W. H., J. S. Wakefield, E. J. Steiner, and S. K. Cox, 1979a: Marine stratocumulus convection. Part I: Governing equations and horizontally homogeneous solutions. *J. Atmos. Sci.*, **36**, 1286-1306.
- Schubert, W. H., J. S. Wakefield, E. J. Steiner and S. K. Cox, 1979b: Marine stratocumulus convection. Part II: Horizontally inhomogeneous solutions. *J. Atmos. Sci.*, **36**, 1308- 1324.
- Seifert, A. and K.D. Beheng, 2001: A double-moment parameterization for simulating autoconversion, accretion and selfcollection, *Atmos. Res.*, **59**, 265– 281.
- Serpetzoglou, E., B. A. Albrecht, P. Kollias, and C. W. Fairall, 2008: Boundary layer, cloud, and drizzle variability in the southeast Pacific stratocumulus regime. *J. Climate*, **21**, 6191–6214.
- Sharon, T. M., B. A. Albrecht, H. H. Jonsson, P. Minnis, M. M. Khaiyer, T. M. van Reken, J. Seinfeld, and R. Flagan, 2006: Aerosol and cloud microphysical characteristics of rifts and gradients in marine stratocumulus clouds. *J. Atmos. Sci.*, **63**, 983–997.
- Siebesma, A. P., and Coauthors, 2003: A large eddy simulation intercomparison study of shallow cumulus convection. *J. Atmos. Sci.*, **60**, 1201-1219.
- Siems, S. T., M. B. Baker, S. S. Shy, and R. E. Breidenthal, 1990: Buoyancy reversal and cloud-top entrainment instability. *Quart. J. Roy. Meteor. Soc.*, **116**, 705–739.
- Slingo, A., 1989: A GCM parameterization for the shortwave radiative properties of clouds. *J. Atmos. Sci.*, **46**, 1419-1427.
- Slingo, A., 1990: Sensitivity of the Earth's radiation budget to changes in low clouds. *Nature*, **343**, 49–51.
- Smolarkiewicz, P. K., and W. W. Grabowski, 1990: The multidimensional positive definite advection transport algorithm: Nonoscillatory option. *J. Comput. Phys.*, **86**, 355-375.
- Soden, B. J., and G. A. Vecchi, 2011: The vertical distribution of cloud feedback in coupled ocean-atmosphere models, *Geophys. Res. Lett.*, **38**, L12704, doi:10.1029/2011GL047632.

- Stevens, B., and Coauthors, 2003: Dynamics and chemistry of marine stratocumulus-DYCOMS-II, *Bull. Amer. Meteorol. Soc.*, **84**, 579–593.
- Stevens, B., and coauthors, 2005: Evaluation of large-eddy simulations via observations of nocturnal marine stratocumulus, *Mon. Weather Rev.*, **133**, 1443–1462.
- Stevens, B., A. Beljaars, S. Bordoni, C. Holloway, M. Kohler, S. Krueger, V. Savic-Jovicic, and Y. Y. Zhang, 2007: On the structure of the lower troposphere in the summertime stratocumulus regime of the northeast Pacific. *Mon. Wea. Rev.*, **135**, 985–1005.
- Stevens, B., and G. Feingold, 2009: Untangling aerosol effects on clouds and precipitation in a buffered system. *Nature*, **461**, doi: 10.1038/nature08281.
- Stevens, B. and J.-L. Brenguier, 2008: Cloud controlling factors -- low clouds, Ernst Strüngmann Forum Contribution to Perturbed Clouds in the Climate System, Heintzenberg and Charslon Eds., MIT Press.
- Twomey, S., 1977: Influence of pollution on shortwave albedo of clouds, *J. Atmos. Sci.*, **34**, 1149–1152.
- Tonizza, T., S. J. Abel, R. Wood, C. R. Mechoso, G. Allen, and L. C. Shaffrey, 2011: Large-scale and synoptic meteorology in the south-east Pacific during the observations campaign VOCALS-REx in austral Spring 2008. *Atmos. Chem. Phys.*, **11**, 4977–5009, doi:10.5194/acp-11-4977-2011.
- Turton, J. D., and S. Nicholls, 1987: A study of the diurnal variation of stratocumulus using a multiple mixed layer model. *Q. J. R. Meteorol. Soc.*, **113**, 969–1009.
- Wang, S., L. W. O'Neill, Q. Jiang, S. P. de Szoeke, X. Hong, H. Jin, W. T. Thompson, and X. Zheng, 2011: A regional real-time forecast of marine boundary layers during VOCALS-REx, *Atmos. Chem. Phys.*, **11**, 421–437, doi:10.5194/acp-11-421-2011.
- Wang, S., Q. Wang, and G. Feingold, 2003: Turbulence, condensation, and liquid water transport in numerically simulated nonprecipitating stratocumulus clouds. *J. Atmos. Sci.*, **60**, 262–278.
- Wang, S., X. Zheng, and Q. Jiang, 2012: Strongly sheared stratocumulus convection: an observationally based large-eddy simulation study, *Atmos. Chem. Phys. Discuss.*, **12**, 4941–4977, doi: 10.5194 /acpd-12-4941-2012.

- Warren, S. G., C. J. Hahn, J. London, R. M. Chervin, and R. L. Jenne, 1988: Global distribution of total cloud cover and cloud types over ocean. NCAR Technical Note, National Center for Atmospheric Research, Boulder, CO.
- Weaver, C. J., and R. Pearson Jr., 1990: Entrainment instability and vertical motion as causes of stratocumulus break up. *Q. J. Roy. Met. Soc.*, **116**, 1359-1388.
- Wood, R., 2007: Cancellation of aerosol indirect effects in marine stratocumulus through cloud thinning. *J. Atmos. Sci.*, **64**, 2657-2669.
- Wood, R. and C.S. Bretherton, 2004: Boundary layer depth, entrainment, and decoupling in the cloud-capped subtropical and tropical marine boundary layer. *J. Climate*, **17**, 3576-3588.
- Wood, R., 2005: Drizzle in stratiform boundary layer clouds. Part I: Vertical and horizontal structure. *J. Atmos. Sci.*, **62**, 3011– 3033.
- Wood, R., and Coauthors, 2011a: The VAMOS Ocean-Cloud-Atmosphere-Land Study Regional Experiment (VOCALS-REx): goals, platforms, and field operations, *Atmos. Chem. Phys.*, **11**, 627-654, doi:10.5194/acp-11-627-2011.
- Wood, R., C. Bretherton, D. Leon, A. Clarke, P. Zuidema, G. Allen, and H. Coe, 2011b: An aircraft case study of the spatial transition from closed to open mesoscale cellular convection over the southeast Pacific. *Atmos. Chem. Phys.*, **11**, 2341–2370.
- Wood, R., 2012: Stratocumulus clouds. *Mon. Wea. Rev.*, doi:10.1175/MWR-D-11-00121.1, in press.
- Wood, R. and C. S. Bretherton, 2006: On the relationship between stratiform low cloud cover and lower tropospheric stability. *J. Climate*, **19**, 6425–6432.
- Wyant, M. C., and Coauthors, 2010: The PreVOCA experiment: modeling the lower troposphere in the Southeast Pacific, *Atmos. Chem. Phys.*, **10**, 4757–4774, doi:10.5194/acp-10-4757-2010.
- Xiao, H., C.-M. Wu, and C. R. Mechoso, 2010: Buoyancy reversal, decoupling and the transition from stratocumulus-topped to trade-wind cumulus-topped marine boundary layer. *Clim. Dyn.*, **37**, 971–984.
- Xie, S.-P., 2004b: Satellite observations of cool ocean–atmosphere interaction. *Bull. Amer. Meteor. Soc.*, **85**, 195–208.

- Xu, H., S. Xie, Y. Wang, 2005: Subseasonal variability of the southeast Pacific stratus cloud deck. *J. Climate*, **18**, 131–142. doi: 10.1175/JCLI3250.1.
- Yamaguchi, T., and D. A. Randall, 2008: Large-eddy simulation of evaporatively driven entrainment in cloud-topped mixed layers. *J. Atmos. Sci.*, **65**, 1481–1504.
- Yamaguchi, T., D. A. Randall, and M. F. Khairoutdinov, 2011: Cloud modeling tests of the ULTIMATE-MACHO scalar advection scheme. *Mon. Wea. Rev.*, **139**, 3248–3264.
- Zheng, X., B. A. Albrecht, P. Minnis, K. Ayers, H. H. and Jonsson, 2010: Observed aerosol and liquid water path relationships in marine stratocumulus, *Geophys. Res. Lett.*, **37**, L17803.
- Zheng, X. B. Albrecht, H. H. Jonsson, D. Khelif, G. Feingold, P. Minnis, K. Ayers, P. Chuang, S. Donaher, D. Rossiter, V. Ghate, J. Ruiz-Plancarte, and S. Sun-Mack, 2011: Observations of the boundary layer, cloud, and aerosol variability in the southeast Pacific near-coastal marine stratocumulus during VOCALS-REx. *Atmos. Chem. Phys.*, **11**, 9943–9959.
- Zhu, P. C. Bretherton, M. Kohler, A. Cheng, A. Chlond, Q. Geng, P. Austin, J.-C. Golaz, G. Lenderink, A. Lock, B. Stevens, 2005: Intercomparison and interpretation of single column model simulations of a nocturnal stratocumulus topped marine boundary layer. *Mon. Wea. Rev.*, **133**, 2741–2758.
- Zhu, P., B. A. Albrecht, V. P. Ghate, Z.-D., Zhu, 2010: Multiple scale simulations of stratocumulus clouds. *J. Geophys. Res.*, **115**, D23201, doi:10.1029/2010JD014400.
- Zuidema, P., D. Painemal, S. de Szoeke, and C. Fairall, 2009: Stratocumulus cloud-top height estimates and their climatic implications. *J. Climate*, **22**, 4652–4666, doi:10.1175/2009jcli2708.1.